AFIT/GE/ENG/93D-18

AD-A274 049

DTIC
ELECTE
DEC 23 1993
S E D

DESIGN OF A FLIGHT CONTROLLER FOR AN UNMANNED RESEARCH VEHICLE WITH CONTROL SURFACE FAILURES USING QUANTITATIVE FEEDBACK THEORY

THESIS

Mark S. Keating
Captain, USAF

AFIT/GE/ENG/93D-18

93-31001

Approved for public release; distribution unlimited

93 12 22 114

AFIT/GE/ENG/93D-18

DESIGN OF A FLIGHT CONTROLLER FOR AN UNMANNED RESEARCH VEHICLE WITH CONTROL SURFACE FAILURES USING QUANTITATIVE FEEDBACK THEORY

THESIS

Presented to the Faculty of the Graduate School of Engineering
of the Air Force Institute of Technology
Air University
In Partial Fulfillment of the
Requirements for the Degree of
Master of Science in Electrical Engineering

Mark S. Keating, B.S.E.E.
Captain, USAF

December, 1993

Accesion For
NTIS CRA&I
DTIC TAB
Unannounced
Justification
By
Distribution /
Availability Codes
Dist | Avail and / or Special
A-1

DTIC COPY INSPECTED 6

Approved for public release; distribution unlimited

Acknowledgements

My deep appreciation goes to the many members of the AFIT community whose interest and insight have made this research effort possible. Sincere thanks go to my advisor Dr Meir Pachter. It was a pleasure learning from his knowledge of the aircraft control problem not only during this thesis effort, but in the classroom as well. I also would like to thank Dr Constantine Houpis for his willingness to share his knowledge of QFT over the past 18 months. It was also a pleasure working with Capt Stuart Sheldon and Capt Steve Rasmussen of Wright Laboratories, who not only sponsored this thesis, but provided welcome advice and direction during its completion. Acknowledgments must also go to my classmates, who have not only enhanced my academic experience but also made it a lot of fun along the way.

Finally, my deepest thanks go to members of my family. To my parents, for laying the educational foundation which has allowed me to achieve my goals and to my wife, Margaret, for her understanding and patience. Set your goals then achieve them.

Mark S. Keating

Table of Contents

		Page
Acknowledgements		2
List of Figures		7
List of Tables		10
Abstract		11
I.	Introduction	1-1
	1.1 Background	1-1
	1.2 Problem	1-2
	1.3 Summary of Current Knowledge	1-3
	1.4 Assumptions	1-5
	1.5 Scope	1-6
	1.6 Standards	1-6
	1.7 Approach/Methodology	1-6
	1.8 Materials and Equipment	1-9
	1.9 Other Support	1-9
II.	The Lambda Aircraft	2-1
	2.1 The Aircraft	2-1
	2.2 The Model	2-3
	2.3 Actuators and Sensors	2-5
III.	Control Surface Failure Modeling	3-1
	3.1 Longitudinal Derivatives	3-1
	3.1.1 M Equation Analysis	3-2

Page

3.1.2 Z Equation Analysis 3-6

3.2 Lateral Derivatives 3-8

3.2.1 Y Equation Analysis 3-9

3.2.2 L Equation Analysis 3-10

3.2.3 N Equation Analysis 3-11

3.3 Disturbance Modeling 3-12

3.3.1 Lateral Disturbance 3-13

3.3.2 Longitudinal Disturbance 3-17

3.3.3 Plant and Disturbance Matrices 3-21

IV. Longitudinal MISO Design 4-1

4.1 Plant Generation 4-1

4.1.1 Flight Conditions 4-1

4.1.2 Short-Period Approximation 4-3

4.2 Design Technique 4-4

4.3 Loaded and Effective Plants 4-7

4.4 Plant Templates 4-9

4.5 Tracking and Disturbance Bounds 4-14

4.6 Compensator $G_{11}(s)$ 4-15

4.7 Prefilter $F_{11}(s)$ 4-19

4.8 Validation of the QFT Design 4-22

4.9 Simulation 4-23

4.10 Other Concerns 4-28

V. Lateral MIMO Design 5-1

5.1 Plant Generation 5-1

5.1.1 Flight Conditions 5-1

5.1.2 Plant Transfer Function Matrix 5-2

Page

5.2 Design Technique 5-3

5.3 Loaded, Effective and MISO Equivalent Plants 5-4

5.3.1 Loaded Plants 5-4

5.3.2 Effective Plants 5-6

5.3.3 MISO Equivalent Loops 5-9

5.4 Plant Templates 5-12

5.5 Loop-Shaping 5-14

5.6 Compensators $G_{ii}(s)$ 5-16

5.7 Prefilters $F_{ii}(s)$ 5-18

5.8 Validation of the QFT Design 5-21

5.9 Simulation 5-24

5.10 Other Concerns 5-26

VI. Autopilot Design 6-1

VII. Summary, Conclusions and Recommendations 7-1

7.1 Summary 7-1

7.2 Conclusions 7-3

7.3 Recommendations 7-4

Appendix A. Modified Model Generation Macro A-1

Appendix B. Flight Conditions B-1

B.1 Longitudinal Conditions B-1

B.2 Lateral Conditions B-2

Appendix C. Longitudinal Plant Transfer Functions C-1

C.1 Longitudinal $P_e(s)$ Short-Period Transfer Functions C-1

C.2 Longitudinal $P_d(s)$ Short-Period Transfer Functions C-3

Page

Appendix D. Lateral Plant Transfer Functions D-1

D.1 Transfer Function $\mathbf{P}_{e_{11}}(s) = \frac{p(s)}{\delta_a(s)}$ D-1

D.2 Transfer Function $\mathbf{P}_{e_{12}}(s) = \frac{p(s)}{\delta_r(s)}$ D-3

D.3 Transfer Function $\mathbf{P}_{e_{21}}(s) = \frac{\beta(s)}{\delta_r(s)}$ D-5

D.4 Transfer Function $\mathbf{P}_{e_{22}}(s) = \frac{\beta(s)}{\delta_r(s)}$ D-7

D.5 Transfer Function $\mathbf{P}_{d_{11}}(s) = \frac{p(s)}{d(s)}$ D-9

D.6 Transfer Function $\mathbf{P}_{d_{21}}(s) = \frac{\beta(s)}{d(s)}$ D-11

Appendix E. MISO Equivalent Transfer Functions E-1

E.1 Roll Channel $q_{22}(s)$ E-1

E.2 Yaw Channel $q_{33_e}(s)$ E-3

Appendix F. Difference Equations F-1

Bibliography BIB-1

Vita VITA-1

List of Figures

Figure		Page
2.1.	Lambda Schematic	2-2
3.1.	M_α vs. ζ_e	3-5
3.2.	MIMO QFT CAD Package Block Diagram	3-21
4.1.	Frequency Response of Complete Longitudinal Eqs. and Short-Period Approximations	4-3
4.2.	Longitudinal Plant and Actuator Dynamics	4-6
4.3.	Longitudinal PCT Implementation	4-7
4.4.	Frequency Response of Longitudinal $P_l(s)$ and $P_d(s)$	4-8
4.5.	Frequency Response of Longitudinal P_e (short-period)	4-9
4.6.	Longitudinal Closed-Loop Tracking Bounds	4-10
4.7.	Longitudinal Templates	4-11
4.8.	Longitudinal Template $w = 6$	4-12
4.9.	Modified Longitudinal Template $w = 6$	4-12
4.10.	Longitudinal Tracking Bounds	4-15
4.11.	Longitudinal Disturbance Bounds	4-16
4.12.	Longitudinal Nominal Loop Transmission	4-18
4.13.	$G_{11}(s)$ and $G_{11}(z)$ Controller Frequency Responses	4-19
4.14.	Longitudinal Closed Loop Response	4-21
4.15.	$F_{11}(s)$ and $F_{11}(z)$ Pre-Filter Frequency Responses	4-21
4.16.	Longitudinal Open-Loop Transmissions with $G_{11}(s)$ Included	4-22
4.17.	Longitudinal Closed-Loop Disturbance Response	4-23
4.18.	Longitudinal Channel Simulink Model	4-24
4.19.	Longitudinal Tracking and Disturbance Responses	4-25
4.20.	Longitudinal Tracking Response $10\frac{deg}{sec}$ Reference	4-26

Figure Page

4.21. Longitudinal Response $\zeta_e = 0.5$ 4-27

4.22. Block Diagram of Elevator Response to Reference Input 4-28

4.23. Frequency Response of Elevator to a Reference Input 4-29

4.24. Block Diagram of Elevator Response to Sensor Noise 4-29

4.25. Frequency Response of Elevator to Sensor Noise 4-30

4.26. Response of the Lambda to Pitch Sensor Noise 4-31

5.1. Lateral Plant and Actuator Dynamics 5-3

5.2. Lateral PCT Implementation 5-4

5.3. Lateral $\mathbf{P}_l(s)$ Frequency Responses 5-5

5.4. Lateral $\mathbf{P}_d(s)$ Frequency Responses 5-6

5.5. Weighting Matrix Effect on Open-Loop Response 5-7

5.6. Lateral $\mathbf{P}_e(s)$ Frequency Responses 5-8

5.7. m^2 Equivalent MISO Loops 5-11

5.8. Frequency Responses of $q_{22}(s)$ (left) and $q_{33e}(s)$ (right) 5-11

5.9. Lateral Plant Templates - Roll Channel 5-13

5.10. Lateral Plant Templates - Yaw Channel 5-13

5.11. Nominal Open-Loop Transmissions - Roll Channel 5-15

5.12. Nominal Open-Loop Transmissions - Yaw Channel 5-15

5.13. Roll Channel Final Loop-Shape 5-17

5.14. Yaw Channel Final Loop-Shape 5-18

5.15. Lateral Controller Frequency Responses 5-19

5.16. Roll and Yaw Channel Closed-Loop Frequency Responses 5-20

5.17. Lateral Prefilter Frequency Responses 5-22

5.18. Roll Channel Open-Loop Transmission with $G_{22}(s)$ Included 5-22

5.19. Yaw Channel Open-Loop Transmission with $G_{33}(s)$ Included 5-23

5.20. Lateral Disturbance 5-23

5.21. Lateral Channel Simulink Model 5-24

Figure Page

5.22. Roll Channel Tracking Response 5-25

5.23. Yaw Channel Tracking Response 5-26

5.24. Lateral Channel Disturbance Response 5-27

5.25. Roll Channel Tracking Response 40$\frac{deg}{sec}$ Reference 5-27

5.26. Block Diagram of Aileron Output/Reference Input 5-28

5.27. Frequency Response of Aileron to Reference 5-29

5.28. Block Diagram of Aileron Output/Roll Sensor Noise Input 5-29

5.29. Frequency Response of Aileron to Sensor Noise 5-30

5.30. Block Diagram of Rudder Output/β Sensor Noise Input 5-31

5.31. Frequency Response of Rudder to β Sensor Noise 5-31

5.32. Response of the Lambda to Roll Sensor Noise 5-32

5.33. Response of the Lambda to Beta Sensor Noise 5-33

6.1. Autopilot Simulink Model 6-2

6.2. Autopilot Response to Elevator Deflection 6-4

6.3. Autopilot Response to 45° Roll Command 6-5

6.4. Autopilot Response to 10° 2 Second Pulse Roll Doublet 6-6

6.5. Autopilot Response to 10° Pitch Rate Command 6-7

6.6. Autopilot Response to 10° 2 Second Pulse Pitch Doublet 6-8

6.7. Autopilot Response to 5° Sideslip Command 6-9

6.8. Autopilot Response to 10° 2 Second Pulse Sideslip Doublet 6-10

List of Tables

Table		Page
1.1.	Upper and Lower Tracking Bounds	1-6
2.1.	Lambda's Physical Characteristics	2-3
4.1.	Sixteen Final Longitudinal Flight Conditions	4-13
5.1.	Thirteen Final Lateral Flight Conditions	5-12
B.1.	Initial Longitudinal Flight Conditions	B-1
B.2.	Initial Lateral Flight Conditions	B-2

AFIT/GE/ENG/93D-18

Abstract

This thesis describes the application of the multiple-input multiple-ouput (MIMO) Quantitative Feedback Theory (QFT) design technique to the design of a digital flight control system for the Lambda Unmanned Research Vehicle (URV). The QFT technique allows the synthesis of a control system which is robust in the presence of structured plant uncertainties. Uncertainties considered in this design are the aircraft's plant variation within the flight envelope and the effects of damage to aircraft control surfaces. Mathematical models of control surface failure effects on aircraft dynamics are derived and used to modify an existing small perturbation model of the Lambda. The QFT technique is applied to design a control system utilizing aircraft pitch rate, roll rate and sideslip angle as feedback variables. The inherent cross-coupling rejection qualities of QFT and an aileron-rudder interconnect are utilized to design a control system which results in a coordinated flight. An outer-loop autopilot is then designed around the QFT controller to further assist turn coordination. Sensor noise effects on aircraft states are also analyzed.

DESIGN OF A FLIGHT CONTROLLER FOR AN UNMANNED RESEARCH VEHICLE WITH CONTROL SURFACE FAILURES USING QUANTITATIVE FEEDBACK THEORY

I. Introduction

1.1 Background

The Lambda Unmanned Research Vehicle (URV) is an asset of the Control Systems Development Branch of Wright Laboratory (WL/FIGS), Wright-Patterson AFB, Ohio. WL/FIGS developed Lambda to test new flight control concepts and devices. Because tests on manned vehicles are expensive, WL/FIGS designed Lambda to offer a low cost, safe alternative to such flights. When WL/FIGS flight tests a new flight system, pilots located on the ground send commands to the Lambda via radio transmitter. The output of the sensors on-board the vehicle are transmitted, through telemetry, to a ground station in order to be recorded for subsequent analysis. New flight control methods are tested on Lambda with the hope that, if successful, these same robust control systems may be further developed and implemented on operational Air Force aircraft.

Several successful aircraft flight compensators (analog control system) and flight controllers (digital control system), both denoted by G, have been designed for the Lambda using a feedback design technique called Quantitative Feedback Theory (QFT). This design method guarantees desired plant response in the presence of structured plant parameter uncertainties. QFT has been used to achieve numerous robust aircraft flight control system designs. Most designs using QFT

have focused on structured uncertainties associated with varying flight conditions. WL/FIGS has investigated and is investigating the feasibility of utilizing a single QFT designed G that maintains the aircraft response within specified limits with and without control surface failures. Since this thesis involves a digital control system, G is henceforth referred to as the controller.

A flight controller that guarantees performance under degraded conditions such as control surface failures is of great benefit. Such a controller can greatly reduce pilot effort, increase aircraft stability margins, and aid in successful aircraft recovery if implemented on manned aircraft. Implementing a controller with these qualities on a test vehicle is the first step in assessing its feasibility as a viable controller.

1.2 Problem

The objective of this thesis is to design a digital flight controller to be implemented on the Lambda's microprocessor-based digital flight control system. The controller is to maintain Lambda performance in the yaw, pitch and roll channels with and without control surface failures. Control surfaces considered are elevators, ailerons and rudders. Dr. Meir Pachter has shown that control surface failures alter aircraft stability derivatives in the same manner as varying flight conditions [1]. This relation is essential to allow the application of QFT design methods to control surface failures. The design addresses failures at all points of the flight envelope for the Lambda. Parameters defining the flight envelope consist of aircraft center of gravity location, airspeed, altitude, and weight.

A reasonable set of failure modes are determined. WL/FIGS wants to determine which control surfaces can fail and still allow the controller to meet performance specifications. Control surface

failures are modeled as a loss of surface area. This type of failure is more difficult to handle than an actuator failure which simply freezes the control surface.

It is desired to design a controller which not only adequately controls the aircraft in the presence of control surface failures, but also maintains a coordinated flight. Coordinated flight is defined as flight which minimizes sideslip angle. An outer-loop autopilot is designed around the QFT controller to perform the coordination function.

1.3 Summary of Current Knowledge

Most aircraft require a robust flight control system for proper flight performance. Since the acquisition of the Lambda aircraft in 1986, WL/FIGS has sponsored several theses which have designed flight control systems for the Lambda. Capt. David Wheaton wrote a Masters thesis which designs a flight control system for the Lambda using digital Quantitative Feedback Theory [2]. This thesis shows that Quantitative Feedback Theory (QFT) is a viable design method for aircraft flight control systems. The model Wheaton used in his thesis, however, was developed by WL/FIGS using only physical dimensions of the aircraft. This model does not reflect actual flight data too accurately. Lt. Gerald A. Swift, in his Masters thesis work, derived a more accurate Lambda model using actual flight data [3]. Capt. Donald J. Lacey used this improved model in his digital QFT design of a flight controller [4]. This thesis expands the work of Lacey by considering control surface failures as an additional source of uncertainty.

Quantitative Feedback Theory is a robust multi-variable feedback control-system design technique which guarantees system specifications can be met even with structured plant parameter uncertainties [5]. Dr. Isaac Horowitz, formerly of the Weitzman Institute of Science, Rehovet, Israel,

developed QFT theory over the past thirty years. He first formalized procedures in 1979. During this period, numerous methods of feedback design for multiple-input multiple-output (MIMO) systems had been investigated. None, however, addressed the topic of structured plant uncertainty, which is most certainly present in most real-world control systems. While QFT has proven itself as a valid design technique, perhaps its greatest asset is the elimination of much of the guesswork associated with other methods. QFT, in fact, "consists of a succession of direct (no iterations necessary) single-loop design steps" [5]. These characteristics make QFT a natural choice for aircraft flight control system design.

Many QFT designs have been performed on aircraft other than the Lambda. This shows QFT to be a flexible design process. Following is a partial list of AFIT theses which used QFT in the design of flight control systems:

- Adams, J.M. - *Digital QFT Design for the AFTI/F-16*, (1988)
- Hamilton, S.W. - *Digital QFT Design for an Unmanned Research Vehicle*, (1987)
- Kobylarz, T.S. - *Flight Controller Design with Nonlinear Aerodynamics, Large Parameter Uncertainty, and Pilot Compensation*, (1988)
- Miller, R.B. - *Multiple-Input Multiple-Output Control System Design for the YF-16 Using Nonlinear QFT and Pilot Compensation*, (1990)
- Neumann, K.N. - *A Digital QFT Design for the Control Reconfigurable Combat Aircraft*, (1988)
- Ott, P.T. - *URV Reconfiguration using Digital QFT*, (1988)
- Rasmussen, S.J. - *Application of non-linear QFT to Flight Control Design for High Angle of Attack Maneuvers with Thrust Vectoring*, (1991)

- Russell, H.H. - *Analog QFT Design for the KC-135*, (1984)

1.4 Assumptions

It is assumed that a linear time-invariant (LTI) minimum-phase (m.p.) model for each flight condition accurately reflects Lambda performance. This limits aircraft maneuvers to low angles-of-attack. The Lambda is designed to fly at low angles-of-attack so this assumption is valid. In using an LTI model, the following conditions are assumed [6]:

- Time spans are short (30 - 60 seconds) and perturbations small.
- The aircraft is assumed to be a rigid body (mass and mass distribution are constant).
- The reference coordinate system used is a rotating system centered at the aircraft center of mass.
- In the horizontal plane, the aircraft is symmetrical about the center of the fuselage (no cross-coupling of the longitudinal and lateral directional equations of motion).

This design also assumes the following properties of the Lambda:

- All inputs (control surface deflections) are measurable.
- Aircraft orientation, rate and sideslip angle signals are available.
- A digital sampling rate of 50 Hz is used for the Lambda flight control system.

1.5 Scope

The objective of this thesis is to develop controller difference equations which satisfactorily control Lambda over the entire flight envelope, allowing for possible partial control surface failures.

The design ends when the computer simulations show Lambda, with partial control surface failures, responding within specifications, to control surface inputs.

1.6 Standards

The controller is designed to meet frequency domain tracking specifications set by WL/FIGS. Tracking specifications are given in the frequency domain and are shown in Table 1.1, where T_u is the upper bound of the closed-loop system's transfer function and T_l is the lower bound. The controller is required to maintain a 45 degree phase margin angle for all responses.

It may be difficult or impossible to meet the given specifications for certain control surface failures. In these instances, the controller will guarantee aircraft plant stability only.

Table 1.1 Upper and Lower Tracking Bounds

Channel	T_u	T_l
pitch	$\frac{100}{s^2+8s+100}$	$\frac{320}{s^3+21s^2+144s+320}$
roll	$\frac{s+100}{s^2+18s+100}$	$\frac{35}{s^2+12s+35}$
yaw	$\frac{9}{s^2+3s+9}$	$\frac{18}{s^3+7.4s^2+19.8s+18}$

1.7 Approach/Methodology

Any control system design begins with the generation of accurate mathematical models. As part of his thesis work, Swift wrote several *Matlab* macros to generate plant models for various flight conditions. These macros will be used to generate plant data for this design. Swift's macros were not written to generate plants with control surface failures. Therefore, the macros are modified to account for the change in stability derivatives caused by the control surface failures.

The longitudinal and lateral-mode models of the aircraft are decoupled when no failures are present, allowing the longitudinal and lateral designs to be performed separately. Failure modeling will attempt to maintain a decoupled design. The longitudinal design reduces to a single-input, single-output (SISO) design while the lateral design becomes a two-by-two multiple-input, multiple-output (MIMO) design. Elevator and pitch rate are the inputs and outputs, respectively, for the longitudinal design. Aileron and rudder are the lateral inputs and roll rate and sideslip angle are the lateral outputs. QFT design procedures vary slightly for these two cases.

The procedure for the SISO design case is simpler than the MIMO case. The MIMO design is actually a series of SISO designs, one SISO design for each input to the system [7]. The steps for the entire design process are listed below:

- Determine how failures will affect stability derivatives
- Alter Swift macro appropriately
- Determine desired flight conditions (including control surface failures)
- Generate aircraft plants
- Form pseudo-continuous time equivalent transfer function
- Generate frequency response data
- Plot templates
- Alter flight conditions as necessary to fill out template (repeat above 4 steps until satisfied)

At this point, the SISO and MIMO design procedures begin to differ. The SISO procedure is listed first [8]:

- Choose nominal plant
- Form stability and performance bounds

- Determine which plants can meet performance bounds
- Shape nominal loop (design compensator)
- Synthesize prefilter
- Transform compensator and prefilter to the Z-plane
- Simulate using designed compensator and prefilter

MIMO design procedure [7]:

- Choose weighting matrix W
- Determine the plant transfer function matrix, P(s)
- Invert P(s), viz., $P^{-1}(s) = \begin{bmatrix} p_{11}^*(s) & p_{12}^*(s) \\ p_{21}^*(s) & p_{22}^*(s) \end{bmatrix}$
- Calculate Q(s), $Q(s) = \begin{bmatrix} \frac{1}{p_{11}(s)} & \frac{1}{p_{12}(s)} \\ \frac{1}{p_{21}(s)} & \frac{1}{p_{22}(s)} \end{bmatrix}$
- Plot Templates for one input-output pair
- Choose a nominal plant
- Form stability and performance bounds
- Shape nominal loop (design first element of compensator)
- Synthesize first element of the prefilter
- Shape the remaining loops
- Form the remaining compensator and prefilter elements
- Transform compensator and prefilter to the Z-plane
- Simulate using designed compensator and prefilter

1.8 Materials and Equipment

Computer analysis for this thesis is performed on the Sun SPARCstation 2 workstations available at both the Air Force Institute of Technology and Wright Laboratories. Software packages used are *Matlab* with *Simulink* and the AFIT MIMO/QFT CAD package.

1.9 Other Support

Dr Meir Pachter, Dr Constantine Houpis, and Capt Stuart Sheldon have all served on the thesis committe. Dr Pachter and Dr Houpis are committee co-chairmen. Mr Richard Sating assisted in using the AFIT MIMO/QFT CAD package.

II. The Lambda Aircraft

2.1 The Aircraft

The Lambda URV, shown in Fig. 2.1, is a small remotely-piloted airplane with a 14 foot wing span and weight of approximately 200 pounds. It uses a pusher propeller and a conventional horizontal tail. The horizontal tail consists of a horizontal stabilizer and a split elevator. The vertical tail is located on either end of the horizontal tail, and consists of a vertical stabilizer and rudder. The wings are slightly tapered; each has three trailing, movable control surfaces. See Table 2.1 for Lambda's characteristics.

Lambda has ten control surfaces. They are:

- Left Elevator
- Right Elevator
- Left Rudder
- Right Rudder
- Left Aileron
- Right Aileron
- Left Outer Flap
- Right Outer Flap
- Left Inner Flap
- Right Outer Flap

Figure 2.1 Lambda Schematic

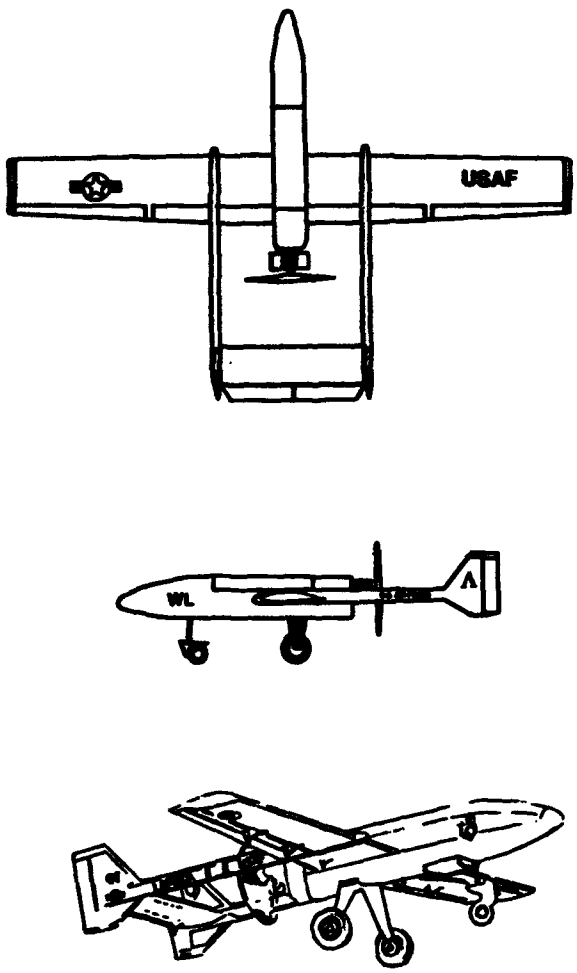

Table 2.1 Lambda's Physical Characteristics

Dimensions	Wing Span.....	14 ft
	Wing Area.....	19 sq ft
	Length.....	9.6 sq ft
	Height With Landing Gear.....	3 ft
	Propeller Diameter.....	2.3 ft
Weights	Maximum Fuel.....	14 lb
	Maximum Payload.....	15 lb
	Maximum Flight Weight.....	210 lb
Performance	Maximum Level Speed at Sea Level.	115 mph (100 knots)
	Stall Speed.....	63 mph (55 knots)
	Stall Speed With Flaps.....	52 mph (45 knots)
Engine	Power.....	18 hp
	Type.....	2 cycle, 2 cylinder
Control Limits	Elevator Deflection Limit.....	$\pm$15 deg
	Rudder Deflection Limit.....	$\pm$25 deg
	Flap Deflection Limit.....	20 deg down
	Aileron Deflection Limit.....	$\pm$15 deg

Although each control surface can operate independently, flight data used to create the mathematical model upon which this design is based are obtained with all four of the flap control surfaces operating together, as are the rudders. The split elevators were deflected together while the ailerons were operated differentially. Flaps are not used as a control surface. Thus, the region of flight investigated in this thesis is during cruise flight conditions since flaps are not involved as control surfaces at this point of flight.

2.2 The Model

Lt Gerald Swift developed a small perturbations model of the Lambda based on data gathered during a series of flight tests [3]. The model first calculates the standard aircraft stability derivatives for the Lambda based on the desired flight condition. The derivatives are then placed into a state-space representation. The model is generated with a *Matlab* macro written by Swift. Capt Steve

Rasmussen of Wright Laboratories later modified some derivatives in the model to better fit recent flight tests. The model describes the aircraft dynamics with eight states, four states for both the longitudinal and lateral channels. The original model is derived assuming that the longitudinal and lateral channels are decoupled. The longitudinal states are u, α, q, and θ. Lateral states are β, p, ϕ and r.

Swift's macro generates an aircraft model for an undamaged aircraft. When control surface damage occurs, the model changes according to the degree of damage. The mathematical derivation of these changes is presented in Chapter III. The changes are incorporated into Swift's macro. The modified macro which calculates damaged aircraft models is presented in Appendix A.

The state-space representation generated by the macro is of the following general form:

$$\dot{\mathbf{x}}(t) = \mathbf{A}(t)\mathbf{x}(t) + \mathbf{B}(t)\mathbf{u}(t) \tag{2.1}$$

$$\mathbf{y}(t) = \mathbf{C}\mathbf{x}(t) \tag{2.2}$$

where $\mathbf{x}(t)$ is an $8x1$ vector of aircraft states, $\mathbf{u}(t)$ is a $3x1$ vector of inputs. $\mathbf{A}(t)$ and $\mathbf{B}(t)$ are $8x8$ and $8x3$ matrices respectively. Because the output of the system, $\mathbf{y}(t)$, is simply the aircraft states, $\mathbf{C}(t)$ is an $8x8$ identity matrix.

Assuming zero initial conditions ($x_o = 0$) and trimmed flight ($\dot{x}_o = 0$), the Laplace transform of the plant is the perturbation model:

$$s\mathbf{X}(s) = \mathbf{A}(s)X(s) + \mathbf{B}(s)\mathbf{U}(s) \tag{2.3}$$

$$\mathbf{Y}(s) = \mathbf{C}(s)\mathbf{X}(s) \tag{2.4}$$

where:

$$\mathbf{A}(s) = \begin{bmatrix} \mathbf{A}(s)_{long} & 0 \\ 0 & \mathbf{A}(s)_{lat} \end{bmatrix} \qquad \mathbf{B}(s) = \begin{bmatrix} \mathbf{B}(s)_{long} \\ \mathbf{B}(s)_{lat} \end{bmatrix} \tag{2.5}$$

$$\mathbf{C}(s) = \begin{bmatrix} \mathbf{C}(s)_{long} & \mathbf{C}(s)_{lat} \end{bmatrix} \tag{2.6}$$

and

$$\mathbf{X}(s) = \begin{bmatrix} u \\ \alpha \\ q \\ \theta \\ \beta \\ p \\ \phi \\ r \end{bmatrix} \qquad \mathbf{U}(s) = \begin{bmatrix} \delta_e \\ \delta_a \\ \delta_r \end{bmatrix} \tag{2.7}$$

2.3 Actuators and Sensors

Three actuator models are used in the mathematical model of the Lambda; one each for the elevator, aileron and rudder. Only one actuator model is necessary for each pair of control surfaces since each pair operates in tandem. Models were constructed by Wright Laboratories based on actual flight data. The elevator model is:

$$\frac{136.2}{s + 10.81 \pm j7.74} \tag{2.8}$$

The aileron model is:

$$\frac{216.84}{s + 11.07 \pm j10.09} \tag{2.9}$$

The rudder model is:

$$\frac{3.906}{s + 4.4372} \tag{2.10}$$

Note that the D.C. gain $\neq 1$

Sensors used to measure aircraft states are not modeled explicitly in Swift's original macro. Therefore, the dynamics of all the sensors are included in the model.

III. Control Surface Failure Modeling

When damage to control surfaces occurs, an aircraft loses the ability to generate moments about its axes. The aircraft also experiences a change in its dynamic response because the loss of an aerodynamic surface changes the stability derivatives of the aircraft. This chapter derives the theory which describes the changes in stability and control derivatives when control surface damage occurs. The derived equations are then implemented in the *Matlab* macro used to generate aircraft models. The original macro was written by Lt Gerald Swift in his thesis. The original macro calculates all aircraft dimensional and non-dimensional stability derivatives for an undamaged aircraft at given flight conditions. The "failed" stability derivatives (denoted with subscript F) are expressed in terms of the "unfailed" stability derivatives (denoted with subscript UF).

3.1 Longitudinal Derivatives

The Lambda has two sets of longitudinal control surfaces; the elevators and flaps. Flaps are used primarily for take-off and landing maneuvers. Because this thesis investigates flight control at cruise flight conditions, only the elevator is considered.

The variable ζ_e is defined as the damage level to the elevators. Damage to be considered is in the form of lost surface area. Such damage on an aircraft might occur as the result of enemy fire. ζ_e is the percentage of elevator surface area which remains after being damaged. When $\zeta_e = 1$, no damage has occurred. When $\zeta_e = 0$ both elevators are completely blown off. If elevators are damaged equally no coupling to the lateral channel exists. Unequal damage, though, creates a lateral moment. For modeling purposes, this analysis assumes only one elevator is damaged at any

one time. Therefore, the range $0.5 \leq \zeta_e \leq 1$ is used in this thesis. Ensuing channel coupling is discussed in more detail in Section 3.3.1.

The effects of failure can be determined by analyzing the three non-dimensionalized longitudinal equations of motion as given in Blakelock [Eq (1-59)].

$$(\frac{mU}{S\bar{q}}\dot{u} - C_{x_u}u) + (-\frac{c}{2U}C_{x_{\dot{\alpha}}}\dot{\alpha} - C_{x_\alpha}\alpha) + [-\frac{c}{2U}C_{x_q}\dot{\theta} - C_w(cos\Theta)\theta] = C_{x_{\delta_e}}\delta_e \quad (3.1)$$

$$-(C_{z_u}u) + [(\frac{mU}{S\bar{q}} - \frac{c}{2U}C_{z_{\dot{\alpha}}})\dot{\alpha}] - C_{z_\alpha}\alpha + [(-\frac{mU}{S\bar{q}} - \frac{c}{2U}C_{z_q})\dot{\theta} - C_w(sin\Theta)\theta] = C_{z_{\delta_e}}\delta_e \quad (3.2)$$

$$-(C_{m_u}u) + (-\frac{c}{2U}C_{m_{\dot{\alpha}}}\dot{\alpha} - C_{m_\alpha}\alpha) + (\frac{I_y}{S\bar{q}c}\ddot{\theta} - \frac{c}{2U}C_{m_q}\dot{\theta}) = C_{m_{\delta_e}}\delta_e \quad (3.3)$$

The C_{i_j} terms are the non-dimensional stability derivatives. These derivatives describe the longitudinal dynamics of the aircraft. They will change when elevator damage occurs.

Some simplifying assumptions are made. Fuselage effects are assumed negligible. Also, effects on the derivatives in Eq. (3.1) can be assumed negligible as changes in elevator surface area create negligible forces in the x direction. This leaves only derivatives in the Z-equation [Eq. (3.2)] and the M-equation [Eq. (3.3)] to be analyzed. The effect on C_w can also be neglected because this term is related to gravity only.

3.1.1 M Equation Analysis. Failure effects on several derivatives in Eq. (3.3) are assumed negligible: C_{m_u} is due mostly to lift on the wing. Elevator damage has negligible effect on this term. Because the final control system will still have a pilot in the loop, only short term dynamics are a concern. Partials of u are only present in phugoid dynamics. For this reason also, failure effects on C_{m_u} can be neglected. This assumption is based on the fact that no spillover of phugoid

poles occurs when loops are closed. Final simulations will verify that no spillover of short-period and phugoid dynamics exists.

$C_{m_{\dot{\alpha}}}$ accounts for downwash effects. It also changes negligibly when elevator damage occurs. Unsteady dynamics associated with $\dot{\alpha}$ are neglected.

The above discussion leaves three short-period derivatives which must be modeled for failures, C_{m_α}, C_{m_q} and $C_{m_{\delta_e}}$. The change in C_{m_α} is derived first. Two forces cause moments about the center of gravity. These moments are caused by the lift on the wing and the lift on the tail. Each moment can be expressed as:

$$M_{wing} = \frac{\bar{q}}{I_x} S_w a_w \Delta X_{cg} \alpha \tag{3.4}$$

$$M_{tail} = \frac{\bar{q}}{I_x} \eta S_t a_t l_t (1-k) \alpha \tag{3.5}$$

Variables l_t and ΔX_{cg} have opposite signs for the Lambda because they are measured aft and forward of the center of gravity, respectively. The total moment about the center of gravity is therefore:

$$M_{total} = M_{wing} + M_{tail}$$

$$M_{total} = \frac{\bar{q}}{I_x} [S_w a_w \Delta X_{cg} + \eta S_t a_t l_t (1-k)] \alpha \tag{3.6}$$

Define $M_{\alpha_{UF}}$ as:

$$M_{\alpha_{UF}} = \frac{\bar{q}}{I_x} [S_w a_w \Delta X_{cg} + \eta S_t a_t l_t (1-k)] \tag{3.7}$$

where $M_{\alpha_{UF}}$ is a dimensional stability derivative for the undamaged aircraft.

If damage occurs to the elevator, less moment is produced by the tail/elevator combination. The change in moment is proportional to the effective area of the horizontal tail. Therefore Eq. (3.5) becomes:

$$M_{tail} = \frac{\bar{q}}{I_z}\zeta_e'\eta S_t a_t l_t(1-k) \tag{3.8}$$

where

$$\zeta_e' = \frac{(\zeta_e - 1)S_e + S_t}{S_t} \tag{3.9}$$

ζ_e' is the ratio of available tail surface area to undamaged tail surface area. When $\zeta_e = 1$ this ratio is 1, thus resulting in a value for M_{tail} being the same as for an undamaged aircraft.

With a damaged elevator, the dimensional stability derivative (M_{α_F}) becomes

$$M_{\alpha_F} = \frac{\bar{q}}{I_z}[S_w a_w \Delta X_{cg} + \zeta_e'\eta S_t a_t l_t(1-k)] \tag{3.10}$$

Because ζ_e' is less than 1 when damage has occurred, it is seen that the magnitude of the moment about the center of gravity is decreased when an elevator loses surface area, as expected.

The effect on C_{m_α} can be expressed in terms of the change in the dimensional stability derivative ΔM_α where

$$\Delta M_\alpha = M_{\alpha_{UF}} - M_{\alpha_F} \tag{3.11}$$

Substituting Eq. (3.7) and (3.10) into (3.11) yields

$$\Delta M_\alpha = \frac{\bar{q}}{I_x}[(1-\zeta_e')\eta S_t a_t l_t(1-k)] \tag{3.12}$$

To non-dimensionalize this change, divide Eq. (3.12) by Eq. (3.10) to yield

$$\frac{\Delta M_\alpha}{M_\alpha} = \frac{(1-\zeta_e^{'})\eta S_t a_t l_t (1-k)}{S_w a_w \Delta X_{cg} + \zeta_e^{'} \eta S_t a_t l_t (1-k)} \tag{3.13}$$

This ratio represents the fraction of $C_{m_{\alpha_{UP}}}$ which has been lost due to damage. Therefore, the first damaged dimensionless stability derivative is

$$C_{m_{\alpha_P}} = C_{m_{\alpha_{UP}}} - C_{m_{\alpha_{UP}}} (\frac{\Delta M_\alpha}{M_\alpha}) \tag{3.14}$$

The terms are subtracted because elevator damage causes a larger moment.

Figure 3.1 shows how M_α varies with damage fraction ζ_e for a representative flight condition.

Figure 3.1 M_α vs. ζ_e

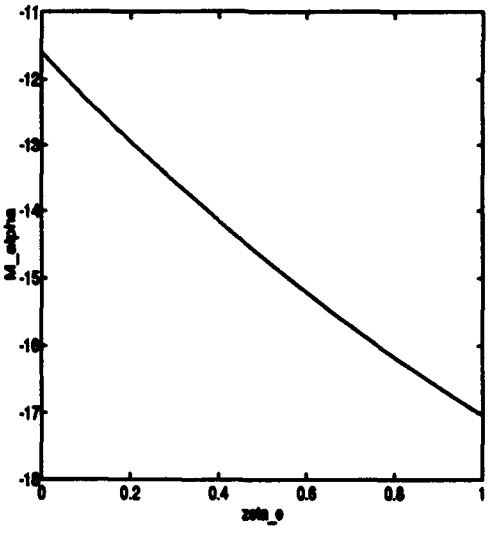

The two remaining stability derivatives of Eq. (3.3) are relatively simple to derive. The first, C_{m_q}, is related to the tail surface area. C_{m_q} depicts damping in pitch motion. Because pitch damping is performed by the tail, the derivative is directly related to effective tail surface area $\zeta_e^{'}$.

$C_{m_{q_F}}$ is therefore a direct proportional function of $C_{m_{qUF}}$.

$$C_{m_{q_F}} = \zeta_e' C_{m_{qUF}} \tag{3.15}$$

$C_{m_{\delta_{eF}}}$ has a similar simple relation. In this case though, the change in the derivative is directly related to the portion of total elevator area which has been lost, not to the effective area of the tail.

$$C_{m_{\delta_{eF}}} = \zeta_e C_{m_{\delta_{eUF}}} \tag{3.16}$$

3.1.2 Z Equation Analysis. Forces in the z-axis direction are described in Eq. (3.2) which is repeated here:

$$-(C_{z_u} u) + [(\frac{mU}{S\bar{q}} - \frac{c}{2U} C_{z_{\dot{\alpha}}})\dot{\alpha}] - C_{z_\alpha}\alpha + [(-\frac{mU}{S\bar{q}} - \frac{c}{2U} C_{z_q})\dot{\theta} - C_w(sin\Theta)\theta] = C_{z_{\delta_e}}\delta_e \tag{3.17}$$

For the same reasons given for the M equation, failure effects on the partials of u and $\dot{\alpha}$ are neglected. C_w is again negligible as it is related to gravity only.

The C_{z_α} term is similar to the C_{m_α} term. Force in the z-axis is generated by lift on the wing and the tail. Both forces are negative since they act in the negative z direction.

$$Z_{wing} = -\frac{\bar{q}}{m} S_w a_w \tag{3.18}$$

$$Z_{tail} = -\frac{\bar{q}}{m} \eta S_t a_t (1-k) \tag{3.19}$$

The sum of these two forces yields $Z_{\alpha_{UF}}$

$$Z_{\alpha_{UF}} = -\frac{\bar{q}}{m}[S_w a_w + \eta S_t a_t (1-k)] \tag{3.20}$$

Elevator damage affects the force caused by the tail only. The force is proportional to the effective area of the horizontal tail. Therefore Z_{α_F} is shown as:

$$Z_{\alpha_F} = -\frac{\bar{q}}{m}[S_w a_w + \zeta_e' \eta S_t a_t (1-k)] \tag{3.21}$$

The difference in Z_α for the failed and unfailed cases is $\Delta Z_\alpha = Z_{\alpha_{UF}} - Z_{\alpha_F}$:

$$\Delta Z_\alpha = -\frac{\bar{q}}{m}(1-\zeta_e')\eta S_t a_t (1-k) \tag{3.22}$$

The above relation is divided by Eq. (3.21) to yield:

$$\frac{\Delta Z_\alpha}{Z_\alpha} = \frac{(1-\zeta_e')\eta S_t a_t (1-k)}{S_w a_w + \zeta_e' \eta S_t a_t (1-k)} \tag{3.23}$$

This ratio is the fraction of C_{z_α} which has been lost to damage.

$$C_{z_{\alpha F}} = C_{z_{\alpha UF}} + C_{z_{\alpha UF}}\left(\frac{\Delta Z_\alpha}{Z_\alpha}\right) \tag{3.24}$$

When the aircraft experiences a pitching motion, changes in lift are generated primarily by the tail. C_{z_q} is therefore proportional to the effective horizontal tail area.

$$C_{z_{qF}} = \zeta_e' C_{z_{qUF}} \tag{3.25}$$

The tail effectiveness $C_{z_{\delta_e}}$ is directly related to available elevator surface area.

$$C_{z_{\delta_{eF}}} = \zeta_e C_{z_{\delta_{eUF}}} \tag{3.26}$$

3.2 *Lateral Derivatives*

Similar to the longitudinal channel, the Lambda's lateral channel has two sets of control surfaces. Lateral control surfaces are the rudders and ailerons. Both sets are used during routine flight to perform aircraft maneuvers. Both sets are considered in damage analysis.

Two damage variables are defined for the lateral channel, one for each set of control surfaces. Damage entails a loss of surface area and is proportional to the latter. Damage to the ailerons is denoted by ζ_a. Rudder damage is similarly ζ_r. Lateral control surface damage variables account for damage to both surfaces in each pair. For example, if both rudders have lost 25% of their surface area, the total lost is 50%. This means ζ_r is 0.5. Lateral damage can be represented as such because damage to a right or left lateral surface has the same net effect on aircraft dynamics. No coupling of lateral damage to the longitudinal channel exists (see Section 3.3.1).

Failure analysis begins with the three lateral equations of motion. Written in Laplace transform form, from Blakelock [Eq. (3-17)]:

$$-\frac{b}{2U}C_{y_p}\dot{\phi} - C_{y_\phi}\phi + (\frac{mU}{S\bar{q}} - \frac{b}{2U}C_{y_r})\dot{\psi} - C_{y_\psi}\psi + \frac{mU}{S\bar{q}}\dot{\beta} - C_{y_\beta}\beta = C_{y_{\delta_a}}\delta_a + C_{y_{\delta_r}}\delta_r \qquad (3.27)$$

$$\frac{I_x}{S\bar{q}b}\ddot{\phi} - \frac{b}{2U}C_{l_p}\dot{\phi} - \frac{J_{xz}}{S\bar{q}b}\ddot{\psi} - \frac{b}{2U}C_{l_r}\dot{\psi} - C_{l_\beta}\beta = C_{l_{\delta_a}}\delta_a + C_{l_{\delta_r}}\delta_r \qquad (3.28)$$

$$-\frac{J_{xz}}{S\bar{q}b}\ddot{\phi} - \frac{b}{2U}C_{n_p}\dot{\phi} + \frac{I_z}{S\bar{q}b}\ddot{\psi} - \frac{b}{2U}C_{n_r}\dot{\psi} - C_{n_\beta}\beta = C_{n_{\delta_a}}\delta_a + C_{n_{\delta_r}}\delta_r \qquad (3.29)$$

It is seen that stability derivatives exist for the ϕ, ψ, p, r and β states. These derivatives describe the lateral dynamics of the aircraft. These will change when aileron and/or rudder damage occurs.

Like the longitudinal channel, fuselage effects on the control derivatives are assumed negligible. C_{l,n_ϕ} and C_{l,n_ψ} denote the change in the respective moments due to a change in aircraft orientation. These four derivatives are always zero. They are not considered in this analysis.

3.2.1 Y Equation Analysis. The Y equation is repeated here:

$$-\frac{b}{2U}C_{y_p}\dot{\phi} - C_{y_\phi}\phi + (\frac{mU}{S\bar{q}} - \frac{b}{2U}C_{y_r})\dot{\psi} - C_{y_\psi}\psi + \frac{mU}{S\bar{q}}\dot{\beta} - C_{y_\beta}\beta = C_{y_{\delta_a}}\delta_a + C_{y_{\delta_r}}\delta_r \tag{3.30}$$

The failed derivatives for p, r and β are directly proportional to the unfailed derivatives. These derivatives measure the force in the y direction created by the respective state. Only the effective area of the vertical fins creates a force in the y direction. Therefore:

$$C_{y_{pF}} = \zeta_r' C_{y_{pUF}} \tag{3.31}$$

$$C_{y_{rF}} = \zeta_r' C_{y_{rUF}} \tag{3.32}$$

$$C_{y_{\beta F}} = \zeta_r' C_{y_{\beta UF}} \tag{3.33}$$

where

$$\zeta_r' = \frac{(\zeta_r - 1)S_r + S_f}{S_f} \tag{3.34}$$

is the effective area of the vertical fin with rudder damage.

The two derivatives for the control surfaces themselves are proportional to the area lost on each control surface. As each of these derivatives is a measure of control surface effectiveness, the effectiveness is reduced proportionally to the available control surface area.

$$C_{y_{\delta_r F}} = \zeta_r C_{y_{\delta_r UF}} \tag{3.35}$$

$$C_{y_{\delta_a F}} = \zeta_a C_{y_{\delta_a UF}} \tag{3.36}$$

For the aircraft model being used, $C_{y_{\delta_a UF}} = 0$ for all cases.

3.2.2 L Equation Analysis. The L moment equation [Eq. (3.28)] is repeated here:

$$\frac{I_x}{S\bar{q}b}\ddot{\phi} - \frac{b}{2U}C_{l_p}\dot{\phi} - \frac{J_{xz}}{S\bar{q}b}\ddot{\psi} - \frac{b}{2U}C_{l_r}\dot{\psi} - C_{l_\beta}\beta = C_{l_{\delta_a}}\delta_a + C_{l_{\delta_r}}\delta_r \tag{3.37}$$

The C_{l_p} derivative is proportional to lateral control surface failure. This derivative is unique in that it can be altered by failures in either the aileron or rudder. This results from the fact that both the wings and vertical fins damp rolling motion. The proportion factor ζ_{ar} is the effective area of the wings and vertical fins.

$$\zeta_{ar} = \frac{(\zeta_a - 1)S_a + (\zeta_r - 1)S_r + S_w + S_f}{S_w + S_f} \tag{3.38}$$

The failed value of C_{l_p} is therefore

$$C_{l_{pF}} = \zeta_{ar}C_{l_{pUF}} \tag{3.39}$$

The other two rate derivatives are both proportional to the effective tail area. Only the vertical tails provide damping due to r or β movement.

$$C_{l_{rF}} = \zeta_r' C_{l_{rUF}} \tag{3.40}$$

$$C_{l_{\beta F}} = \zeta_r' C_{l_{\beta UF}} \tag{3.41}$$

The control surface derivatives are directly related to their respective control surface areas.

$$C_{l_{\delta aF}} = \zeta_r C_{l_{\delta aUF}} \tag{3.42}$$

$$C_{l_{\delta rF}} = \zeta_a C_{l_{\delta rUF}} \tag{3.43}$$

3.2.3 N Equation Analysis. The N moment equation [Eq. (3.29)] is repeated here:

$$-\frac{J_{xz}}{S\bar{q}b}\ddot{\phi}-\frac{b}{2U}C_{n_p}\dot{\phi}+\frac{I_z}{S\bar{q}b}\ddot{\psi}-\frac{b}{2U}C_{n_r}\dot{\psi}-C_{n_\beta}\beta=C_{n_{\delta_a}}\delta_a+C_{n_{\delta_r}}\delta_r \tag{3.44}$$

All of the N equation rate derivatives are proportional to the effective vertical fin area ζ_r'. The vertical fin is the only surface which has an effect on moments about the z-axis.

$$C_{n_{pF}}=\zeta_r' C_{n_{rUF}} \tag{3.45}$$

$$C_{n_{rF}}=\zeta_r' C_{n_{rUF}} \tag{3.46}$$

$$C_{n_{\beta F}}=\zeta_r' C_{n_{\beta UF}} \tag{3.47}$$

The control surface derivatives are directly related to their respective control surface areas.

$$C_{n_{\delta_a F}}=\zeta_r C_{n_{\delta_a UF}} \tag{3.48}$$

$$C_{n_{\delta_r F}}=\zeta_a C_{n_{\delta_r UF}} \tag{3.49}$$

3.3 Disturbance Modeling

The lateral and longitudinal models both have an external disturbance input. The origins of these disturbances are described.

As shown by Eq. (2.3), the equations of motion for both the longitudinal and lateral channels are written in state-space form as

$$s\mathbf{X}(s) = \mathbf{A}(s)\mathbf{X}(s) + \mathbf{B}(s)\mathbf{U}(s) \tag{3.50}$$

where $\mathbf{X}$ is the state vector for the channel in question. Because the model is time invariant, the $\mathbf{A}$ and $\mathbf{B}$ matrices are not functions of s and they are hence so defined.

Eq. (3.50) is augmented to include disturbances as

$$s\mathbf{X}(s) = \mathbf{A}\mathbf{X}(s) + \mathbf{B}\mathbf{U}(s) + \mathbf{\Gamma}d(s) \tag{3.51}$$

where $\mathbf{\Gamma}$ is a disturbance input matrix and d is the disturbance input(s). In the following sections, the disturbance input matrices $\mathbf{\Gamma}_{lat}$ and $\mathbf{\Gamma}_{lng}$ are determined for the lateral and longitudinal channels, respectively.

First consider damage to lateral control surfaces. If the rudder loses surface area, the rudder loses ability to create a yawing moment. The effect on the lateral channel is described in Sec. 3.2. The configuration of the two rudders does not allow it to create a pitching moment, even when one rudder is damaged more than the other. Thus a rudder failure does not cause a coupling disturbance in either the lateral or longitudinal channels.

The location of the ailerons, parallel to the y-axis, allows the ailerons to create a pitching moment if both ailerons do not create the same moment about the y-axis. If one aileron has less surface area than the other, unequal pitching moments occur. However, aileron failures are not modeled as coupling into the longitudinal channel because the moment caused by the ailerons is a small fraction of the moment caused by the wing. Tail moments already counter the wing moments.

Therefore, only elevator failures are modeled as disturbances.

3.3.1 Lateral Disturbance. Swift's models for an undamaged aircraft assume that the longitudinal and lateral modes are uncoupled. This is a valid approximation for the undamaged aircraft. However, the possibility of coupling must be considered for a damaged aircraft. Loss of surface area may cause paired control surfaces to exert unequal moments about the other channel's axes.

The effect of damage to the elevator is considered. The left and right elevator of the Lambda are located on the horizontal tail trailing edge. The elevators share a common inside edge. The elevators move together when deflected to produce a moment. Because the elevators are symmetric about the x-axis of the aircraft, no lateral moments are produced. If one elevator operates with less surface area, it produces less moment about the x-axis than the undamaged elevator. The net result is a coupling into the lateral channel in the form of a moment about the x-axis. This moment is considered to be significant and therefore is included in the aircraft model.

The coupling of an elevator failure to the lateral mode is modeled as a disturbance to the lateral states. By modeling as a disturbance, the designed QFT controller attenuates the effect of this moment on the output, maintaining an essentially uncoupled system.

An elevator deflection which contributes an x-axis moment does so in much the same manner as an aileron deflection. The elevator "effectiveness" can be introduced into Eq. (3.28). This additional term is the moment about the x-axis added by an elevator deflection. In this case, δ_e is the elevator deflection from horizontal, not from trim. Note that $\ddot{\phi} = \dot{p}$, $\ddot{\psi} = \dot{r}$, $\dot{\phi} = p$ and $\dot{\psi} = r$.

$$\frac{I_x}{S\bar{q}b}\dot{p} - \frac{b}{2U}C_{l_p}p - \frac{J_{xz}}{S\bar{q}b}\dot{r} - \frac{b}{2U}C_{l_r}r - C_{l_\beta}\beta = C_{l_{\delta_a}}\delta_a + C_{l_{\delta_r}}\delta_r + C_{l_{\delta_e}}\delta_e \tag{3.52}$$

The above equation is placed into state space form. This requires solving Eq. (3.52) for $\dot{p}$ as follows:

$$\frac{I_x}{S\bar{q}b}\dot{p} = \frac{b}{2U}C_{l_p}p + \frac{J_{xz}}{S\bar{q}b}\dot{r} + \frac{b}{2U}C_{l_r}r + C_{l_\beta}\beta + C_{l_{\delta_a}}\delta_a + C_{l_{\delta_r}}\delta_r + C_{l_{\delta_e}}\delta_e \tag{3.53}$$

$$\dot{p} = \frac{S\bar{q}b^2}{2I_xU}C_{l_p}p + \frac{J_{xz}}{I_x}\dot{r} + \frac{S\bar{q}b^2}{2I_xU}C_{l_r}r + \frac{S\bar{q}b}{I_x}C_{l_\beta}\beta + \frac{S\bar{q}b}{I_x}C_{l_{\delta_a}}\delta_a + \frac{S\bar{q}b}{I_x}C_{l_{\delta_r}}\delta_r + \frac{S\bar{q}b}{I_x}C_{l_{\delta_e}}\delta_e \tag{3.54}$$

Equation (3.54) is now written in terms of its dimensional derivatives.

$$\dot{p} = L_p p + \frac{J_{xz}}{I_x}\dot{r} + L_r r + L_\beta \beta + L_{\delta a}\delta_a + L_{\delta r}\delta_r + L_{\delta e}\delta_e \tag{3.55}$$

The L and N equations are coupled equations. Therefore, to place in state space form, $\dot{r}$ must be expressed in terms of the other states and $\dot{p}$. This equation is then substituted into Eq. (3.55). Notice no $C_{n_{\delta_e}}$ term is included. Elevator deflection is assumed to create a negligible yaw moment. Equation (3.29) is now solved for $\dot{r}$.

$$-\frac{J_{xz}}{S\bar{q}b}\dot{p} - \frac{b}{2U}C_{n_p}p + \frac{I_z}{S\bar{q}b}\dot{r} - \frac{b}{2U}C_{n_r}r - C_{n_\beta}\beta = C_{n_{\delta_a}}\delta_a + C_{n_{\delta_r}}\delta_r \tag{3.56}$$

$$\frac{I_x}{S\bar{q}b}\dot{r} = \frac{J_{xz}}{S\bar{q}b}\dot{p} + \frac{b}{2U}C_{n_p}p + \frac{b}{2U}C_{n_r}r + C_{n_\beta}\beta + C_{l_{\delta_a}}\delta_a + C_{l_{\delta_r}}\delta_r \tag{3.57}$$

$$\dot{r} = \frac{J_{xz}}{I_x}\dot{p} + \frac{S\bar{q}b^2}{2I_xU}C_{n_p}p + \frac{S\bar{q}b^2}{2I_xU}C_{n_r}r + \frac{S\bar{q}b}{I_x}C_{n_\beta}\beta + \frac{S\bar{q}b}{I_x}C_{l_{\delta_a}}\delta_a + \frac{S\bar{q}b}{I_x}C_{l_{\delta_r}}\delta_r \tag{3.58}$$

This equation is now written in terms of dimensional derivatives:

$$\dot{r} = \frac{J_{xz}}{I_z}\dot{p} + N_p p + N_r r + N_\beta \beta + N_{\delta a}\delta_a + N_{\delta r}\delta_r \tag{3.59}$$

Substituting Eq. (3.59) into Eq. (3.55) and solving for $\dot{p}$ yields:

$$\dot{p} = (\frac{L_p + \kappa_l N_p}{\Lambda})p + (\frac{L_r + \kappa_l N_r}{\Lambda})r + (\frac{L_\beta + \kappa_l N_\beta}{\Lambda})\beta + (\frac{L_{\delta a} + \kappa_l N_{\delta a}}{\Lambda})\delta_a + (\frac{L_{\delta r} + \kappa_l N_{\delta r}}{\Lambda})\delta_r + (\frac{L_{\delta e}}{\Lambda})\delta_e \tag{3.60}$$

where $\kappa_l = J_{xz}/I_x$ and $\Lambda = 1 - \frac{J_{xz}^2}{I_x I_z}$.

Coupling exists between the L and N moment equations when placed in state-space form. This is evidenced by the presence of both $\dot{r}$ and $\dot{p}$ terms in Els. (3.28) and (3.29). A derivation similar to the one just performed but beginning with the N equation yields a disturbance which affects the r state. Substituting Eq. (3.55) into Eq. (3.59) yields:

$$[1 - \frac{J_{xz}^2}{I_x I_z}]\dot{r} = \frac{J_{xz}}{I_z}[L_p p + L_r r + L_\beta \beta + L_{\delta a}\delta_a + L_{\delta r}\delta_r + L_{\delta e}\delta_e] + N_p p + N_r r + N_\beta \beta + N_{\delta a}\delta_a + N_{\delta r}\delta_r \tag{3.61}$$

$$\dot{r} = (\frac{N_p + \kappa_n L_p}{\Lambda})p + (\frac{N_r + \kappa_n L_r}{\Lambda})r + (\frac{N_\beta + \kappa_n L_\beta}{\Lambda})\beta + (\frac{N_{\delta a} + \kappa_n L_{\delta a}}{\Lambda})\delta_a + (\frac{N_{\delta r} + \kappa_n L_{\delta r}}{\Lambda})\delta_r + (\frac{\kappa_n L_{\delta e}}{\Lambda})\delta_e \tag{3.62}$$

where $\kappa_n = J_{xz}/I_z$ and $\Lambda = 1 - \frac{J_{xz}^2}{I_x I_z}$.

A valid approximation for $L_{\delta e}$ is now derived. The elevator and aileron have approximately the same area. They can therefore be assumed to create the same force when deflected by equal amounts. The moment created about the x-axis, however, is different due to different moment arms. The elevators are approximately $\frac{1}{6}$ the distance from the x-axis as the ailerons. Returning

to the non-dimensional unfailed derivatives allows the following relationship to be derived:

$$C_{l_{\delta eUF}} = \frac{1}{6} C_{l_{\delta eUF}} \tag{3.63}$$

and similarly:

$$L_{\delta eUF} = \frac{1}{6} L_{\delta aUF} \tag{3.64}$$

Because $L_{\delta e}$ is a measure of elevator "effectiveness" in the lateral channel, $L_{\delta eF}$ is a proportion of $L_{\delta eUF}$, that is:

$$L_{\delta eF} = (1 - \zeta_e) L_{\delta eUF} \tag{3.65}$$

which can be written:

$$L_{\delta eF} = \frac{(1 - \zeta_e)}{6} L_{\delta aUF} \tag{3.66}$$

Examination of Eq. (3.60) and Eq. (3.62) shows the contribution of an elevator deflection to the lateral dynamics as:

$$\begin{bmatrix} \dot{\beta} \\ \dot{p} \\ \dot{\phi} \\ \dot{r} \end{bmatrix} = \mathbf{A}_F \begin{bmatrix} \beta \\ p \\ \phi \\ r \end{bmatrix} + \begin{bmatrix} 0 \\ \frac{L_{\delta_a F}}{\Lambda} \\ 0 \\ \frac{\kappa_n L_{\delta_a F}}{\Lambda} \end{bmatrix} \delta_e \tag{3.67}$$

Substituting Eq. (3.66) into Eq. (3.67) yields:

$$\begin{bmatrix} \dot{\beta}_d \\ \dot{p}_d \\ \dot{\phi}_d \\ \dot{r}_d \end{bmatrix} = \mathbf{A}_F \begin{bmatrix} \beta \\ p \\ \phi \\ r \end{bmatrix} + \begin{bmatrix} 0 \\ \frac{(1-\zeta_e) L_{\delta aUF}}{6\Lambda} \\ 0 \\ \frac{\kappa_n (1-\zeta_e) L_{\delta aUF}}{6\Lambda} \end{bmatrix} \delta_e \tag{3.68}$$

The 2x1 Γ_{lat} matrix is now written from Eq. (3.68) as:

$$\Gamma_{lat} = \begin{bmatrix} 0 \\ \frac{(1-\zeta_e)L_{\delta_e UF}}{\delta A} \\ 0 \\ \frac{\kappa_a(1-\zeta_e)L_{\delta_e UF}}{\delta A} \end{bmatrix} \tag{3.69}$$

For disturbance modeling purposes, δ_e is set to the maximum value of elevator deflection.

3.3.2 Longitudinal Disturbance. Elevator damage is modeled as a disturbance in the longitudinal channel also. ior to damage, the elevator is set at a particular trim condition. When damage occurs, forces and moments generated by the elevator trim setting are lost. Thus, the elevator moves to a position different from the trim position for the linearized model. The change in forces and moments are therefore modeled as an elevator deflection.

The moment generated by an undamaged elevator is given as:

$$M_{UF} = \bar{q} S_t a_t \delta_e' \tag{3.70}$$

where δ_e' is used to avoid confusion with the elevator deflections of Eqs. (3.1), (3.2) and (3.3).

When the elevator is failed, the moment is a fraction of available elevator surface area:

$$M_F = \zeta_e \bar{q} S_t a_t \delta_e' \tag{3.71}$$

The moment generated by an undamaged trim setting is:

$$M_{UF} = \bar{q} S_t a_t \delta_{trim} \tag{3.72}$$

where δ_{trim} is referenced to the horizontal tail surface. The trim moment *lost* when elevator damage occurs is a function of the undamaged elevator trim moment:

$$M_F = (1 - \zeta_e)\bar{q}S_t a_t \delta_{trim} \tag{3.73}$$

After damage occurs, the elevator trim adjusts to make up for the lost moments. Equation (3.71) and Eq. (3.73) are therefore set equal to determine the required elevator deflection.

$$\zeta_e \bar{q}S_t a_t \delta_e^{'} = (1 - \zeta_e)\bar{q}S_t a_t \delta_{trim} \tag{3.74}$$

$$\delta_e^{'} \approx \frac{1 - \zeta_e}{\zeta_e}\delta_{trim} \tag{3.75}$$

$\delta_e^{'}$ of Eq. (3.75) is the elevator deflection required to offset the lost trim moments caused by elevator damage. This deflection appears in the longitudinal equations of motion in addition to the standard control deflection δ_e. The effectiveness of $\delta_e^{'}$ is the same as δ_e. The z and $m-$equations are rewritten with the additional moment and force terms. The $x-$equation is neglected because $C_{x_{\delta_e}} = 0$.

$$-(C_{z_u}u) + [(\frac{mU}{S\bar{q}} - \frac{c}{2U}C_{z_{\dot{\alpha}}})\dot{\alpha}] - C_{z_\alpha}\alpha + [(-\frac{mU}{S\bar{q}} - \frac{c}{2U}C_{z_q})\dot{\theta} - C_w(sin\Theta)\theta] = C_{z_{\delta_e}}\delta_e + C_{z_{\delta_e}}\delta_e^{'} \tag{3.76}$$

$$-(C_{m_u}u) + (-\frac{c}{2U}C_{m_{\dot{\alpha}}}\dot{\alpha} - C_{m_\alpha}\alpha) + (\frac{I_y}{S\bar{q}c}\ddot{\theta} - \frac{c}{2U}C_{m_q}\dot{\theta}) = C_{m_{\delta_e}}\delta_e + C_{m_{\delta_e}}\delta_e^{'} \tag{3.77}$$

The additional moments and forces are added because the additional trim deflection creates moments and forces in the same directions as a normal dynamic control deflection.

Similar to the lateral channel disturbances, the above equation needs to be placed in state-space form.

$$\frac{I_y}{S\bar{q}c}\dot{q} = \frac{C_{m_u}}{U}u + (\frac{c}{2U}C_{m_{\dot{\alpha}}}\dot{\alpha} + C_{m_\alpha}\alpha) + \frac{c}{2U}C_{m_q}q) + C_{m_{\delta_e}}\delta_e + C_{m_{\delta_e}}\delta_e' \quad (3.78)$$

$$\dot{q} = \frac{S\bar{q}c}{I_yU}C_{m_u}u + (\frac{S\bar{q}c^2}{2I_yU}C_{m_{\dot{\alpha}}}\dot{\alpha} + \frac{S\bar{q}c}{I_y}C_{m_\alpha}\alpha) + \frac{S\bar{q}c^2}{2I_yU}C_{m_q}q) + \frac{S\bar{q}c}{I_y}C_{m_{\delta_e}}\delta_e + \frac{S\bar{q}c}{I_y}C_{m_{\delta_e}}\delta_e' \quad (3.79)$$

Setting in terms of dimensional derivatives:

$$\dot{q} = M_u u + M_{\dot{\alpha}}\dot{\alpha} + M_\alpha\alpha + M_q q + M_{\delta_e}\delta_e + M_{\delta_e}\delta_e' \quad (3.80)$$

Now Eq. (3.2) is used to solve for $\dot{\alpha}$ and substitute that result into 3.80. Adding the additional trim forces to Eq. (3.2) yields:

$$-(\frac{C_{z_u}}{U}u) + (\frac{mU}{S\bar{q}} - \frac{c}{2U}C_{z_{\dot{\alpha}}})\dot{\alpha} - C_{z_\alpha}\alpha - (\frac{mU}{S\bar{q}} + \frac{c}{2U}C_{z_q})q - C_w(sin\Theta)\theta = C_{z_{\delta_e}}\delta_e + C_{z_{\delta_e}}\delta_e' \quad (3.81)$$

$$\frac{m}{S\bar{q}}(U - \frac{S\bar{q}c}{2Um}C_{z_{\dot{\alpha}}})\dot{\alpha} = \frac{C_{z_u}}{U}u + C_{z_\alpha}\alpha + (\frac{m}{S\bar{q}}(U + \frac{S\bar{q}c}{2Um}C_{z_q})q + C_w(sin\Theta)\theta + C_{z_{\delta_e}}\delta_e + C_{z_{\delta_e}}\delta_e' \quad (3.82)$$

$$(U - \frac{S\bar{q}c}{2Um}C_{z_{\dot{\alpha}}})\dot{\alpha} = \frac{S\bar{q}}{mU}C_{z_u}u + \frac{S\bar{q}}{m}C_{z_\alpha}\alpha + (U + \frac{S\bar{q}c}{2Um}C_{z_q})q + \frac{S\bar{q}}{m}C_w(sin\Theta)\theta + \frac{S\bar{q}}{m}C_{z_{\delta_e}}\delta_e + \frac{S\bar{q}}{m}C_{z_{\delta_e}}\delta_e' \quad (3.83)$$

Now define in non-dimensional terms:

$$[U - Z_{\dot{\alpha}}]\dot{\alpha} = Z_u u + Z_\alpha\alpha + [U + Z_q]q - g(sin\Theta)\theta + Z_{\delta_e}\delta_e + Z_{\delta_{\dot{e}}}\delta_e' \quad (3.84)$$

$$\dot{\alpha} = \frac{Z_u}{[U - Z_{\dot{\alpha}}]}u + \frac{Z_\alpha}{[U - Z_{\dot{\alpha}}]}\alpha + \frac{[U + Z_q]}{[U - Z_{\dot{\alpha}}]}q - \frac{g(sin\Theta)\theta}{[U - Z_{\dot{\alpha}}]} + \frac{Z_{\delta_e}}{[U - Z_{\dot{\alpha}}]}\delta_e + \frac{Z_{\delta_{\dot{e}}}}{[U - Z_{\dot{\alpha}}]}\delta_e' \quad (3.85)$$

Substitute Eq. (3.85) into Eq. (3.80) to obtain the $\dot{q}$ state-space equation:

$$\dot{q} = [M_u + \frac{M_{\dot{\alpha}} Z_u}{U - Z_{\dot{\alpha}}}]u + [M_\alpha + \frac{M_{\dot{\alpha}} Z_\alpha}{U - Z_{\dot{\alpha}}}]\alpha + [M_q + \frac{M_{\dot{\alpha}} Z_q}{U - Z_{\dot{\alpha}}}]q - \frac{M_{\dot{\alpha}} g(sin\Theta)\theta}{U - Z_{\dot{\alpha}}} + [M_{\delta_e} + \frac{M_{\dot{\alpha}} Z_{\delta_e}}{U - Z_{\dot{\alpha}}}]\delta_e + [M_{\delta_e} + \frac{M_{\dot{\alpha}} Z_{\delta_e}}{U - Z_{\dot{\alpha}}}]\delta_e' \tag{3.86}$$

By extracting the terms in Eqs. (3.85) and (3.86) related to δ_e', the contributions of elevator damage to a longitudinal disturbance can be written in matrix form.

$$\begin{bmatrix} \dot{u}_d \\ \dot{\alpha}_d \\ \dot{q}_d \\ \dot{\theta}_d \end{bmatrix} = \mathbf{A}_F \begin{bmatrix} u_d \\ \alpha_d \\ q_d \\ \theta_d \end{bmatrix} + \begin{bmatrix} 0 \\ \frac{Z_{\delta_e}}{U - Z_{\dot{\alpha}}} \\ M_{\delta_e} + \frac{M_{\dot{\alpha}} Z_{\delta_e}}{U - Z_{\dot{\alpha}}} \\ 0 \end{bmatrix} \delta_e' \tag{3.87}$$

Substituting Eq. (3.75) into the above yields Γ_{lng}:

$$\begin{bmatrix} \dot{u}_d \\ \dot{\alpha}_d \\ \dot{q}_d \\ \dot{\theta}_d \end{bmatrix} = \mathbf{A}_F \begin{bmatrix} u_d \\ \alpha_d \\ q_d \\ \theta_d \end{bmatrix} + \frac{(1 - \zeta_e)}{\zeta_e} \begin{bmatrix} 0 \\ \frac{Z_{\delta_e}}{U - Z_{\dot{\alpha}}} \\ M_{\delta_e} + \frac{M_{\dot{\alpha}} Z_{\delta_e}}{U - Z_{\dot{\alpha}}} \\ 0 \end{bmatrix} \delta_{trim} \tag{3.88}$$

where

$$\Gamma_{lng} = \frac{(1 - \zeta_e)}{\zeta_e} \begin{bmatrix} 0 \\ \frac{Z_{\delta_e}}{U - Z_{\dot{\alpha}}} \\ M_{\delta_e} + \frac{M_{\dot{\alpha}} Z_{\delta_e}}{U - Z_{\dot{\alpha}}} \\ 0 \end{bmatrix} \tag{3.89}$$

For simulation purposes, the maximum expected value of elevator trim is used as δ_{trim}. This derivation reveals that the effect of lost trim moments can be modeled as a disturbance in the longitudinal channel. The disturbance is proportional to the unfailed trim setting and is a function of ζ_e.

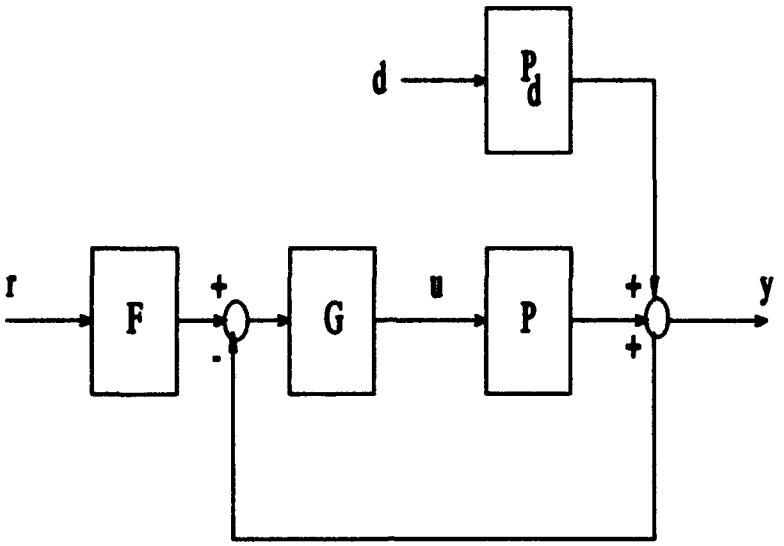

Figure 3.2 MIMO QFT CAD Package Block Diagram

3.3.3 Plant and Disturbance Matrices. Figure (3.2) shows the general block diagram of the model used by the MIMO QFT CAD Package. The derived failure models need to be described in terms of the plant matrix $P(s)$ and the disturbance plant matrix $P_d(s)$.

The failure models have been derived in the form:

$$\dot{\mathbf{x}}(t) = \mathbf{A}(t)\mathbf{x}(t) + \mathbf{B}(t)\mathbf{u}(t) \tag{3.90}$$

$$\mathbf{y}(t) = \mathbf{C}\mathbf{x}(t) \tag{3.91}$$

Placing these equations into Laplace domain yields:

$$s\mathbf{x}(s) = \mathbf{A}(s)\mathbf{x}(s) + \mathbf{B}(s)\mathbf{u}(s) \tag{3.92}$$

$$\mathbf{y}(s) = \mathbf{C}\mathbf{x}(s) \tag{3.93}$$

The states and outputs are therefore solved as:

$$\mathbf{x}(s) = [s\mathbf{I} - \mathbf{A}]^{-1}\mathbf{B}\mathbf{u} + [s\mathbf{I} - \mathbf{A}]^{-1}\mathbf{\Gamma}d(s) \tag{3.94}$$

and

$$\begin{aligned} \mathbf{y}(s) &= \mathbf{C}[s\mathbf{I} - \mathbf{A}]^{-1}\mathbf{B}\mathbf{u} + \mathbf{C}[s\mathbf{I} - \mathbf{A}]^{-1}\mathbf{\Gamma}d(s) \\ &= \mathbf{P}(s)\mathbf{u}(s) + \mathbf{P}_d(s)d(s) \end{aligned} \tag{3.95}$$

where

$$\mathbf{P}(s) = \mathbf{C}[s\mathbf{I} - \mathbf{A}]^{-1}\mathbf{B} \tag{3.96}$$

$$\mathbf{P}_d(s) = \mathbf{C}[s\mathbf{I} - \mathbf{A}]^{-1}\mathbf{\Gamma} \tag{3.97}$$

Equation (3.95) is in the form represented by the system block diagram in Fig. (3.2). Thus the lateral system matrices are:

$$\mathbf{P}(s) = \mathbf{C}[s\mathbf{I} - \mathbf{A}_F]^{-1}\mathbf{B}_F \tag{3.98}$$

$$\mathbf{P}_d(s) = \mathbf{C}[s\mathbf{I} - \mathbf{A}_F]^{-1}\mathbf{\Gamma}_{lat} \tag{3.99}$$

where

$$d_{lat}(s) = \delta_e(s) \tag{3.100}$$

and

$$\Gamma_{lat} = \begin{bmatrix} 0 \\ \frac{(1-\zeta_a)L_{\delta_a UP}}{6\Lambda} \\ 0 \\ \frac{\kappa_n(1-\zeta_a)L_{\delta_a UP}}{6\Lambda} \end{bmatrix} \tag{3.101}$$

The longitudinal system matrices are:

$$\mathbf{P}(s) = \mathbf{C}[s\mathbf{I} - \mathbf{A}_F]^{-1}\mathbf{B}_F \tag{3.102}$$

$$\mathbf{P}_d(s) = \mathbf{C}[s\mathbf{I} - \mathbf{A}_F]^{-1}\Gamma_{lng} \tag{3.103}$$

where

$$d_{lng}(s) = \delta_{trim}(s) \tag{3.104}$$

and

$$\Gamma_{lng} = \frac{(1-\zeta_e)}{\zeta_e} \begin{bmatrix} 0 \\ \frac{Z_{\delta_e}}{U-Z_{\dot{w}}} \\ M_{\delta_e} + \frac{M_{\dot{w}} Z_{\delta_e}}{U-Z_{\dot{w}}} \\ 0 \end{bmatrix} \tag{3.105}$$

IV. Longitudinal MISO Design

This chapter discusses the design of the longitudinal controller. The design steps are outlined in Chapter 1.

4.1 Plant Generation

4.1.1 Flight Conditions. Plants are selected to adequately represent/cover all regions of the Lambda flight envelope and all possible flight conditions. It is desired to include as large a variation in the flight parameters as possible. A large variation better ensures the QFT controller will adequately control the aircraft at any flight condition.

Uncertain flight parameters are chosen with consideration to the actual flight envelope of the Lambda and to the expected conditions during flight. The flight parameters consist of four variables:

- Center of Gravity
- Airspeed
- Altitude
- Weight

For the investigation of control surface failure effects on the longitudinal channel, elevator damage is included as a fifth variable. It is desired to reduce the range on the variables when possible without eliminating a flight condition which the aircraft might encounter. This reduces excess plant variation from the QFT design which facilitates design of the controller.

At air speeds less than 70 knots the Lambda has unstable phugoid poles. The time constant of the unstable phugoid poles is very slow. These plants are eliminated from consideration as the Lambda does not routinely operate at speeds less than 70 knots. Speeds less than 70 knots require use of the flaperons for control. Flaperons are not considered in the design. The maximum speed of the Lambda is 100 knots. To adequately represent upper airspeed limits, a maximum speed of 110 knots is used. Therefore, airspeed is varied from 70 knots to 110 knots.

Lacey uses a weight range of 181 to 215 lbs for his design. This range is somewhat narrowed for this design. The weight of the Lambda without fuel is 194 lbs. With a full tank at take-off, the weight is 208 lbs. To encompass this range and to allow additional components to be loaded on the Lambda, a weight range of 190 to 215 lbs is used.

The high altitude value of the Lambda flight envelope is 10000 ft. Because altitude has large effects on the plant dynamics, a range of 1000 to 10000 ft is considered. It is assumed that high-dynamic maneuvers are not performed below 1000 ft.

Finally, the same center of gravity range as used by Lacey is chosen for the design. This allows for c.g. variation due to fuel consumption during flight. The chosen range is 45.83" to 47.74" measured from the aircraft nose.

Because the extent of the effect of elevator failure on aircraft dynamics is not known, the minimum ζ_e is chosen to be 0.75. This corresponds to half of one entire elevator being lost. This is a substantial failure. If design efforts show that a QFT design cannot be accomplished for this level of a failure, ζ_e will be altered to reflect less damage.

Each flight parameter is taken at its extreme maximum and minimum values. With five conditions being varied, 32 flight conditions are analyzed. The number of plants actually used in

the CAD package is reduced, however, for computational ease. This is discussed in further detail in Section 4.4. The initial 32 flight conditions are presented in Appendix B.

4.1.2 Short-Period Approximation. To reduce computations and increase their numerical accuracy, the short-period approximation is considered. Slow aircraft dynamics are considered negligible. With a pilot in the loop, pilot corrections are anticipated that will negate any slow (phugoid) dynamics. Therefore, if the short-period approximation varies from the full longitudinal dynamics only at sufficiently slow frequencies, the short-period approximation can be considered a valid approximation. Figure 4.1 shows that the short-period approximation duplicates the full equations above $w = 1\frac{rad}{sec}$. Frequencies below $1\frac{rad}{sec}$ are considered slow dynamics. A numerical rule

Figure 4.1 Frequency Response of Complete Longitudinal Eqs. and Short-Period Approximations

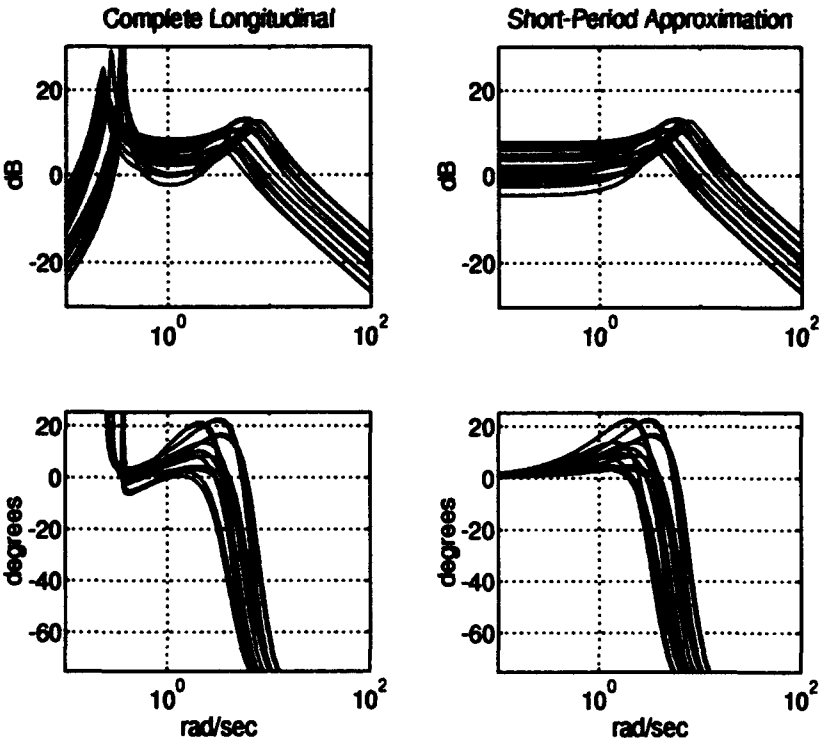

of thumb for use of the short-period approximation is that $\omega_{n_{sp}} > 5\omega_{n_{phugoid}}$. This relation holds true for all 32 flight conditions. Hence, use of the short-period approximation is considered valid from a theoretical point of view.

Final verification of the validity of the short-period assumption is obtained when simulations are performed. Simulations are performed with the full model of aircraft dynamics. Any spillover of the phugoid into the short-period, e.g. due to loop closure, will be seen there.

Appendix C lists the short-period approximation transfer functions of the plants actually used in the CAD package. See Section 4.4 for more detail on the selection of these plants.

4.2 Design Technique

The effective plant model used in the QFT design includes not only aircraft dynamics, but also actuator and sensor dynamics. Actuator models are those given in Eq. (2.8) through Eq. (2.10). Swift did not account for sensor dynamics in his Lambda model. Sensor dynamics are therefore included in the state-space produced by his model.

Several methods exist for the design of a digital controller. In the first method, design can be performed directly in the z-plane. This method is not frequently used due to numerical accuracy problems which arise in the mapping of the s-plane to the z-plane via the transformation $z = e^{sT}$ where T is the sampling period. Another method [9] is to transform the z-plane plant matrix into the w'-plane via the transformation $z = \frac{Tw'+2}{-Tw'+2}$. Lacey's Lambda design was performed in the w'-plane. Problems arose with the gain introduced by the w' method. Therefore, the Pseudo-Continuous Time (PCT) method is utilized for this design, [9].

Implementation of the PCT method requires the dominant poles and zeros of the plant to lie "sufficiently close" to the origin. For a pole located at $\sigma_{dom} + j\omega_{dom}$, sufficiently close is defined as [9]:

$$|\sigma_{dom}| < \frac{0.1}{T} \tag{4.1}$$

$$|\omega_{dom}| < \frac{0.6114}{T} \tag{4.2}$$

For a sampling rate of $50Hz$, the sampling period T is $T = \frac{1}{f_s} = \frac{1}{50} = 0.02sec$. Therefore, to apply the PCT approach:

$$|\sigma_{dom}| < 5 \tag{4.3}$$

$$|\omega_{dom}| < 30.57 \tag{4.4}$$

This requirement is satisfied by the full equations for all longitudinal plants. Note that actuator dynamics do not lie within this region. The PCT approximation is valid since actuator dynamics are not dominant.

The PCT method allows the zero-order hold effects at the input to the plant to be modeled using the first-order Padé approximation. The zero-order hold is modeled exactly in the s-plane as [9]:

$$G_{zoh}(s) = \frac{1 - e^{-sT}}{s} \tag{4.5}$$

The first-order Padé approximation models G_{zoh} linearly as:

$$G_{zoh}(s) \approx \frac{2T}{Ts + 2} \tag{4.6}$$

This approximation is valid for

$$\omega_c < \frac{\omega_s}{10} \tag{4.7}$$

where ω_c is the plant cutoff frequency and ω_s is the sampling frequency which in our case, corresponds to $50Hz$ and is $w_s = 100\pi = 314\frac{rad}{sec}$. Thus, from Eq. (4.7) $\omega_c = 31.416\frac{rad}{sec}$. Figure 4.2 shows the plant frequency response with actuator dynamics included. It is seen that the cutoff frequency is approximately $w = 15\frac{rad}{sec}$. Thus, Eq. (4.7) is satisfied.

Figure 4.2 Longitudinal Plant and Actuator Dynamics

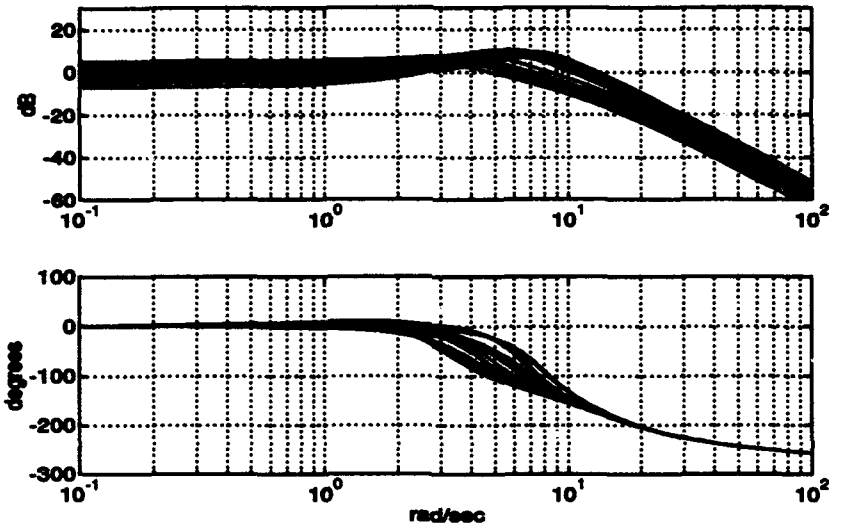

Sampler attenuation of $\frac{1}{T}$ must also be included with the PCT model. The linear nature of the PCT approximation allows the sampling effects to be included with the zero-order hold. Therefore, the PCT approximation $G_A(s)$ is written as:

$$G_A(s) = \frac{1}{T} G_{zoh}(s) \tag{4.8}$$

Therefore combining Eq.(4.6) and Eq. (4.8) with a sampling time of T=0.02 seconds yields:

$$G_A(s) = \frac{100}{s + 100} \tag{4.9}$$

The PCT implementation of the Lambda longitudinal channel is shown in Figure 4.3.

Figure 4.3 Longitudinal PCT Implementation

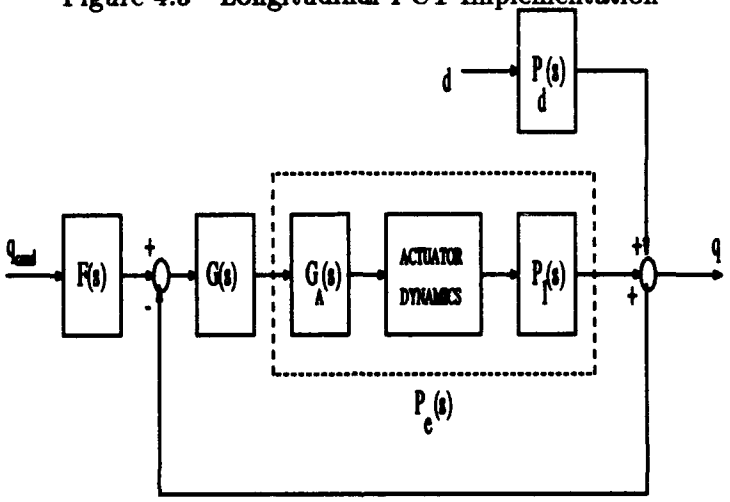

4.3 Loaded and Effective Plants

The equations defining the effect of control surface failures on Lambda dynamics are derived in Chapter 3. These equations are implemented in the modified Lambda model macro. Once implemented, the altered macro generates **A** and **B** matrices for both the longitudinal and lateral channels. A *Matlab* macro then converts the **A** and **B** matrices for each plant into a data file compatible with *Mathematica*. This is required because the MIMO QFT CAD Package operates from a *Mathematica* platform. Once loaded into *Mathematica* and the MIMO CAD Package, the state-space representations are transformed to transfer functions relating output(s) to input(s). QFT design is performed with the resulting transfer functions.

Two sets of **A** and **B** matrices are generated by Swift's amended macro. One set defines the bare aircraft dynamics, $\mathbf{P}_l(s)$. Matrices for the disturbance dynamics $\mathbf{P}_d(s)$ are also created. As shown in Chapter III, the **A** matrix for $\mathbf{P}_l(s)$ and $\mathbf{P}_d(s)$ is the same for the longitudinal design. However, **B** matrices differ by a factor of $\frac{1-\zeta_a}{\zeta_e}$.

The longitudinal design is a MISO design. For the tracking case, there is one input q_{cmd} and one output q. $P_l(s)$ therefore consists of a 1 x 1 matrix of transfer functions. For the disturbance rejection case, there is one input d_{trim} and one output q. Similarly, $P_d(s)$ is also a 1 x 1 matrix of transfer functions. These transfer functions are listed in Appendix C. Henceforth, both $P_l(s)$ and $P_d(s)$ for the longitudinal channel are denoted as scalar quantities. Figure 4.4 shows the frequency response of $P_l(s)$ and $P_d(s)$ for all plant cases used in the QFT design.

Figure 4.4 Frequency Response of Longitudinal $P_l(s)$ and $P_d(s)$

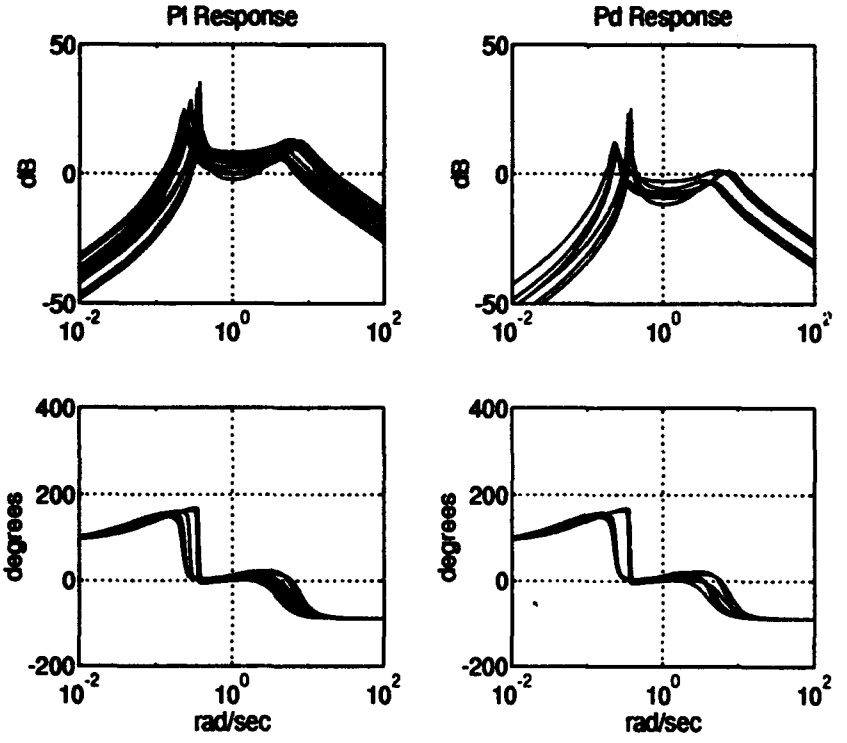

Controller synthesis with the QFT technique takes into account not only aircraft plant dynamics, but also actuator and sensor dynamics. Zero-order hold, actuator and plant dynamics are combined into an effective plant transfer function P_e. Figure 4.3 shows the relation of P_e to the QFT MISO model. Figure 4.5 shows the frequency response of the P_e used in the design (short-period P_e). Appendix C lists the effective short-period longitudinal plants.

Figure 4.5 Frequency Response of Longitudinal P_e (short-period)

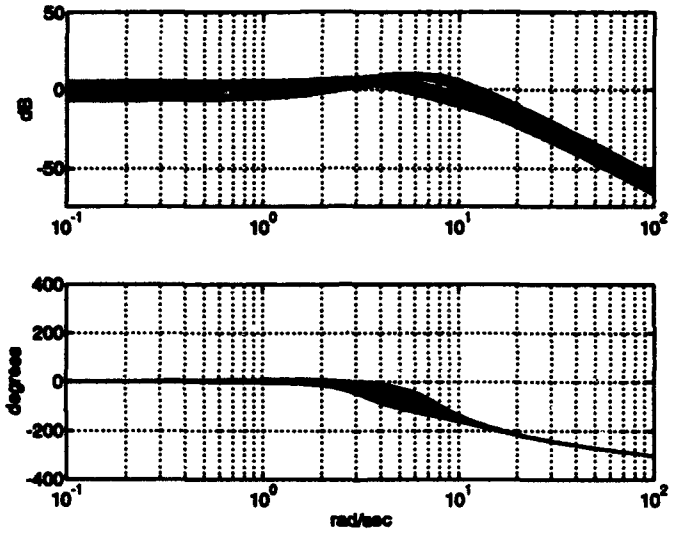

4.4 Plant Templates

Plant templates are generated from the effective plants $P_e(s)$. A number of frequencies must be chosen to use for template generation. Templates below $w = 1\frac{rad}{sec}$ are not used. Plant data below this frequency is not valid since the short-period approximation is used. The upper and lower tracking bounds for a m.p. system are shown in Fig. 4.6 for the longitudinal tracking specification given in Table 1.1. The desired tracking response bandwidth w_{h_R} is defined as the frequency at which the $-12dB$ line intersects the upper tracking bound [8]. Figure 4.6 shows the desired tracking

response is negligible above $w_{h_R} = 20\frac{rad}{sec}$. Therefore, templates for frequencies above $w = 20\frac{rad}{sec}$ are not critical in the design for tracking and disturbance purposes. High frequencies however, still must be considered for stability. One high frequency template at $w = 50\frac{rad}{sec}$ is used to shape the high frequency U-contour. In between $w = 1$ and $w = 20$, template frequencies are chosen on the basis of plant variation. Where plants vary significantly, frequencies are chosen closer together. For the longitudinal design, the frequencies $w = 1, 2.5, 3.25, 4, 6, 8, 10, 20$ and 50 are used.

Figure 4.6 Longitudinal Closed-Loop Tracking Bounds

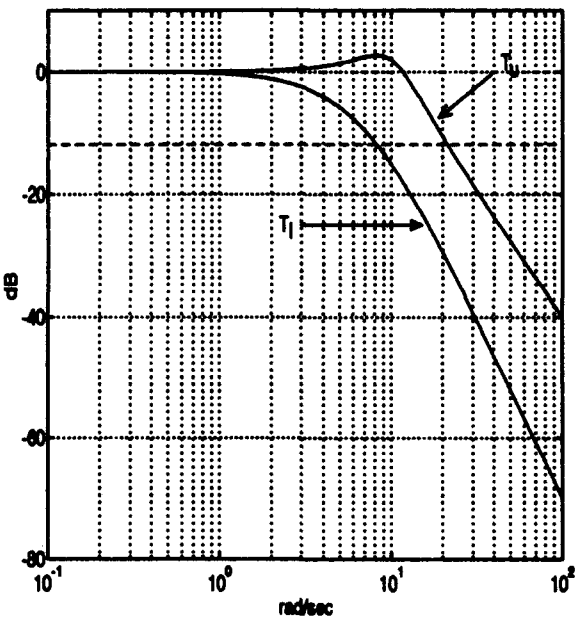

Templates are generated by determining the magnitude and phase of the response for each effective plant at a given frequency. The template is defined by plants with the outermost magnitude and phase values. Lines drawn between these plants define the template boundaries. Figure 4.7 shows the longitudinal templates generated by the MIMO QFT CAD Package.

To reduce package computations, plants which do not define a boundary at any of the chosen frequencies are discarded. This process reduces the number of plants to 15.

Figure 4.7 Longitudinal Templates

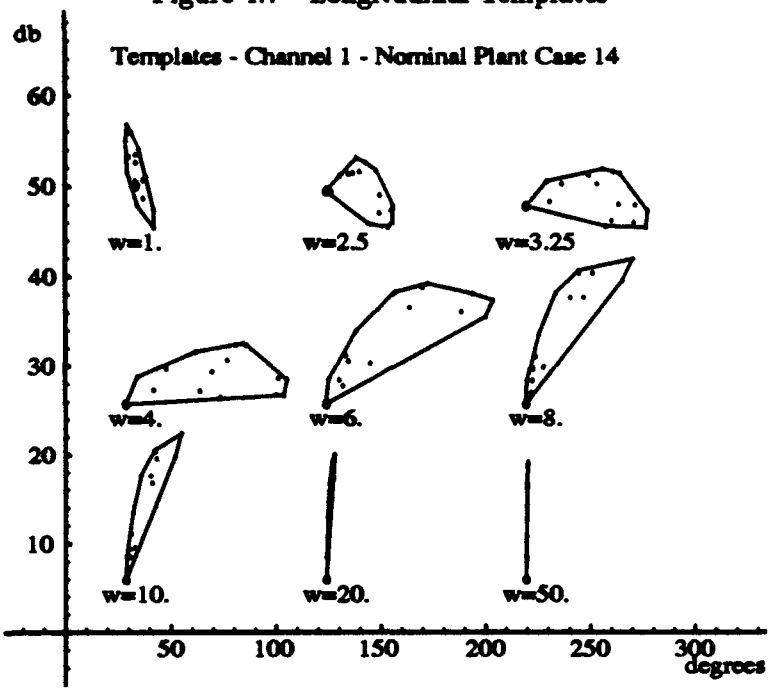

Several flight conditions not among the initial 32 are then included in templates to see if the template boundaries are expanded. One iteration of this process is described. It is seen that little phase variation between plants exists in the high and low frequency templates. For this reason, an intermediate frequency template, $w = 6$, is analyzed. Figure 4.8 shows that plants 2,3,7,8,5,14 and 11 lie consecutively on the boundary. Segments between each of these plants comprise the boundary. Seven boundary segments exist for this template.

Plants 5 and 8 comprise a segment. The contribution of plant 4 to that boundary is considered negligible. The only flight condition which varies between plants 5 and 8 is speed. Adding another plant with the same flight conditions, but with speed chosen half-way between that of plants 5 and 8, yields plant 16 which expands the original template boundary. Figure 4.9 shows the new template with plant 16 added. Addition of this plant results in a more curvi-linear boundary. Similar template expansion occurs for several other frequency templates.

Figure 4.8 Longitudinal Template $w = 6$

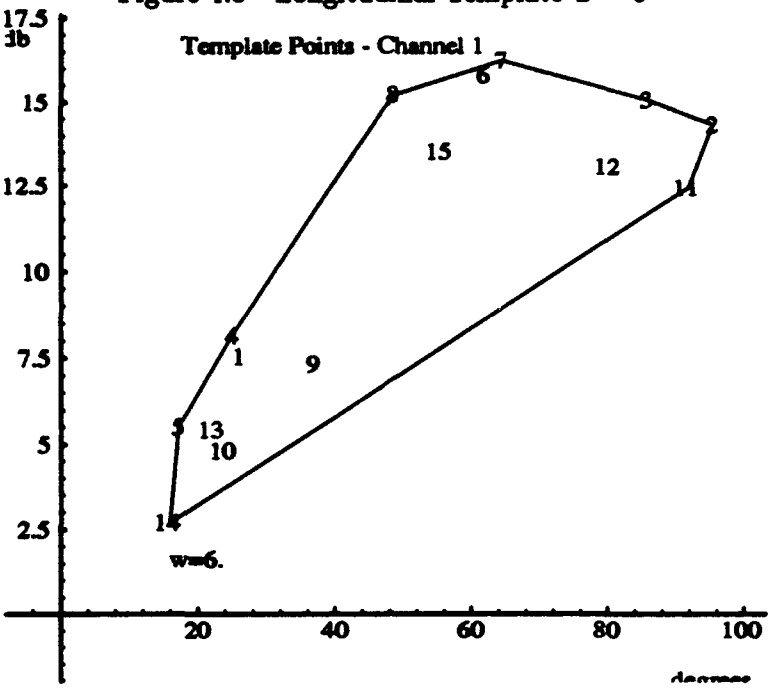

Figure 4.9 Modified Longitudinal Template $w = 6$

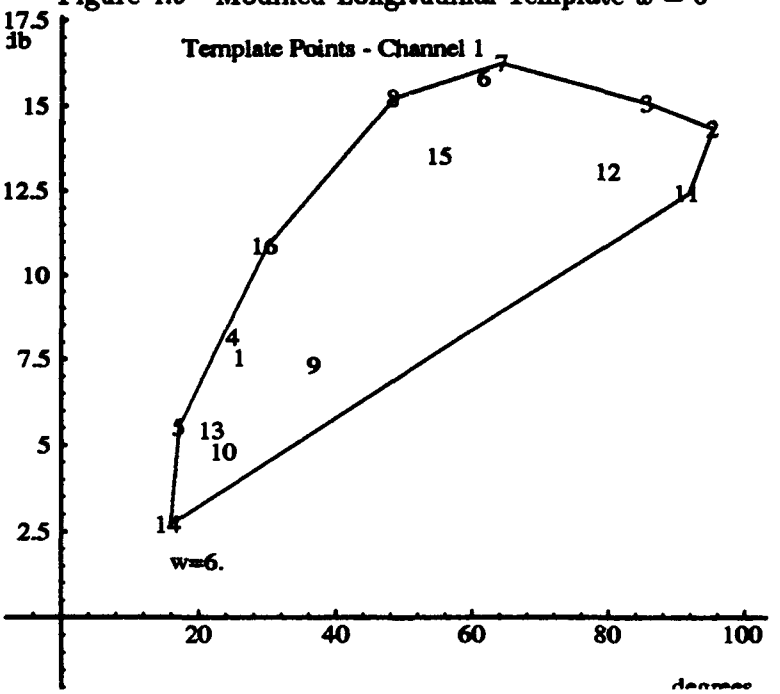

Similar analysis for the other boundary segments found plants which lie inside the existing boundaries. Generally, the templates assume a "banana" shape. The lower boundary (segment 11-14) of the template thus creates some overdesign in the system.

The 16 plants used in the design are listed in Table 4.1. The corresponding short-period transfer functions are the ones listed in Appendix C.

Table 4.1 Sixteen Final Longitudinal Flight Conditions

Plant#	*cg* (*in*)	*Speed* (*ft/sec*)	Q_∞ (lbs/ft^2)	*Weight* (*lbs*)	ζ_e
1	45.83	118.23	12.27	215	1
2	45.83	185.79	39.83	215	1
3	45.83	185.79	30.31	215	1
4	47.75	118.23	16.13	190	1
5	47.75	118.23	12.27	215	1
6	45.83	185.79	39.83	190	1
7	45.83	185.79	39.83	215	1
8	45.83	185.79	30.31	215	1
9	45.83	118.23	16.13	190	.75
10	45.83	118.23	12.27	215	.75
11	45.83	185.79	39.83	215	.75
12	45.83	185.79	30.31	215	.75
13	47.75	118.23	16.13	190	.75
14	47.75	118.23	12.27	190	.75
15	47.75	185.79	39.83	190	.75
16	47.75	152.00	20.29	190	1

The maximum magnitude differential in a template is 16.6 dB at $w = 10$. The maximum phase difference is 80 degrees at $w = 6$. Investigation of the location of plants within each template reveals that speed and altitude cause the largest plant variation with a constant percentage of elevator damage. Elevator damage causes a loss of magnitude and a slight increase in phase lag.

The QFT procedure requires the selection of a nominal plant. This plant is the one actually used during the controller synthesis (loop-shaping) process. Tracking and disturbance bounds on

the Nichol's Chart are created from the nominal plant. The nominal plant is usually chosen as the plant with the largest phase lag and smallest magnitude for the most frequencies. Plant 14 of Table 4.1 is chosen as the nominal. It is seen that Plant 14 is at the lowest speed, highest altitude and maximum failure. It is expected that control efforts will be most difficult under these conditions. The nominal plant transfer function is:

$$\frac{q(s)}{\delta_e(s)} = \frac{4.5870(s + 2.1700)}{(s + 1.3559 \pm j2.9567)} \tag{4.10}$$

4.5 Tracking and Disturbance Bounds

Figures 4.10 and 4.11 shows the tracking and disturbance bounds generated by the MIMO QFT CAD Package. Tracking bounds are comparable to those generated in a Lambda longitudinal design by Wright Laboratories. Tracking bounds are created from the templates shown in Fig. 4.7. Disturbance bounds are created based on a disturbance rejection limit of 0.2. That is, the maximum system output from a disturbance should not exceed 20% of the disturbance input. Because no specifications for disturbance rejection are given, 0.2 is arbitrarily chosen. If actual responses are unsatisfactory or if a 0.2 bound cannot be met, the bounds can be changed accordingly.

A low system bandwidth is beneficial to feedback design. Large bandwidths increase control effort as well as allow the introduction of sensor noise and structural dynamics. In a digital design, low system bandwidth is especially crucial, as a high bandwidth requires faster sampling rates. It is seen that satisfying disturbance bounds requires an excessively high bandwidth. The advantage of QFT is evident here. To minimize bandwidth, engineering judgement is used to selectively violate bounds. Bounds at frequencies with minimal effect on system response are ignored. More effort is

placed on meeting the low frequency bounds. This is because higher frequencies experience greater attenuation by the plant.

Figure 4.10 Longitudinal Tracking Bounds

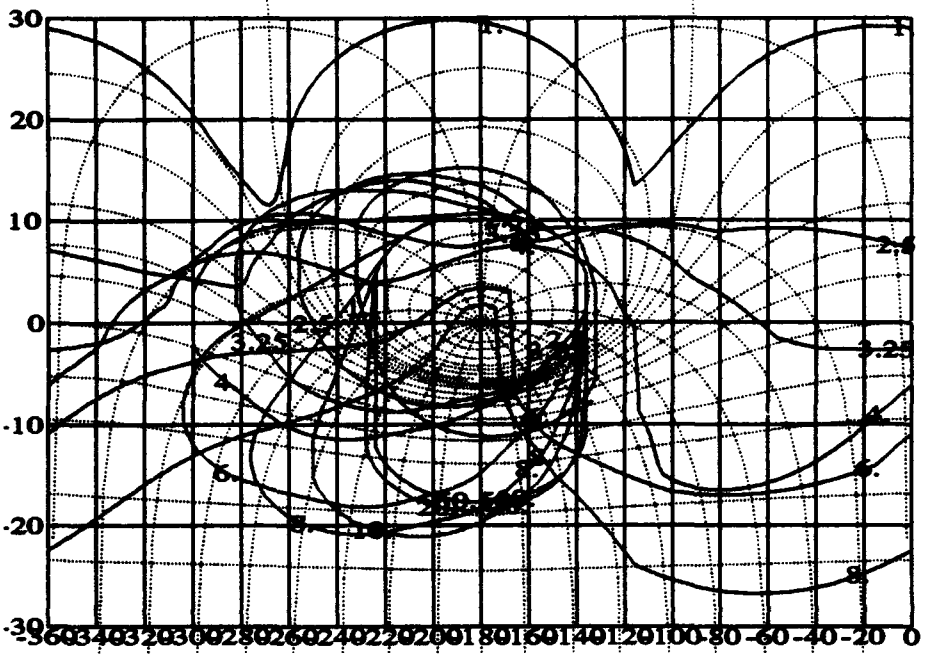

4.6 Compensator $G_{11}(s)$

The longitudinal compensator's transfer function $G_{11}(s)$ is obtained by shaping the nominal loop on the Nichol's Chart so that all frequencies lie above their corresponding bounds and outside their corresponding stability contour.

Elevator failures increase plant phase lag and decrease plant magnitude. Both factors tend to increase the bandwidth of the open-loop plants. This causes a significant amount of lead and gain to be placed in the controller. Poles of the compensator must therefore be placed far from the origin, so as not to negate the benefits of the zeros which are added. This creates aliasing problems when the controller is implemented digitally. The poles of $G_{11}(s)$ must therefore be "slow" enough

Figure 4.11 Longitudinal Disturbance Bounds

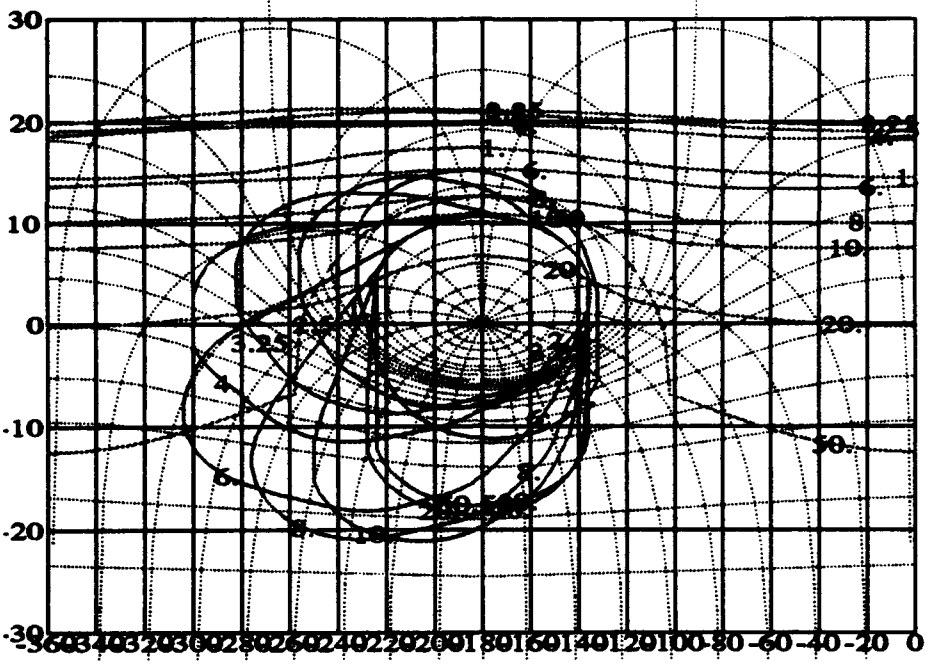

so $G_{11}(z)$ at $50Hz$ emulates $G_{11}(s)$. A rule of thumb to be followed while loop-shaping is to keep the natural frequency of the poles less than $\frac{1}{2}$ the sampling frequency ($\omega_n < \frac{1}{2}\omega_s$). At $50Hz$, therefore, poles should be placed at $s > -150$ as a minimum. This is as non-dominant as the poles can be made when including poles to obtain a proper order compensator.

Problems arise when loop-shaping with compensator poles > -150. The nominal loop transmission tends to violate the U-contour at high frequencies. Anticipating the additional lag of the compensator poles, as the nominal loop is designed, a phase margin of 60° is targeted. Then, when compensator poles are placed, the additional lag of these poles returns the nominal loop closer a 45° phase margin.

Even with the phase margin considerations while loop-shaping, U-contour violations occur at high frequencies. It is decided that some low frequency boundaries are to be violated to complete

the loop shape. Tracking bounds are not as restrictive and they can all be met fairly easily. Disturbance bounds are therefore violated.

Initial efforts at loop-shaping result in a compensator which satisfies all tracking bounds but violates all disturbance bounds except $w = 1$. Simulations revealed excellent tracking response and disturbance rejection. However, analysis of sensor noise effects, (see Sec. 4.10), revealed significant amplification of sensor noise between 5 and $90\frac{rad}{sec}$. This noise amplification should be attenuated to acceptable levels as aircraft structural modes lie within the specified bandwidth. Therefore, a new $G_{11}(s)$ is synthesized.

The requirement for an acceptable $G(s)$ is it must have as low as possible magnitude in the bandwidth of concern. This presents a problem with respect to stability and the need to provide quite a bit of additional phase lead and gain due to failures in this region. Thus it is decided that loop-shaping should be performed to satisfy only the tracking bounds. The first loop-shaping attempt violated disturbance bounds significantly, yet disturbance rejection, upon simulation, was quite good. Ignoring disturbance bounds allows the compensator gain to be lowered considerably, thereby enhancing noise rejection.

Loop-shaping results in the nominal open-loop transmission of Fig. 4.12 and the following s-domain compensator:

$$G_{11}(s) = \frac{13804.6(s+2)(s+3)(s+13.125 \pm j7.26)}{s(s+0.3)(s+130)(s+150)^2} \tag{4.11}$$

Based on the tracking bounds in Fig. 4.12, the initial attempts at prefilter design indicate that the tracking bound at $w = 2\frac{rad}{sec}$ is not satisfied. To meet the tracking bound at $w = 2\frac{rad}{sec}$ requires a significant increase in compensator gain if compensator order is not increased. It is decided that the increase in compensator order is not worth the improvement in tracking. Therefore, the bound at $w = 2$ is left unsatisfied. With this violation, simulation will determine if the design is acceptable.

Figure 4.12 Longitudinal Nominal Loop Transmission

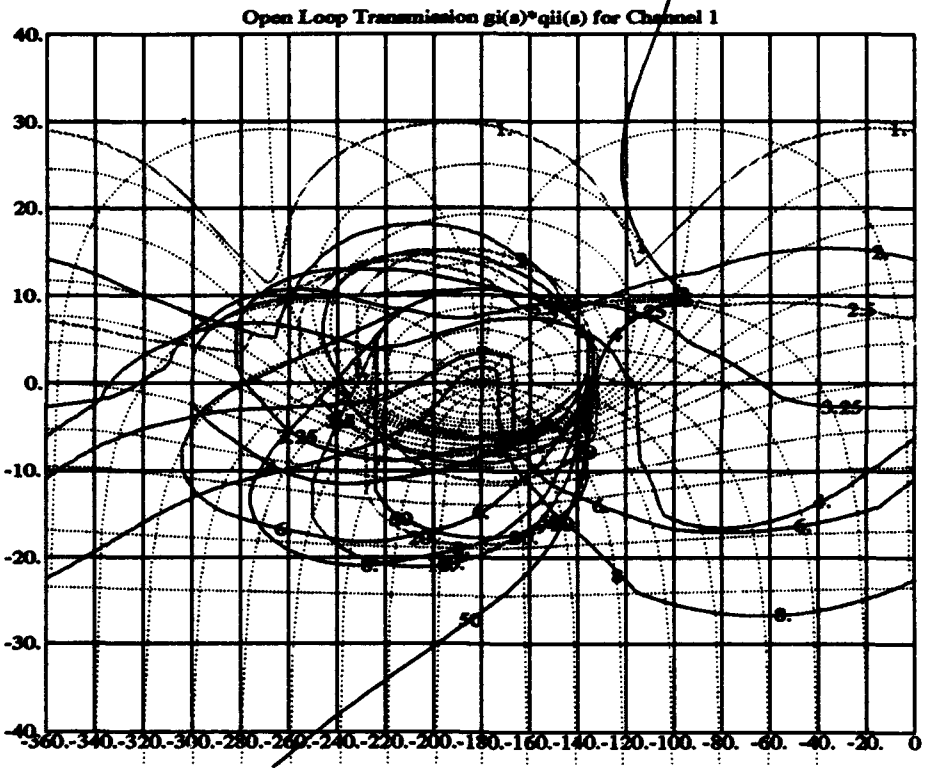

The digital flight control system of the Lambda requires the controller to be implemented discretely. Because $G_{11}(s)$ does not have two more poles than zeros and does involve a zero-order-hold, a direct z-transform cannot be performed [9]. Instead the following bilinear Tustin transformation is used to transform $G_{11}(s)$ to $G_{11}(z)$:

$$s^q = \left[\frac{2(1-z^{-1})}{T(1+z^{-1})}\right]^q \tag{4.12}$$

Applying the Tustin approximation to Eq. (4.11) results in the following discrete controller:

$$G_{11}(z) = \frac{12.25156(z+1)(z-0.96078)(z-0.94175)(z-0.76070 \pm j0.11300)}{(z-1)(z-0.99402)(z+0.2)^2(z+0.13043)} \tag{4.13}$$

The discrete controller must adequately duplicate the continuous compensator for the given sampling rate. The duplication can be determined by analyzing the frequency responses of both $G_{11}(s)$ and $G_{11}(z)$. If the responses are the same up to $\frac{1}{3}\omega_s$ the sampling rate is adequate. For $\omega_s = 314.16\frac{rad}{sec}$, the controller frequency responses must match up to $105\frac{rad}{sec}$. Figure 4.13 shows a good correspondence within the required bandwidth of $0 < \omega < 105\frac{rad}{sec}$.

Figure 4.13 $G_{11}(s)$ and $G_{11}(z)$ Controller Frequency Responses

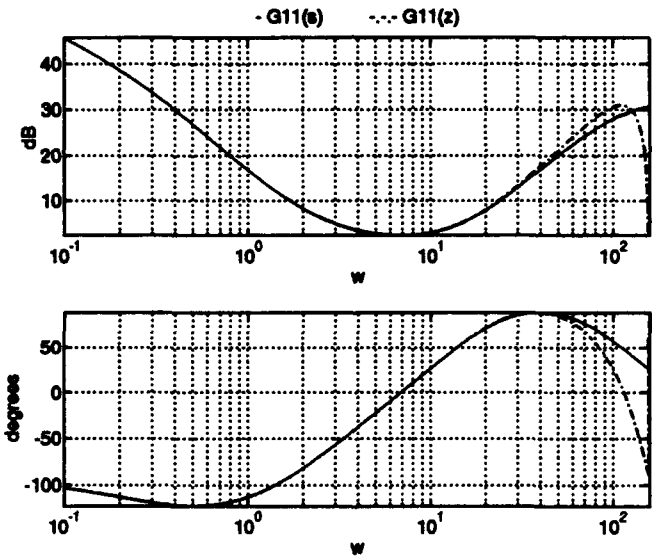

4.7 Prefilter $F_{11}(s)$

The prefilter is obtained by plotting the frequency responses of the closed-loop system on the same magnitude Bode plot as the upper and lower tracking bounds. The prefilter is then adjusted until the frequency responses for all plants lie within these tracking bounds. If violations of the

tracking bounds occur in the loop shaping process, it is likely that the upper and/or the lower tracking bounds will be violated by the closed-loop response for one or more of the plants at that same frequency. If tracking bound violations occur at significantly small magnitudes, the impacts are negligible. The prefilter is chosen as:

$$F_{11}(s) = \frac{0.010942(s+1.9)(s+100)^2}{(s+2.2)(s+6.3)(s+15)} \tag{4.14}$$

The non-dominant zeros at $s = -100$ are placed to prevent $F_{11}(z)$ from having two zeros lie on the unit circle, as would occur if $F_{11}(s)$ is left as a first over third order transfer function and the Tustin approximation applied to obtain $F_{11}(z)$.

Figure 4.14 shows that with the prefilter of Eq. (4.14), the tracking bounds are slightly violated for some plants at approximately $2\frac{rad}{sec}$. This violation is expected due to the violation of the $w = 2$ tracking bound. Once again, the gain required to meet the tracking specifications at these frequencies is not considered worthy of the cost in noise attenuation.

Like $G_{11}(s)$, $F_{11}(s)$ must be transformed to the discrete domain. A Tustin transformation results in:

$$F_{11}(z) = \frac{0.035698(z-0.96271)(z)^2}{(z-0.95695)(z-0.88147)(z-0.73913)} \tag{4.15}$$

Since the $F_{11}(s)$ and $F_{11}(z)$ frequency responses in Fig. 4.15 lie essentially on top of one another within the bandwidth $0 \leq w \leq 105$ then the prefilter of Eq. (4.14) is valid for the given sampling rate.

Figure 4.14 Longitudinal Closed Loop Response

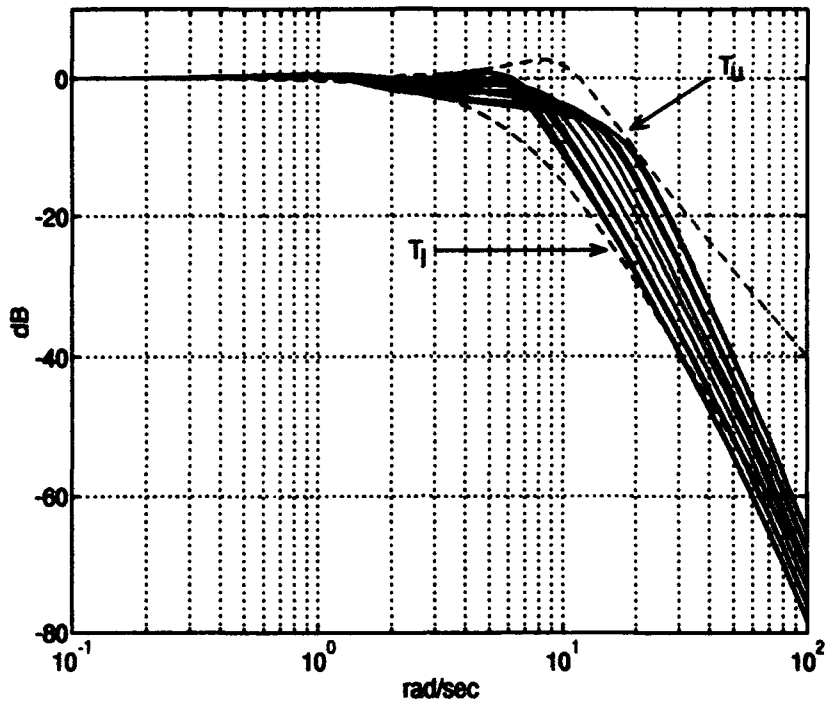

Figure 4.15 $F_{11}(s)$ and $F_{11}(z)$ Pre-Filter Frequency Responses

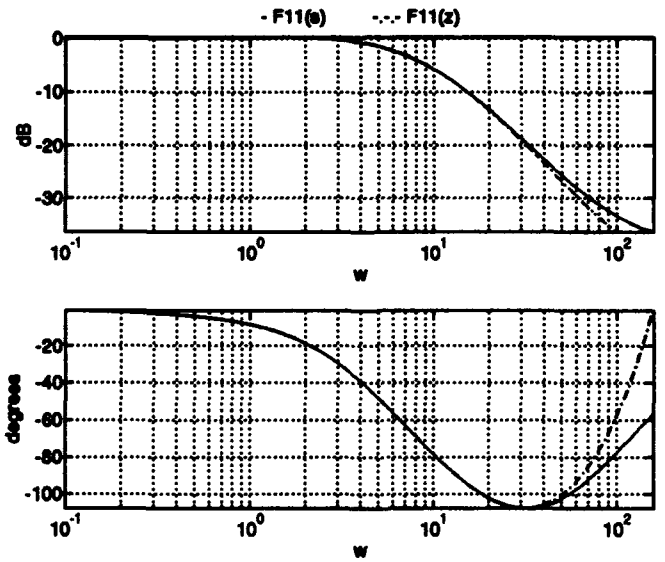

4.8 Validation of the QFT Design

A simulation of the QFT design reveals if any of the design specifications are violated. It has already been shown in Fig. 4.14 that the frequency domain tracking specifications are slightly violated with the designed controller and prefilter. The simulation (Sec. 4.9) will determine if this violation is insignificant. Wright Laboratories also specified a $\gamma = 45°$ phase margin angle. This corresponds to a $3dB$ M_m contour on the Nichol's Chart. Figure 4.16 shows that the γ requirement is satisfied for all plants.

Figure 4.16 Longitudinal Open-Loop Transmissions with $G_{11}(s)$ Included

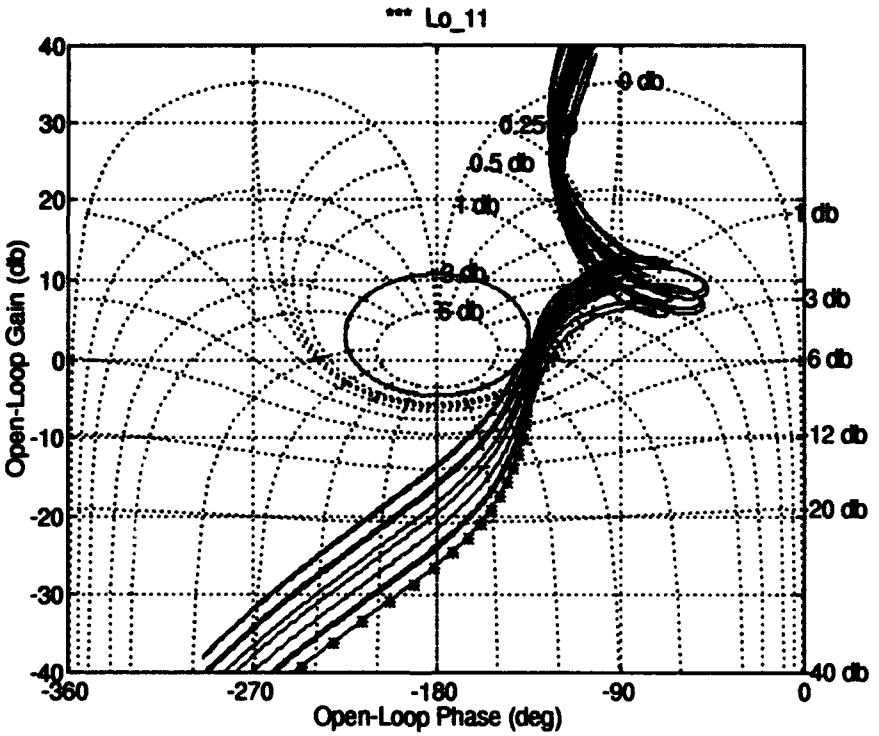

Analysis of the closed-loop disturbance response in Fig. 4.17 indicates that the arbitrarily chosen 0.2 disturbance bound is violated from 2 to $35\frac{rad}{sec}$. The simulations will determine if this

violation is acceptable. The violation is most likely to be unacceptable if the input disturbance signal has a large magnitude at one of the violated frequency components.

Figure 4.17 Longitudinal Closed-Loop Disturbance Response

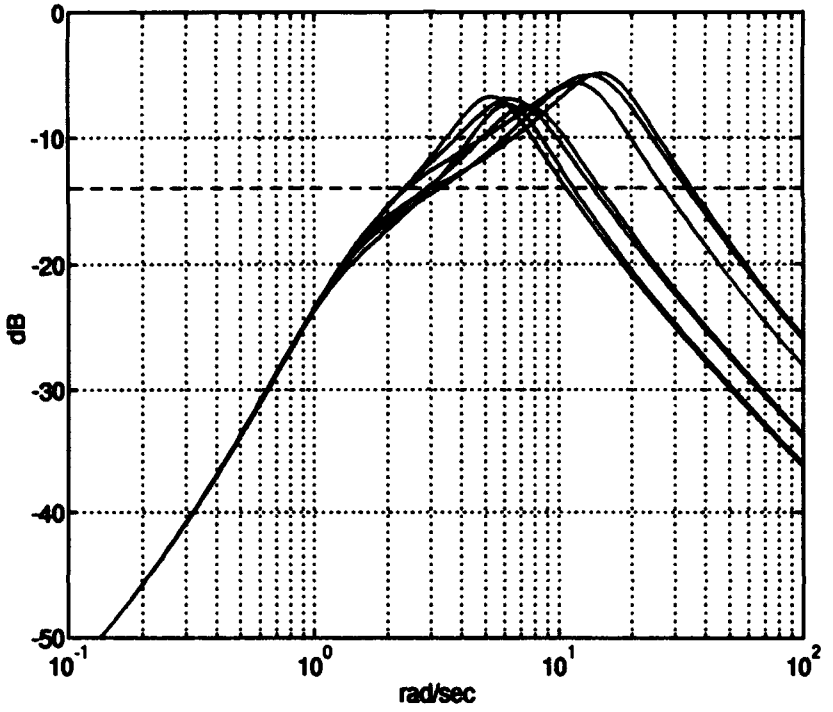

4.9 Simulation

Time domain simulations verify the effectiveness of the designed controller. Simulations are performed in *Simulink* using a linear model. A non-linear actuator element is included in the model. The non-linear element represents the deflection limits of the elevator. *Simulink* allows both discrete and continuous elements to be included in the simulation. Therefore, prefilters and controllers are described in the model with z-domain transfer functions with sampling time equal to 0.02 seconds. Actuators and aircraft dynamics are described with s-domain transfer functions. Figure 4.18 is the block diagram representation of the simulation model.

Figure 4.18 Longitudinal Channel Simulink Model

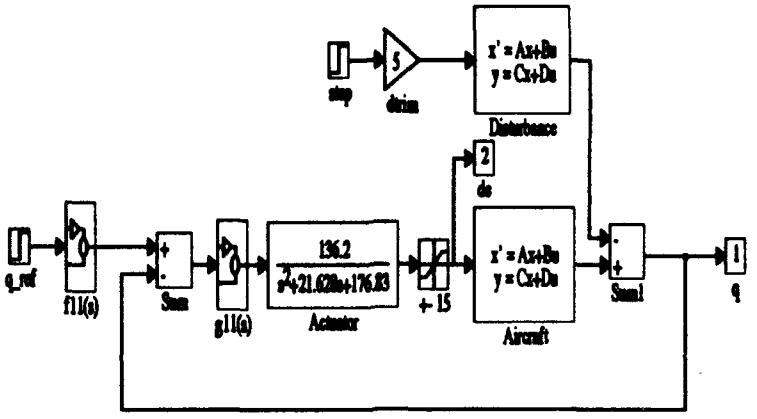

A step input of $q_ref = 1\frac{deg}{sec}$ is applied to the system. Figure 4.19 shows the aircraft response with the designed controller and prefilter in place. The response is seen to reach the desired reference in a reasonable amount of time. Pitch angle increases steadily as expected. The corresponding elevator deflection is well within the limits of the actuator.

The controller is seen to attenuate the pitch motion caused by the loss of elevator and also return the aircraft to trimmed, level flight. The elevator is seen to assume a steady-state value. This elevator setting is a result of the trim moment lost when the elevator damage occurs.

A larger reference input of $10\frac{deg}{sec}$ is applied to the system to analyze possible saturation of the actuators. Figure 4.20 shows the elevator saturating as early as 1.25 seconds for one flight condition. The flight condition which saturates (flight condition #10) is characterized by low speed and high altitude with elevator failure. Minimal control authority is expected here. When the elevator saturates, the pitch rate is not maintained. This is due to the corresponding loss of speed.

When actually performing a pitch maneuver, the pilot must apply more throttle to maintain pitch rate. The response of Fig. 4.20 is considered adequate for the Lambda aircraft.

Figure 4.19 Longitudinal Tracking and Disturbance Responses

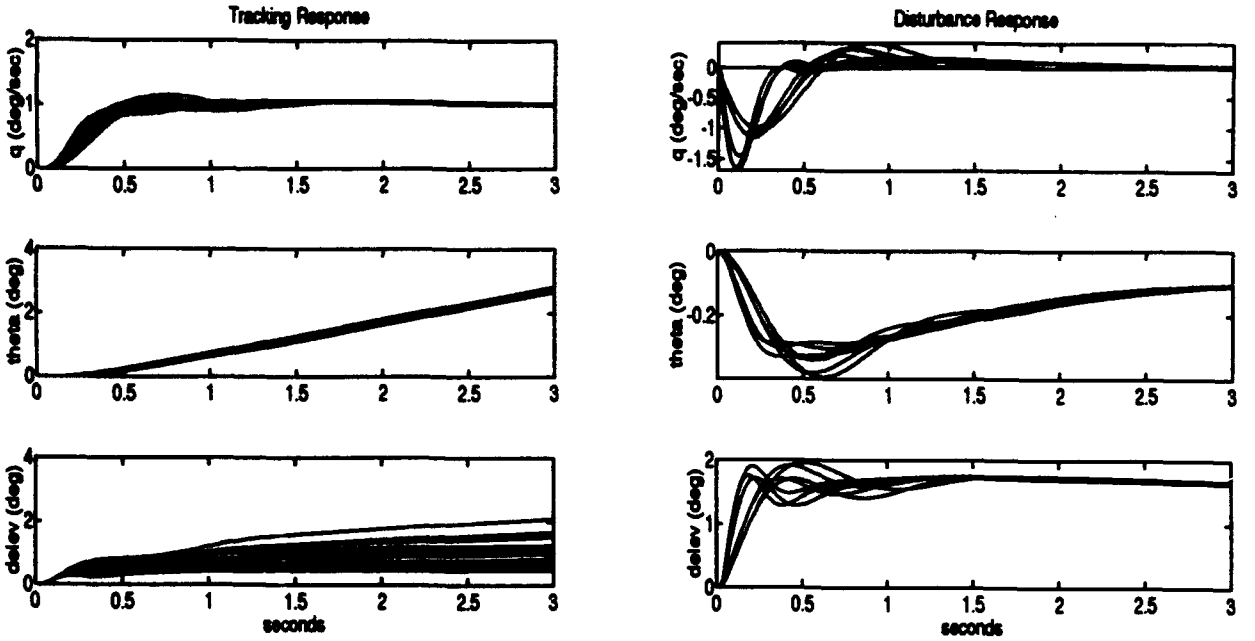

There exists an extent of damage at which no controller can adequately maintain aircraft dynamic response. Obviously, if $\zeta_e = 0$, no capability exists to control the longitudinal dynamics of the aircraft. While the designed controller and prefilter of Eq. (4.13) and Eq. (4.15) generally meet the given specifications for failures up to $\zeta_e = 0.75$, it is desired that the controller still allow some control authority for more drastic surface damage.

When flying at steady cruise conditions, the elevators are set at a small positive deflection to trim the aircraft. As surface area is lost, the elevators deflect more to generate the same trim pitch moment on the tail. There exists a failure level when the damaged elevator saturates before creating the necessary trim moment. When this occurs, the aircraft is statically unstable. If the

Figure 4.20 Longitudinal Tracking Response $10\frac{deg}{sec}$ Reference

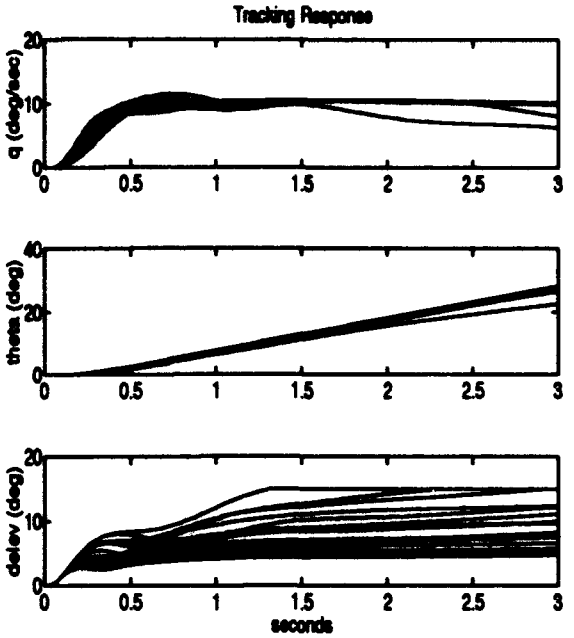

elevator does trim the aircraft but is saturated, no control authority is left in the elevator. It is therefore desirable to maintain some available elevator deflection for dynamic control purposes.

The total elevator deflection after damage is equal to the initial trim setting (δ_{trim}) plus the additional deflection required for damaged trim ($\delta_e^{'}$). To maintain 5° of elevator control authority, the following relation must hold:

$$\delta_{trim} + \delta_e^{'} < 10^{\circ} \tag{4.16}$$

Simulations assume a worst case initial trim setting of 5°. Therefore, the steady-state elevator deflection in response to a longitudinal disturbance should not exceed 5° to satisfy Eq (4.16). Equation (3.75) defines the relation between δ_{trim} and $\delta_e^{'}$. Substituting Eq. (3.75) into Eq. (4.16) yields:

$$\delta_{trim} + \frac{1-\zeta_e}{\zeta_e}\delta_{trim} < 10^{\circ} \tag{4.17}$$

Assuming the worst case initial trim setting of 5°, solving Eq. (4.17) for ζ_e results in:

$$\zeta_e > 0.5 \tag{4.18}$$

Therefore, the elevator cannot experience more than a 50% failure and still guarantee elevator control authority. Figure 4.21 shows a Lambda response for the 16 flight conditions with $\zeta_e = 0.5$.

Figure 4.21 Longitudinal Response $\zeta_e = 0.5$

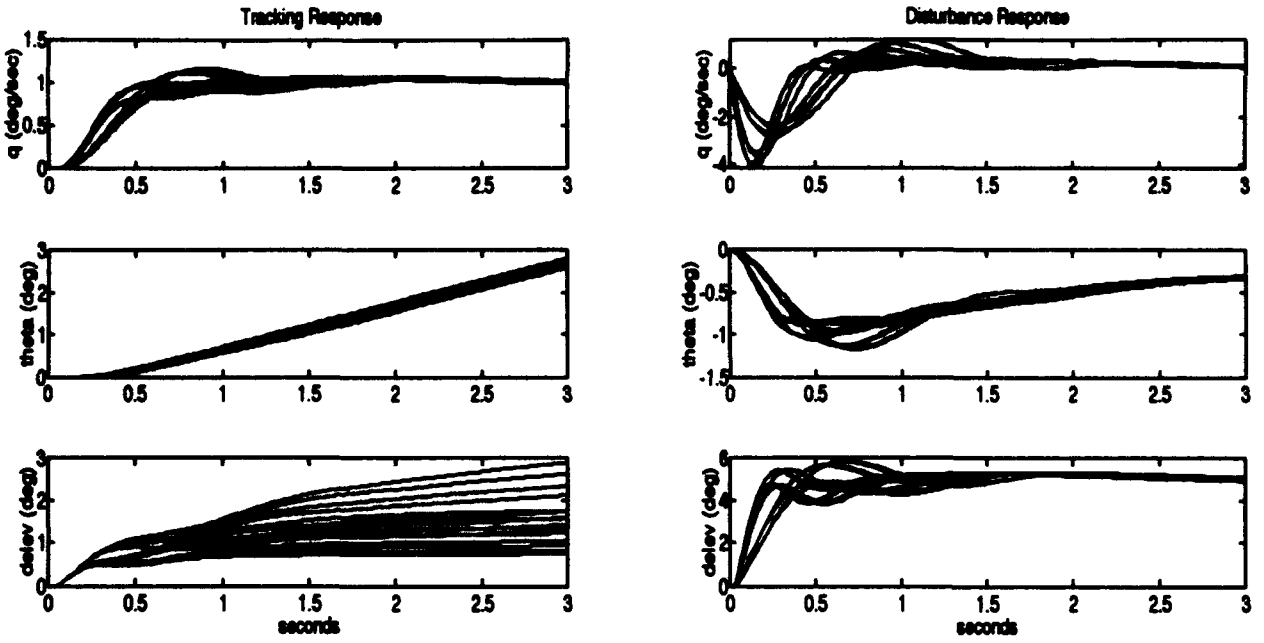

It is seen that the additional trim deflection is equal to 5°. The elevator deflection in response to a $1\frac{deg}{sec}$ pitch rate reference never exceeds 5°. Therefore reasonable longitudinal control is possible with only 50% of available elevator. The rate response though is not as crisp as at 75% available elevator. This is because QFT design was based on 25% elevator failure. Larger magnitude of pitch references saturate the elevator. These simulations are based on an initial worst case trim setting of 5°. This is a conservative estimate.

4.10 Other Concerns

The Lambda has longitudinal structural modes at $28\frac{rad}{sec}$. Excitation of the elevator by a reference input or by sensor noise should avoid exciting these modes. Block diagram models in *Simulink* are used to determine the frequency response of the elevator with respect to both of the cited inputs.

Figure 4.22 shows the equivalent block diagram used for analysis and Fig. 4.23 shows the resulting frequency response of a reference input. It is seen that the system is greatly attenuated above $10\frac{rad}{sec}$. This greatly eliminates the probability of pilot induced oscillations (p.i.o.).

Figure 4.22 Block Diagram of Elevator Response to Reference Input

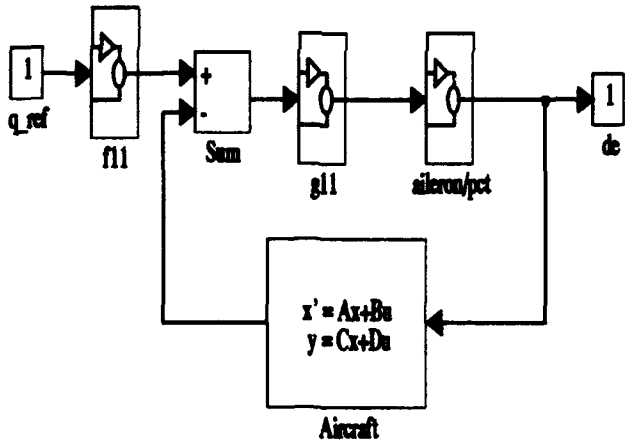

Figure 4.24 shows the equivalent block diagram used for analysis and Fig. 4.25 shows frequency response of an elevator to sensor noise. Noise levels are approximately 7 to $8dB$ lower than in the initial compensator design. While sensor noise is not amplified, the possibility exists that if sensor noise is large enough, structural mode excitation may become significant.

Figure 4.23 Frequency Response of Elevator to a Reference Input

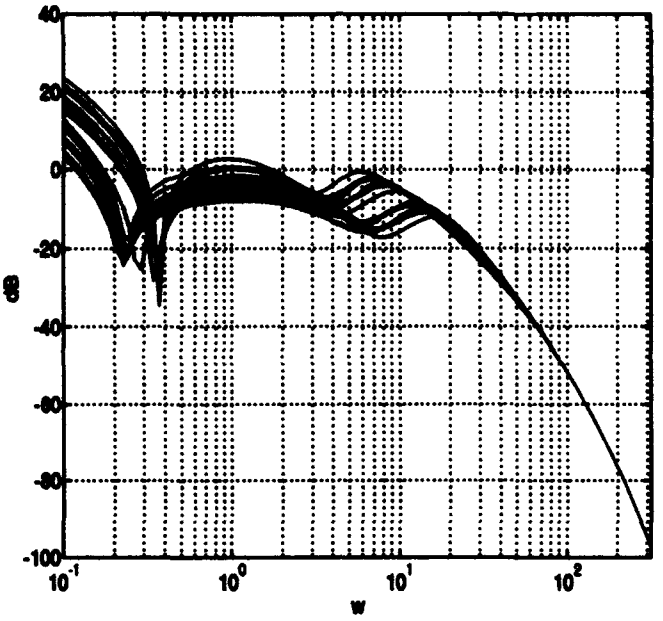

Figure 4.24 Block Diagram of Elevator Response to Sensor Noise

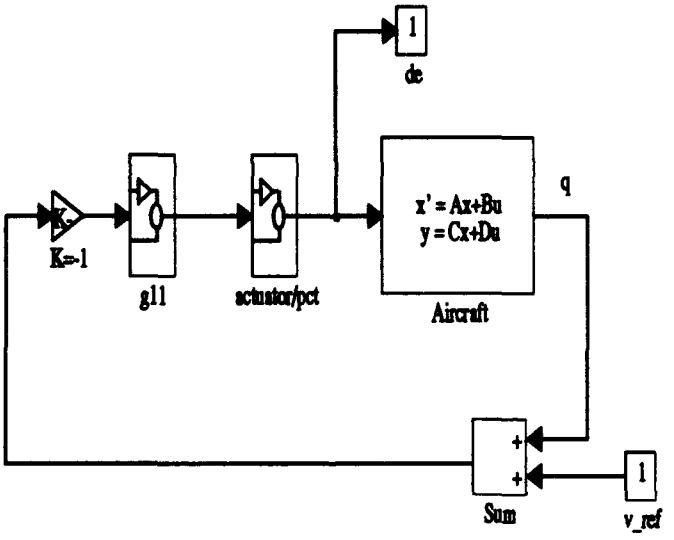

Figure 4.25 Frequency Response of Elevator to Sensor Noise

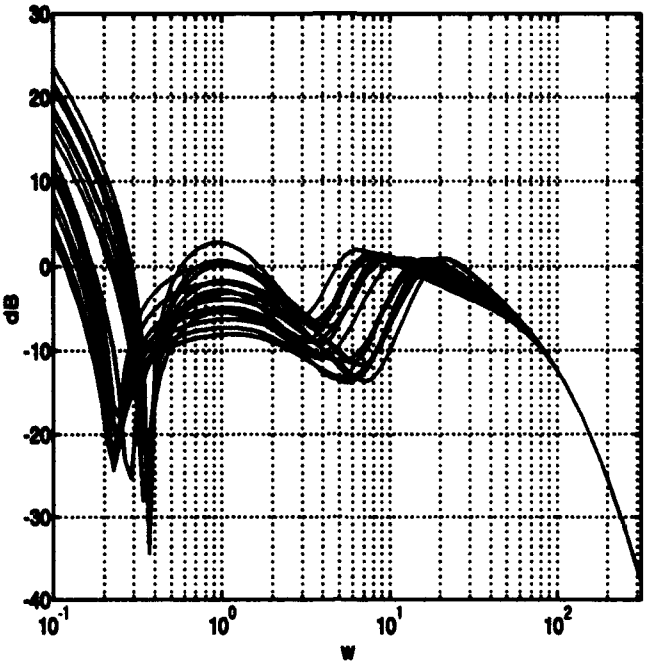

The effect that pitch rate sensor noise has on elevator control can be determined through simulation. Wright Laboratories has developed white Gaussian noise models for all sensors on board the Lambda [10]. The modeled pitch rate sensor noise is added to the *Simulink* model at the sensor feedback loop. Figure 4.26 shows that pitch rate noise has a negligible effect on the aircraft's pitch channel response.

Figure 4.26 Response of the Lambda to Pitch Sensor Noise

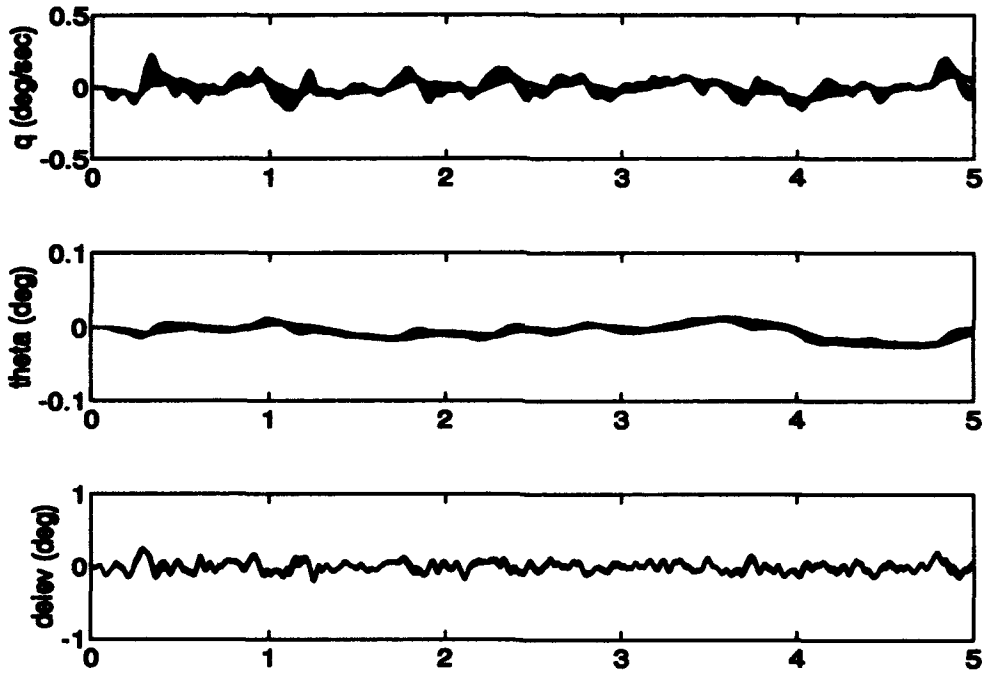

V. *Lateral MIMO Design*

This chapter presents the MIMO lateral controller design. The design of the lateral channel differs slightly from the design of the MISO longitudinal channel. The differences are discussed here. Individual design steps are outlined in Chapter 1.

5.1 Plant Generation

5.1.1 Flight Conditions. Similar to the longitudinal channel, flight conditions used to generate lateral channel plants are selected to adequately represent the entire flight envelope. The same flight variables in the longitudinal channel determine the envelope for the lateral channel; center of gravity, airspeed, altitude and weight. The same range of these variables used in the longitudinal channel is used to generate lateral plants. Elevator failure is still considered in the lateral channel due to the cross-coupling of failures. Failures to the lateral control surfaces, ailerons and rudders, are now considered. This leaves seven different variables to be considered for the lateral channel. Varying all seven between their maximum and minimum values results in 128 permutations of lateral plants. Processing this many permutations during the design process would be computationally intensive. The number of plants is therefore reduced.

Because the lateral channel has no gravity force acting on it, (see Eqs. (3.27) through (3.29)), weight has no effect on lateral dynamics. Inspection of the magnitude and phase response of the lateral transfer functions reveals that the lateral response is negligibly affected by the center of gravity location. These two variables are therefore set to the median value of their expected ranges:

$$c.g. = 45.83" + \frac{47.74" - 45.83"}{2} = 46.79" \tag{5.1}$$

$$weight = 190 + \frac{215lbs - 190lbs}{2} = 202.5lbs \tag{5.2}$$

The number of lateral plants is reduced further by assuming a constant elevator failure of 50% ($\zeta_e = 0.5$). A const value is assumed because the magnitude of elevator failure has no effect on lateral disturbance dynamics. It only effects the magnitude of the disturbance input. Therefore, if disturbances from 50% elevator failure are rejected, failures of less magnitude are also rejected.

The four parameters that are varied for lateral plant generation are:

- Airspeed
- Altitude
- Aileron Failure
- Rudder Failure

which result in sixteen lateral flight conditions. These flight conditions are listed in Appendix B. Like the longitudinal channel, plants are eliminated during template generation. This is discussed further in Section 5.4.

5.1.2 Plant Transfer Function Matrix. Lateral control system design can take place around several different lateral states. Because coordinated flight is desired, roll rate and sideslip angle are the states utilized for design. No approximations are used to generate these transfer functions.

The resulting transfer function matrix utilizing bare aircraft dynamics is:

$$\mathbf{P}_{lat}(s) = \begin{bmatrix} \frac{p(s)}{\delta_a(s)} & \frac{p(s)}{\delta_r(s)} \\ \frac{\beta(s)}{\delta_a(s)} & \frac{\beta(s)}{\delta_r(s)} \end{bmatrix} \tag{5.3}$$

5.2 Design Technique

The PCT method is used for the lateral design. Dominant poles of aircraft plant transfer functions all lie within the region specified by Eq. (4.3) and Eq. (4.4). Figure 5.1 shows the frequency response of lateral plant and actuator dynamics. Cutoff frequencies satisfy the limit of $30\frac{rad}{sec}$ defined by Eq. (4.7). The PCT approximation is therefore valid for the lateral channel.

Figure 5.1 Lateral Plant and Actuator Dynamics

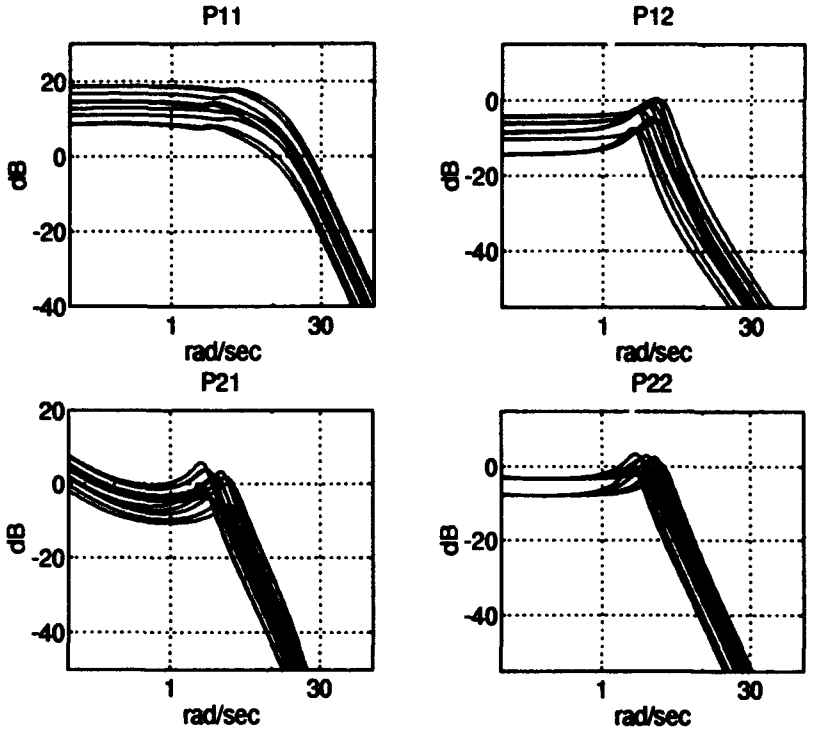

The PCT implementation of the lateral channel is shown in Fig. 5.2. $G_A(s)$ is given by Eq. (4.9). Actuator dynamics are given in Eqs. (2.9) and (2.10). $\mathbf{W} = \{w_{ij}\}$ is a 2×2 weighting matrix which is designed as an aileron-rudder interconnect.

Figure 5.2 Lateral PCT Implementation

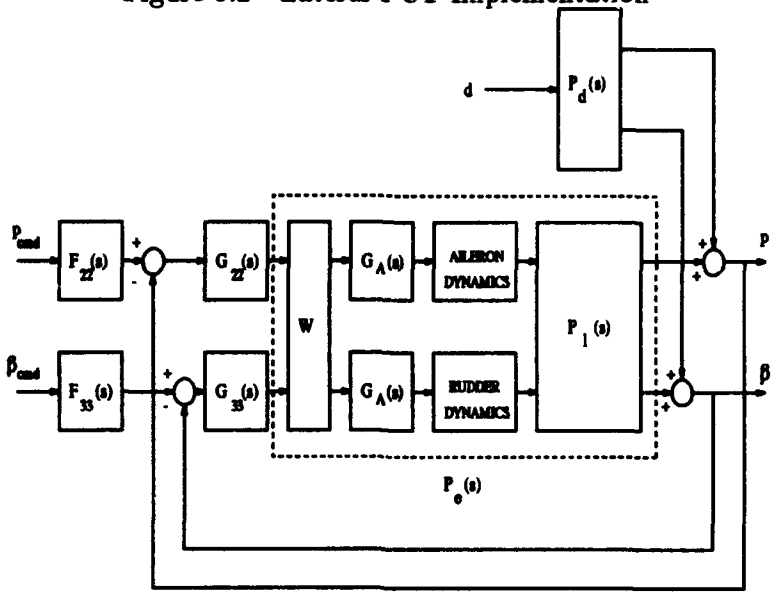

5.3 Loaded, Effective and MISO Equivalent Plants

The roll and yaw channels are designed sequentially. For presentation purposes, the designs are described simultaneously here.

5.3.1 Loaded Plants. Like the longitudinal channel, lateral plants are generated with the modified *Matlab* macro in Appendix A. Three different matrices are generated for the lateral channel. One **A** matrix for each flight condition is generated. This matrix is the same for both the tracking and disturbance dynamics. Two **B** matrices are created, one for $\mathbf{P}_l(s)$ and one for $\mathbf{P}_d(s)$. From the appropriate **A** and **B** matrices, the MIMO CAD Package creates the 2×2 tracking dynamics matrix $\mathbf{P}_l(s)$ and the 2×1 disturbance dynamics matrix, $\mathbf{P}_d(s)$. Transfer functions related to the β output contain non-minimum phase (n.m.p.) elements. $\mathbf{P}_l(s)$ is shown in Eq. (5.3). $\mathbf{P}_d(s)$ is shown as:

$$\mathbf{P}_d(s) = \begin{bmatrix} \frac{p_d(s)}{\delta_a(s)} \\ \\ \frac{\beta_d(s)}{\delta_a(s)} \end{bmatrix} \tag{5.4}$$

The transfer functions which comprise $\mathbf{P}_l(s)$ and $\mathbf{P}_d(s)$ for all flight conditions used in the lateral design are listed in Appendix C. The frequency responses of $\mathbf{P}_l(s)$ and $\mathbf{P}_d(s)$ are shown in Fig. 5.3 and Fig. 5.4 respectively.

Figure 5.3 Lateral $\mathbf{P}_l(s)$ Frequency Responses

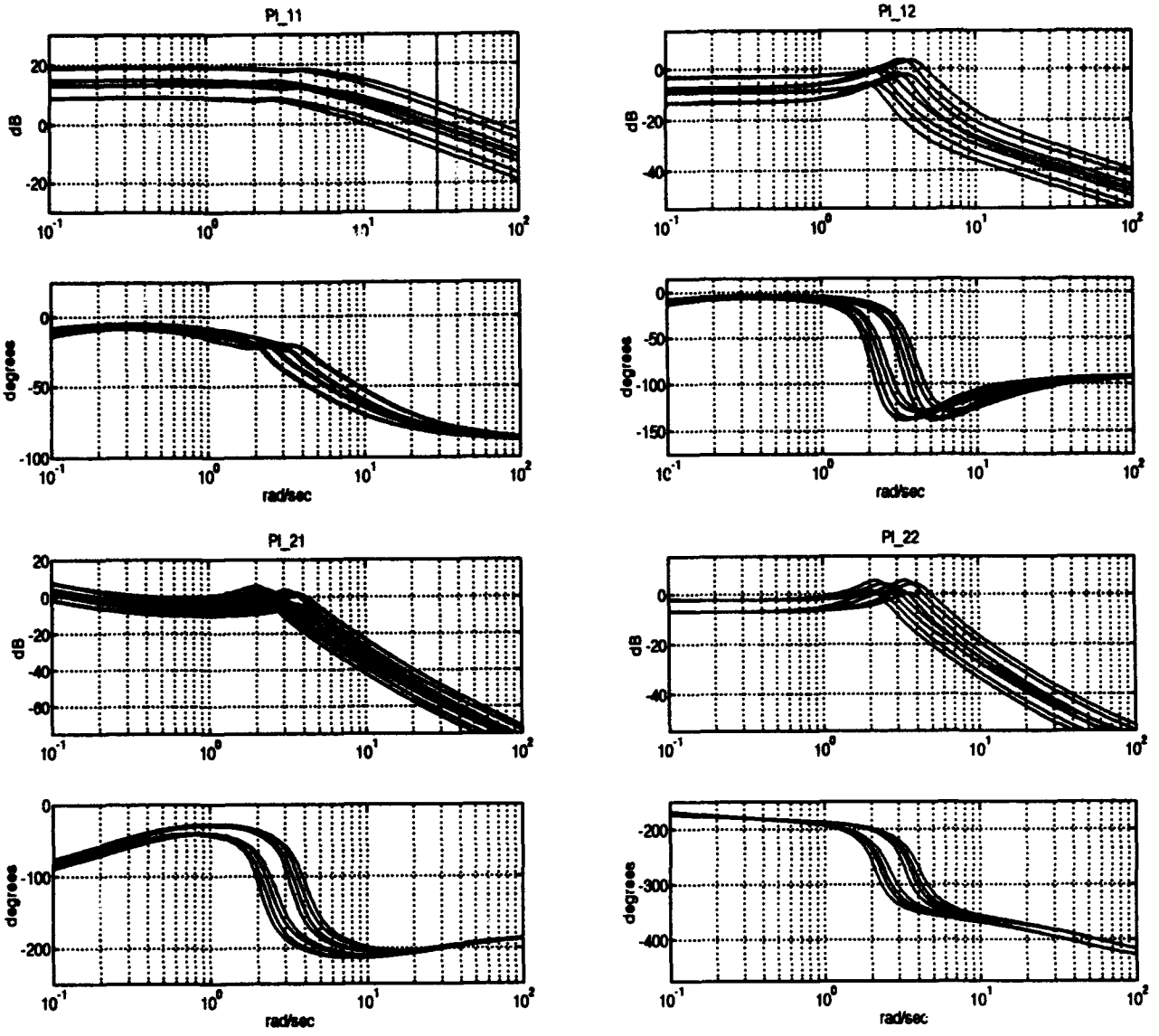

Figure 5.4 Lateral $\mathbf{P}_d(s)$ Frequency Responses

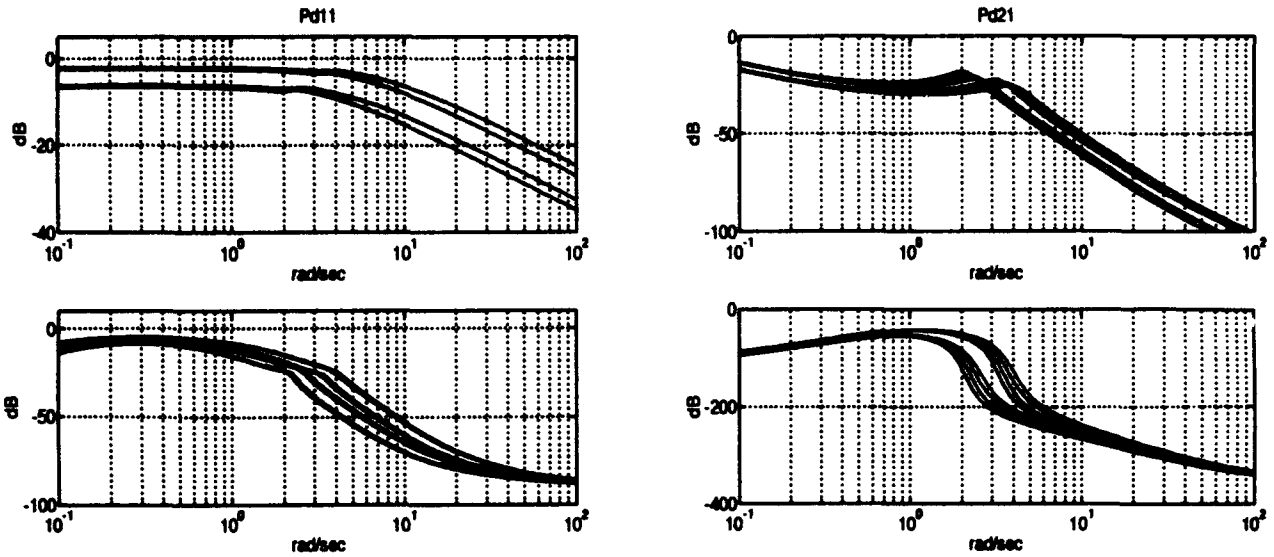

5.3.2 Effective Plants. Bare aircraft dynamics are combined with actuator dynamics, PCT dynamics and a weighting matrix to form the effective plants $\mathbf{P}_e(s)$. These plants are used in the QFT loop-shaping process.

The $2x2$ weighting matrix $\mathbf{W}$ is used as an aileron-rudder interconnect. When Lambda rolls in response to an aileron deflection, sideslip is induced. A non-zero element in $w_{2,1}$ causes the rudder to deflect whenever the aileron deflects. The induced rudder deflection counters the natural tendency of the aircraft to generate sideslip when responding to a roll command. The reduction of the β output due to a roll command by use of a weighting matrix minimizes the control efforts required by the QFT controller. Likewise, a non-zero $w_{1,2}$ element causes the aileron to deflect when a command is sent to the rudder. Because the rudder is not intended to be used often in a coordinated aircraft and because the roll induced by a rudder command is negligible, $w_{1,2}$ is set to 0. Diagonal terms are set equal to 1 since no amplification or attenuation of command signals is

desired. To keep the system order to a minimum, $w_{2,1}$ is considered as only a gain element. No additional dynamics are introduced.

The weighting matrix element $w_{2,1}$ is chosen through analysis of the aircraft open-loop time response. The open-loop response includes actuator dynamics. The value of $w_{2,1}$ which best minimizes β for a short time span is 1.0. Figure 5.5 compares the open-loop response of $\mathbf{W} = \begin{bmatrix} w_{1,1} & w_{1,2} \\ w_{2,1} & w_{2,2} \end{bmatrix} = \begin{bmatrix} 1 & 0 \\ 0 & 1 \end{bmatrix}$ with $\mathbf{W} = \begin{bmatrix} 1 & 0 \\ 1 & 1 \end{bmatrix}$.

Figure 5.5 Weighting Matrix Effect on Open-Loop Response

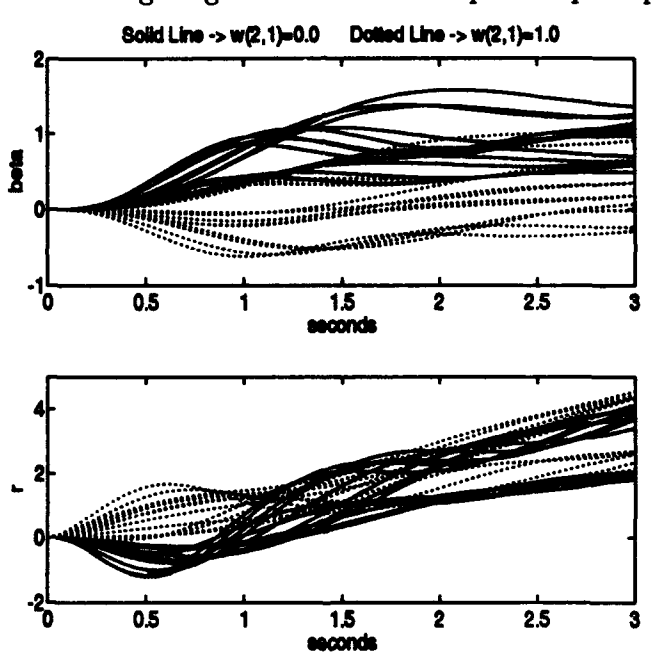

It is seen that when $w_{2,1} = 1.0$ the median excursion of β is centered about $\beta = 0$. The rudder induces a positive yaw rate to maintain β as close to 0 as possible. An adverse effect of a non-zero element in $w_{2,1}$ is an increase in the peak the β response due to a disturbance input. A large pitch rate is induced by the modeled lateral disturbance. The aileron command to counter that large

rate interconnects to the rudder causing the rudder to over compensate yaw motion. However, the postive results of cross-coupling rejection outweigh the negative effects of disturbance rejection.

Frequency responses of the effective plants with $w_{2,1} = 1.0$ are shown in Fig. 5.6. Appendix C lists the effective lateral plants.

Figure 5.6 Lateral $\mathbf{P}_e(s)$ Frequency Responses

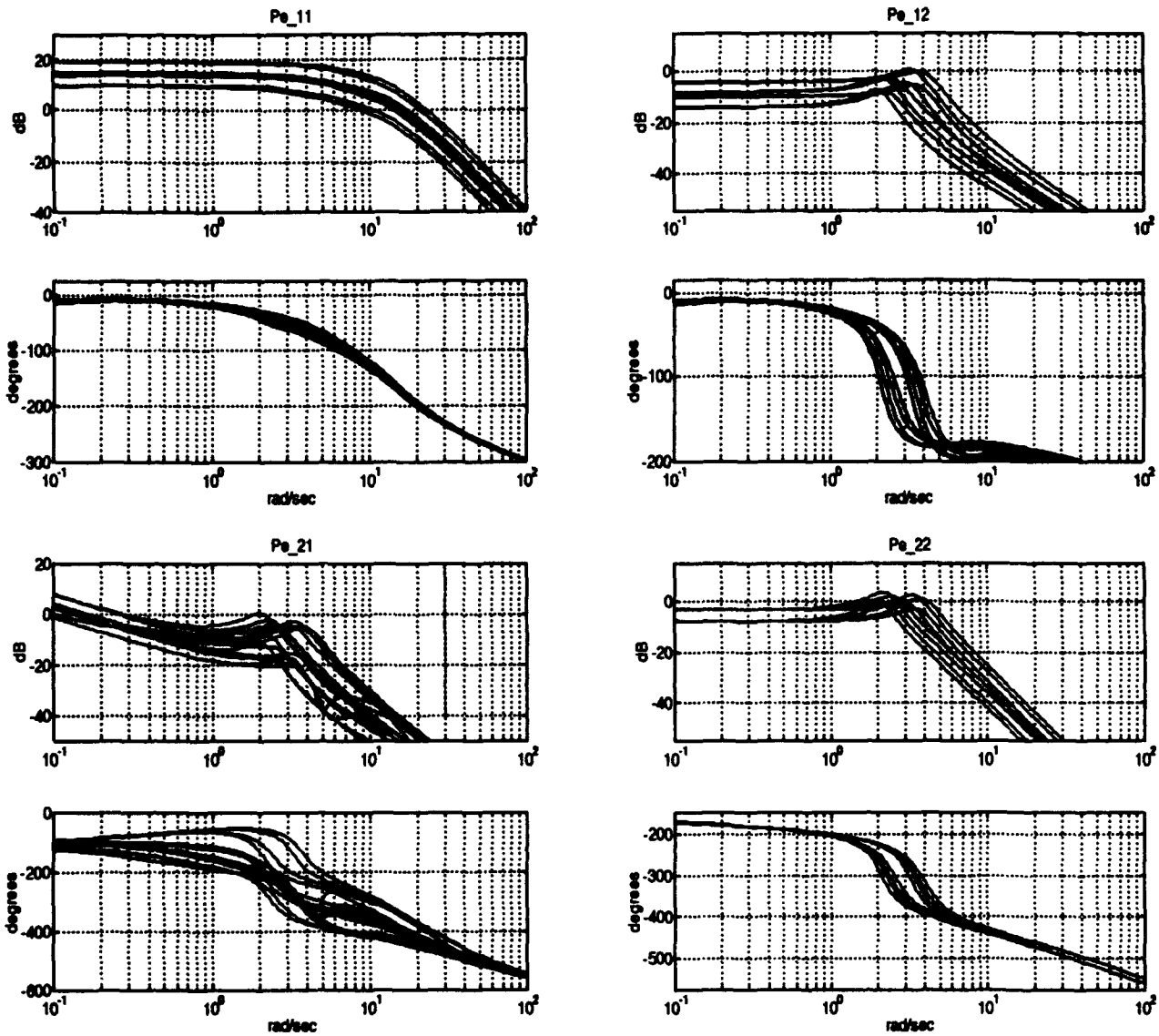

5.3.3 MISO Equivalent Loops. The MIMO QFT method for an m×m plant requires the formation of m^2 equivalent MISO loops for design as shown in Fig. 5.7 [5]. Compensators are designed in the same manner as a simple 1×1 QFT design. Each MISO loop has a tracking input and a disturbance input. The tracking input is the external reference command applied to the plant. The disturbance input represents the cross-coupling from other channels. The diagonal compensator and prefilter matrices are given by:

$$\mathbf{G}(s) = \begin{bmatrix} g_{11} & 0 & 0 \\ 0 & g_{22} & 0 \\ 0 & 0 & g_{33} \end{bmatrix} \tag{5.5}$$

and

$$\mathbf{F}(s) = \begin{bmatrix} f_{11} & 0 & 0 \\ 0 & f_{22} & 0 \\ 0 & 0 & f_{33} \end{bmatrix} \tag{5.6}$$

Therefore the off-diagonal loops only have disturbance inputs.

The equivalent loop transfer functions q_{ii} are formed by taking the inverse of the plant matrix $\mathbf{P}_e(s)$ and then inverting each element of $\mathbf{P}_e^{-1}(s)$.

$$\mathbf{P}_e^{-1}(s) = \begin{bmatrix} p_{22}^* & p_{23}^* \\ p_{32}^* & p_{33}^* \end{bmatrix} \tag{5.7}$$

and:

$$\mathbf{Q}(s) = \begin{bmatrix} \frac{1}{p_{22}^*} & \frac{1}{p_{23}^*} \\ \frac{1}{p_{32}^*} & \frac{1}{p_{33}^*} \end{bmatrix} = \begin{bmatrix} q_{22} & q_{23} \\ q_{32} & q_{33} \end{bmatrix} \tag{5.8}$$

The elements of $\mathbf{Q}(s)$ are the q_{ii} transfer functions which appear in the equivalent loops for each plant case.

Two methods exist for forming the equivalent loops. The first method, Method One, treats the loops as entirely separate QFT designs. Loop transmissions L_i from previously completed loops are not considered in cross-coupling disturbance rejection. The second method, Method Two, is an improvement on the first in that it takes into account loop transmissions of previously designed loops. Previously completed loops alter the disturbance input. When starting the design process, Method One is used for loop 2. For loop 3, Method Two is used which requires the generation of a new expression for q_{33} [11]. This new expression is denoted as q_{33_e} and is given by:

$$q_{33_e} = q_{33}\frac{1 + L_2}{1 + L_2 - \gamma_{23}} \tag{5.9}$$

where:

$$\gamma_{23} = \frac{p_{32}p_{23}}{p_{33}p_{22}} \tag{5.10}$$

A general rule of thumb exists for choosing the first loop to be designed. Normally, the loop with the smallest bandwidth is designed first which for this design is the yaw channel. However, because turn coordination is desired, the roll channel is designed first. By designing the roll channel first, roll loop transmissions are modeled in the yaw channel. This allows loop-shaping to precisely eliminate cross-coupling of roll commands into β, as desired for turn coordination.

The MIMO CAD Package forms the $\mathbf{Q}(s)$ matrices from the $\mathbf{P}_e(s)$ matrices and in turn forms q_{33_e}. Frequency response data of $q_{22}(s)$ and $q_{33_e}(s)$ are shown in Fig. 5.8.

Figure 5.7 m^2 Equivalent MISO Loops

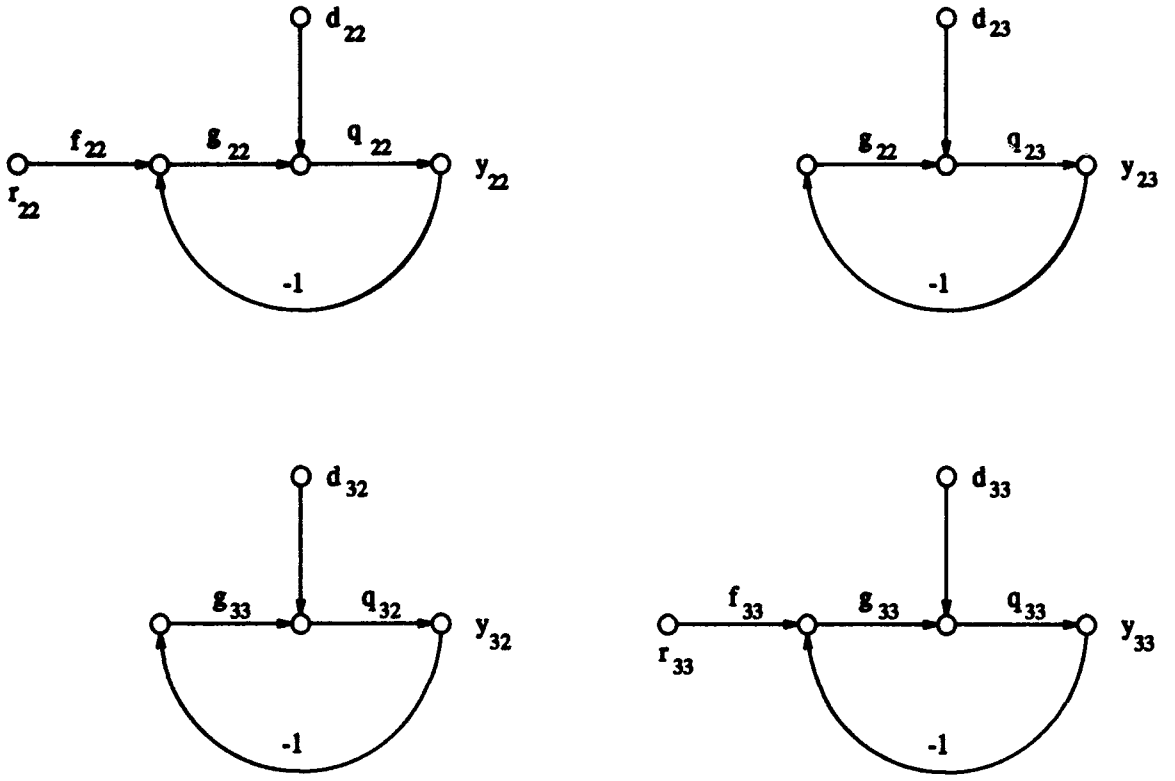

Figure 5.8 Frequency Responses of $q_{22}(s)$ (left) and $q_{33e}(s)$ (right)

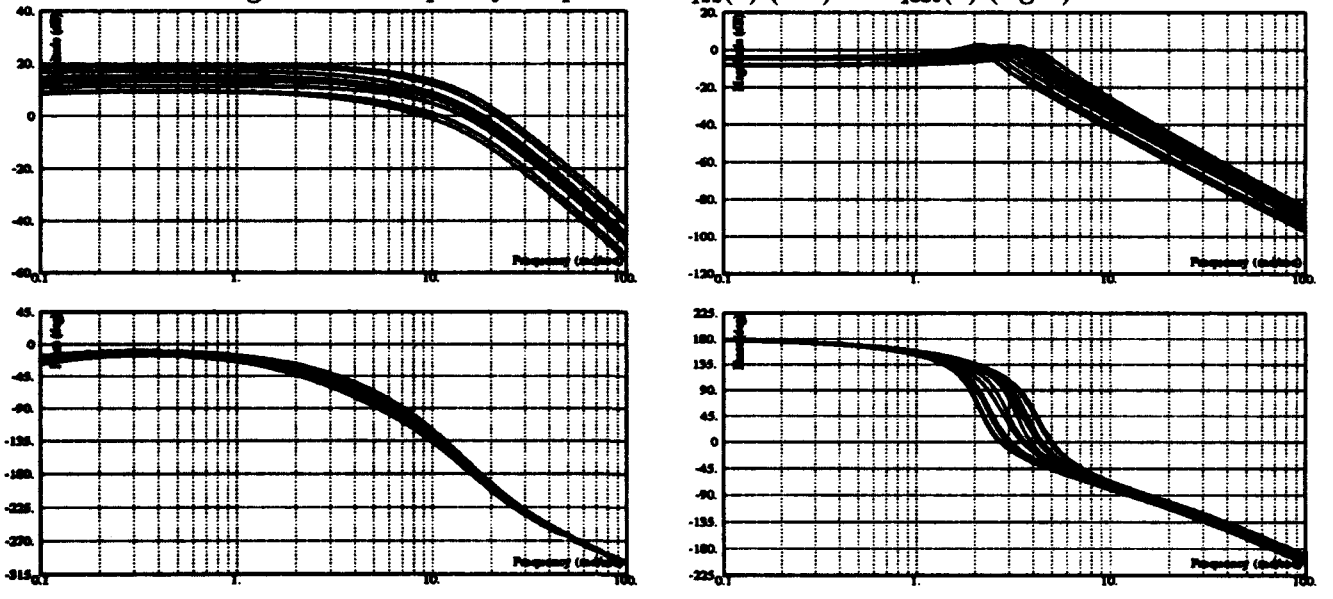

5.4 Plant Templates

A set of templates is generated for both lateral channels from the frequency response of $q_{22}(s)$ and $q_{33_e}(s)$. Plant template frequencies are chosen as described in Sec. 4.4. For the lateral channel, frequencies of $w = 0.5, 1, 2, 3.5, 5, 8, 10, 20$ and 100 are chosen.

As in the longitudinal channel, plants which do not define a template boundary in either loop are eliminated. Two plants are also added to expand the boundaries. The design is therefore accomplished with thirteen plants. Table 5.1 lists the thirteen flight conditions used in the lateral design. Plant templates generated with the thirteen flight conditions are shown in Fig. 5.9 and Fig. 5.10.

Table 5.1 Thirteen Final Lateral Flight Conditions

#	*cg* (*in*)	*Speed* (ft/sec)	Q_∞ (lbs/ft^2)	*Weight* (*lbs*)	ζ_e	ζ_r	ζ_a
1	46.79	118.23	16.13	202.5	0.5	1	0.5
2	46.79	118.23	12.27	202.5	0.5	0.5	1
3	46.79	185.79	39.83	202.5	0.5	1	1
4	46.79	185.79	39.83	202.5	0.5	1	0.5
5	46.79	185.79	30.31	202.5	0.5	0.5	1
6	46.79	185.79	30.31	202.5	0.5	0.5	0.5
7	46.79	118.23	16.13	202.5	0.5	1	1
8	46.79	118.23	16.13	202.5	0.5	1	0.5
9	46.79	118.23	12.27	202.5	0.5	0.5	1
10	46.79	185.79	39.83	202.5	0.5	1	1
11	46.79	185.79	30.31	202.5	0.5	0.5	1
12	46.79	152.00	26.66	202.5	0.5	1	0.5
13	46.79	152.00	20.29	202.5	0.5	1	1

Examination of plant location within the templates of each channel reveals that failures cause a drop in gain and a slight increase in phase lag. In addition to failures, gain variations are caused by velocity changes. Gain increases with velocity. Velocity and altitude variation cause the greatest variation in phase. The maximum variation of template parameters are:

Figure 5.9 Lateral Plant Templates - Roll Channel

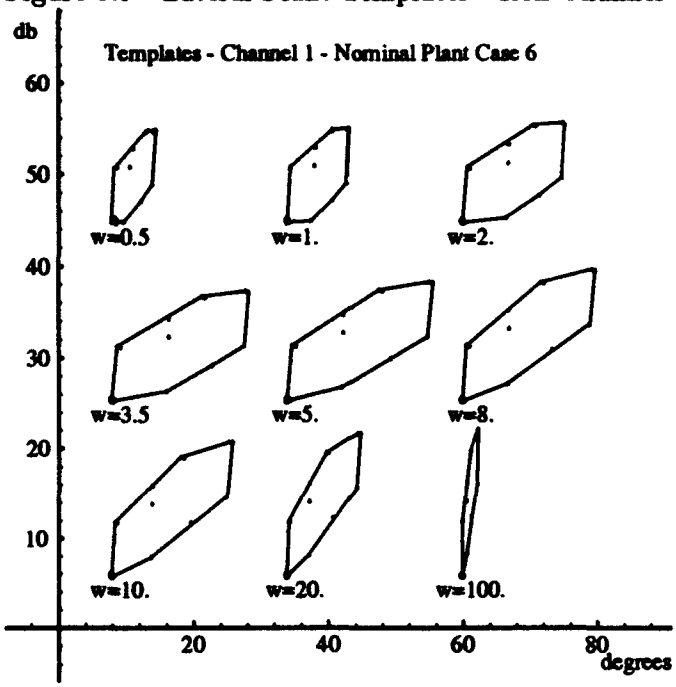

Figure 5.10 Lateral Plant Templates - Yaw Channel

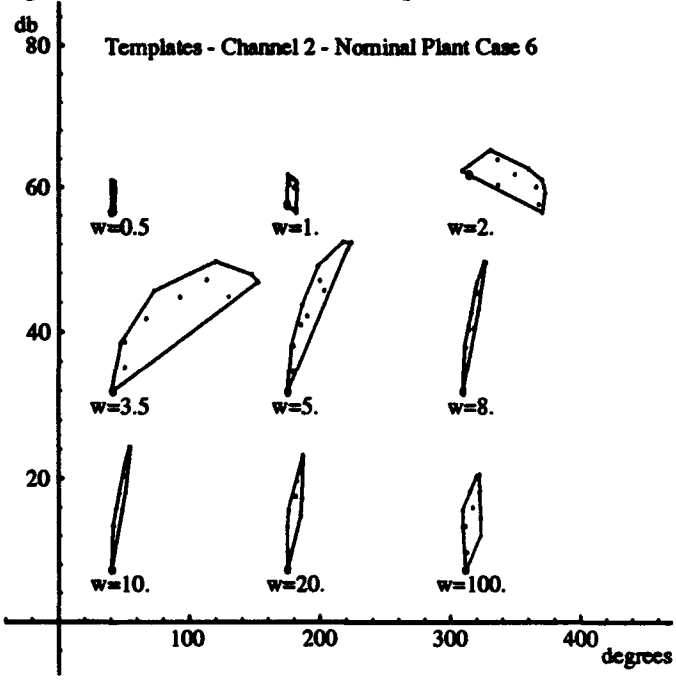

- Loop1 - 17 dB @ $w = 100$

  $24°$ @ $w = 5$

- Loop2 - 21 dB @ $w = 100$

  $106°$ @ $w = 3.5$

Plant #6 is chosen as the nominal plant for both channels. The nominal plant transfer functions are:

$$q_{22}(s) = \frac{237557.98s(s - 40.9676)}{(s - 0.0427)(s - 40.7745)(s + 3.5194)(s + 11.0737 \pm j10.0893)(s + 100)} \tag{5.11}$$

and:

$$q_{33_e}(s) = \frac{49084.0569(s - 40.9676)}{(s + 0.4233 \pm j2.0809)(s + 4.4707)(s + 100)(s + 2612.7424)} \tag{5.12}$$

5.5 Loop-Shaping

Tracking, cross-coupling and disturbance rejection bounds are generated with the MIMO QFT CAD Package. Like the longitudinal channel, not all bounds can be met and still allow a reasonable system bandwidth. Loop-shaping is therefore performed with emphasis on meeting tracking bounds. High frequency bounds are readily violated to maintain a low system bandwidth.

Figures 5.11 and 5.12 show the nominal open-loop transmissions for channel 1 and 2 respectively with $G_{ii}(s) = 1$. Tracking bounds are displayed. It is seen that bounds for the yaw channel are much less restrictive. Initially, bounds at $w = 0.5\frac{rad}{sec}$ are not included in the design process which results in significant tracking errors in the yaw channel over the time span of interest. While

Figure 5.11 Nominal Open-Loop Transmissions - Roll Channel

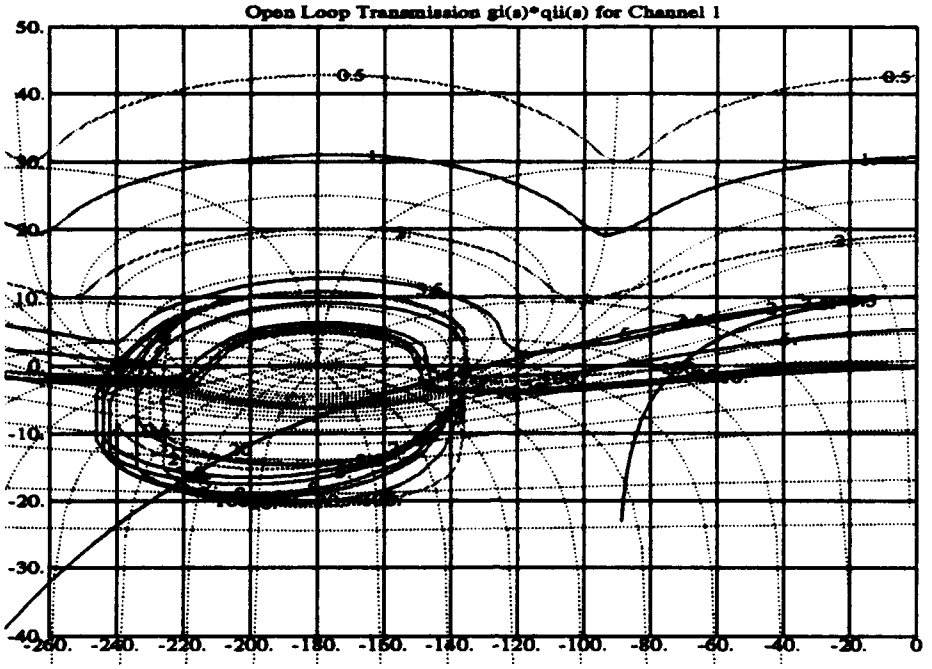

Figure 5.12 Nominal Open-Loop Transmissions - Yaw Channel

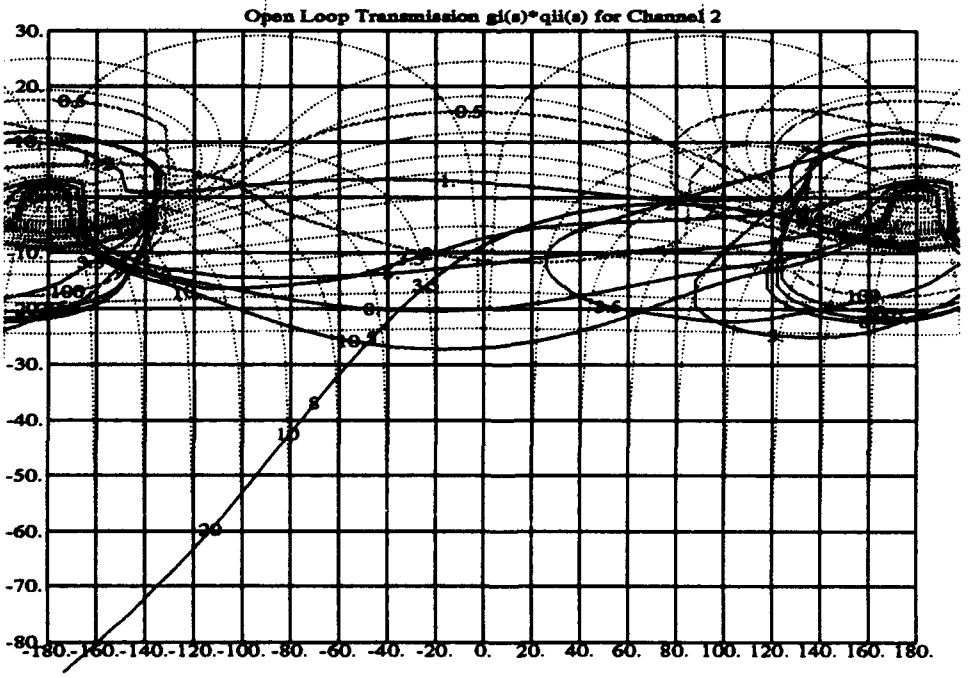

tracking in the yaw channel is not of critical interest, it is still desirable to have some degree of control in that channel with β feedback employed. Addition of a bound at $w = 0.5\frac{rad}{sec}$ and adjustment of the loop shape greatly improves tracking. The improved tracking also improves disturbance rejection because of the increased gain. Tracking performance can be improved further, but it is desired to keep a relatively low gain and bandwidth for the yaw channel due to the noise associated with β feedback.

5.6 Compensators $G_{ii}(s)$

Lambda lateral channels have lower bandwidths than the longitudinal channel. This greatly facilitated loop-shaping as poles of the lateral compensators are not as difficult to place. Loop-shaping results in the following compensators:

$$G_{22}(s) = \frac{6200(s+0.1)(s+3)(s+9 \pm j15.59)}{s^2(s+125)(s+130)(s+150)} \tag{5.13}$$

and:

$$G_{33}(s) = \frac{-5250(s+0.75)(s+1.6)(s+1.5 \pm j2)}{s(s+0.1)(s+15)(s+45)(s+50)} \tag{5.14}$$

The physical implications of the URV response require that: (1) the yaw channel loop transmission have a $-180°$ shift in phase, thus $G_{33}(s)$ must have a negative gain; and (2) the yaw rate r and sideslip β have opposite signs in the gain term of their respective transfer functions which also requires that the feedback signals have their sign inverted.

Figures 5.13 and 5.14 show the final loop-shape for the roll and yaw channel respectively. Note the tracking violations at low frequencies for the roll channel. These violations are assumed to have negligible effect on the tracking response. Time domain simulations validate this assumption.

Figure 5.13 Roll Channel Final Loop-Shape

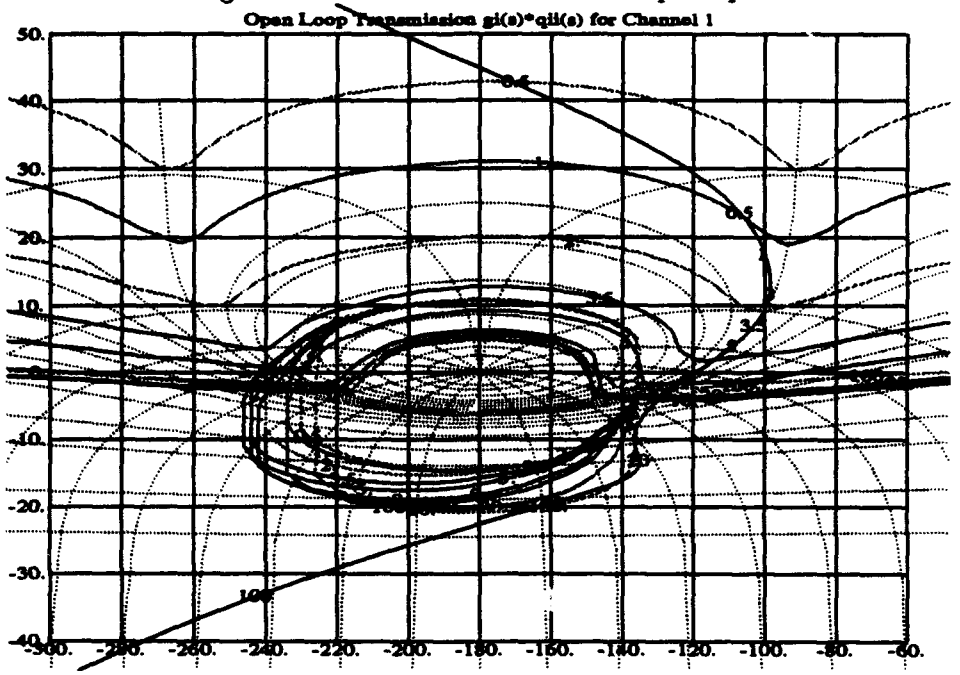

Application of the Tustin approximation to Eq. (5.13) and Eq. (5.14) results in the following z-domain controllers:

$$G_{22}(z) = \frac{5.99046(z+1)(z-0.99800)(z-0.94175)(s-0.79808 \pm j0.25717)}{(z-1)^2(z+0.2)(z+0.13043)(z+0.11111)} \tag{5.15}$$

and:

$$G_{33}(z) = \frac{-22.12114(z+1)(z-0.98511)(z-0.96850)(z-0.96968 \pm 0.038811)}{(z-1)(z-0.99800)(z-0.73913)(z-0.37931)(z-0.33333)} \tag{5.16}$$

Figure 5.14 Yaw Channel Final Loop-Shape

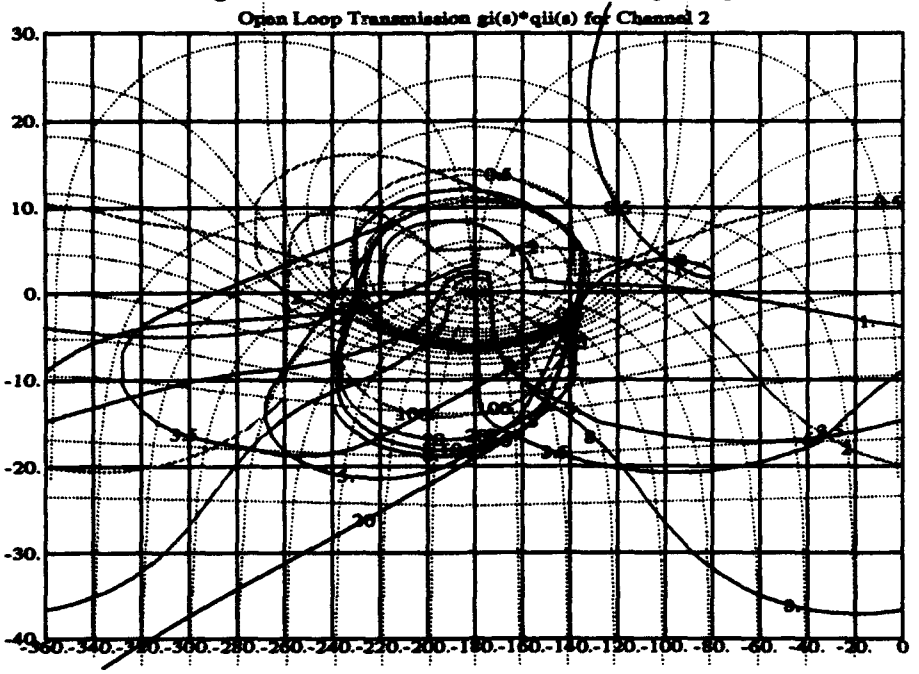

Comparison of the s-domain and z-domain frequency responses of each controller show good correlation over the region of interest. See Fig. 5.15.

5.7 *Prefilters* $F_{ii}(s)$

The following prefilters are formed for each channel:

$$F_{22}(s) = \frac{0.006(s+100)^2}{(s+6)(s+10)} \tag{5.17}$$

and:

$$F_{33}(s) = \frac{0.0008(s+1)(s+100)^2}{(s+2)(s+1.4 \pm j1.42829)} \tag{5.18}$$

Similar to the longitudinal prefilter, nondominant zeros are added to the lateral prefilters.

Figure 5.15 Lateral Controller Frequency Responses

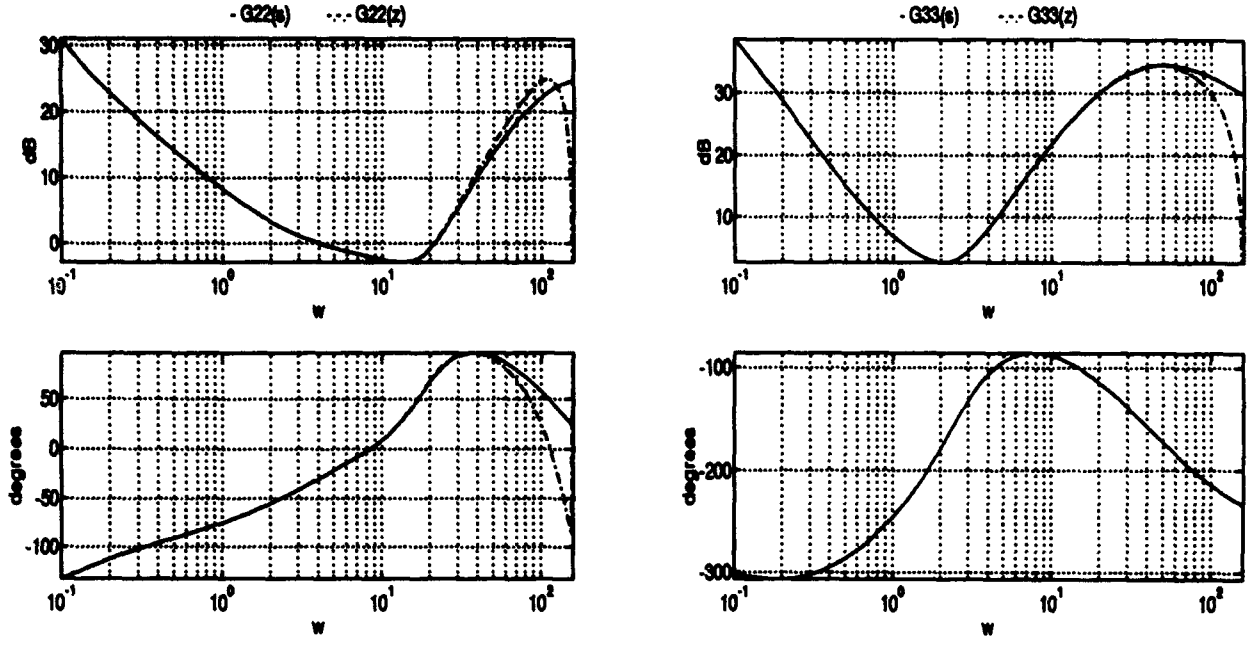

Figure 5.16 shows the closed-loop frequency response for each tracking response and for each cross-coupling response. It is seen that roll channel tracking bounds are violated above $w = 10\frac{rad}{sec}$. This corresponds to the violation of tracking bounds on the Nichol's Chart. Violations do not occur until the closed-loop response is significantly attenuated. The roll channel closed-loop frequency response is therefore considered adequate.

Tracking bound violations also occur in the yaw channel. Initial design attempts result in a controller and prefilter which meet the specified yaw tracking bounds. However, the gain of this controller is large enough to make the implementation of it impractical. The high gain controller amplifies sensor noise and causes significant chatter in the rudders. A new controller is therefore designed which somewhat violates tracking bounds, but does not excessively amplify sensor noise (see Sec. 5.10). The tracking bounds could be better satisfied if a higher order prefilter is used. Because of sampling rates and the extent to which the yaw channel is used for control, a higher order

Figure 5.16 Roll and Yaw Channel Closed-Loop Frequency Responses

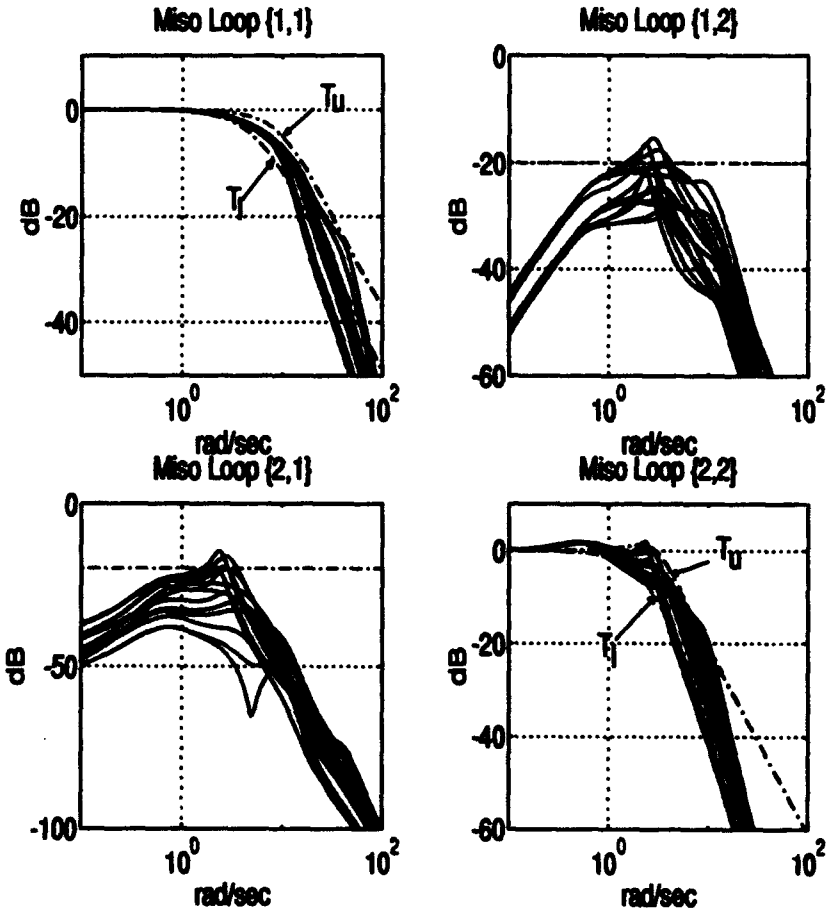

prefilter is not desired either. Simulations determine the adequacy of the designed yaw channel controller.

Cross-coupling rejection is seen to be quite good. Violations occur in the roll response due to a rudder input. The violations are not corrected because the rudder is not a primary command surface and the violations do not result in inadequate time domain responses.

The z-domain representation of the lateral compensators derived via the Tustin transformation is:

$$F_{22}(z) = 0.020583\frac{z^2}{(z-0.88679)(z-0.81818)} \tag{5.19}$$

and:

$$F_{33}(z) = 0.0030811\frac{(z-0.98020)(z)^2}{(z-0.96078)(z+0.97200 \pm j0.027777} \tag{5.20}$$

Figure 5.17 shows the z-domain representations are valid over the region of interest.

5.8 Validation of the QFT Design

It is shown that the closed-loop tracking responses are adequate in meeting the given specifications. Open-loop transmissions shown in Fig. 5.18 and Fig. 5.19 show that the $\gamma = 45°$ specification is satisfied in both channels. Figure 5.20 shows that the chosen disturbance responses are also satisfied.

Figure 5.17 Lateral Prefilter Frequency Responses

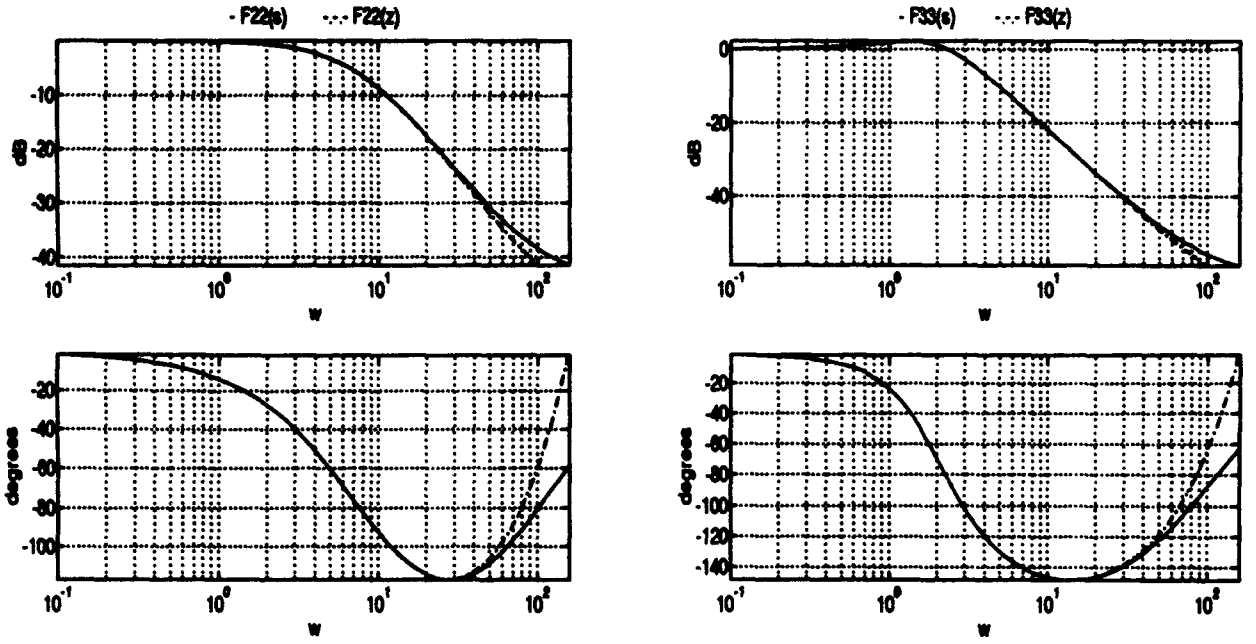

Figure 5.18 Roll Channel Open-Loop Transmission with $G_{22}(s)$ Included

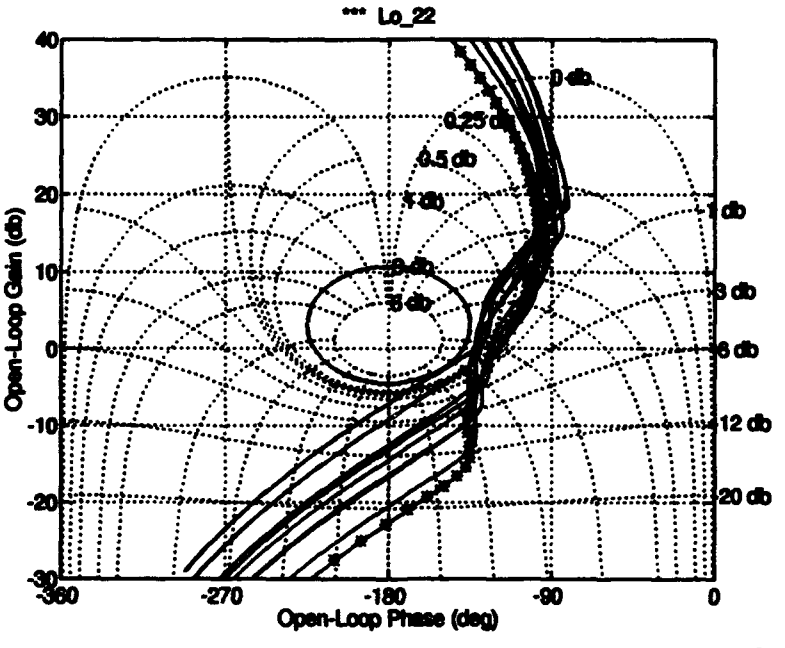

Figure 5.19 Yaw Channel Open-Loop Transmission with $G_{33}(s)$ Included

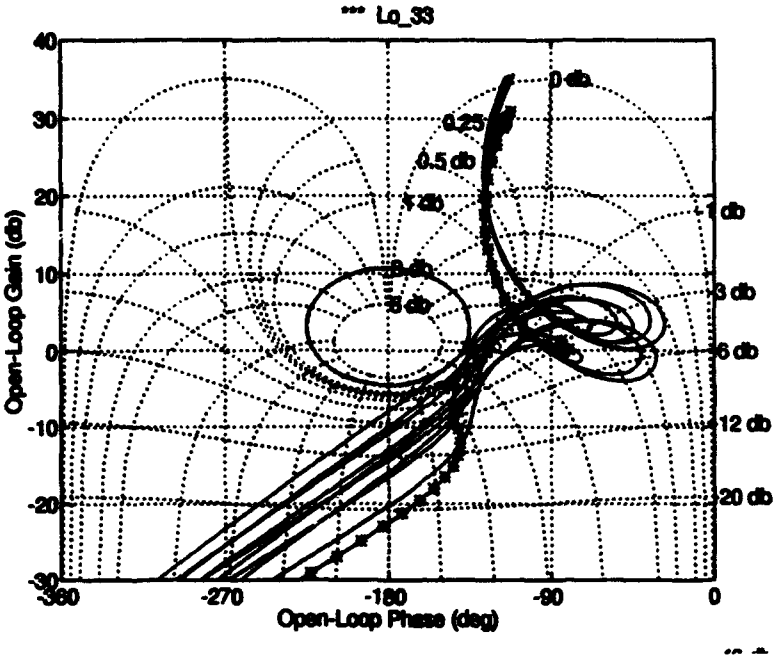

Figure 5.20 Lateral Disturbance

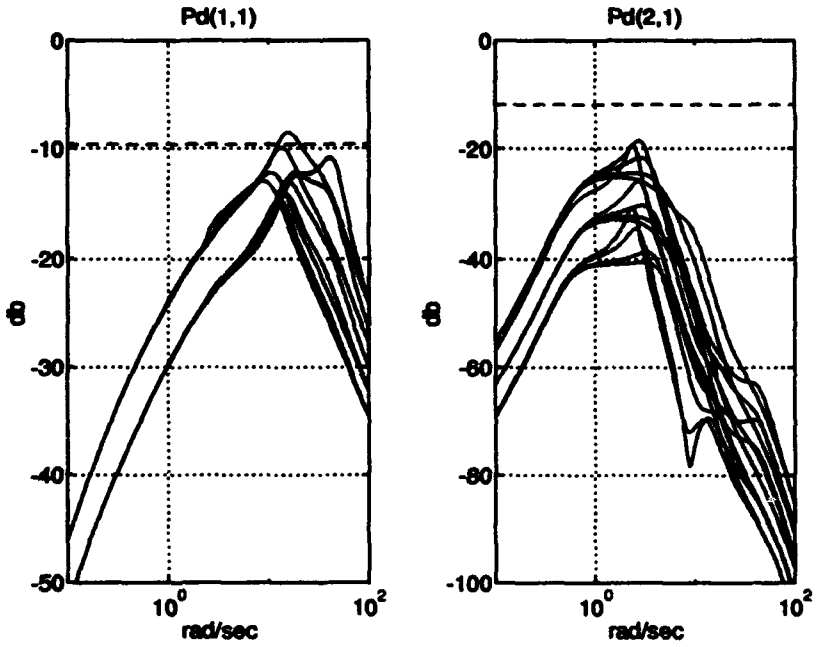

5.9 *Simulation*

Time domain simulations verify the effectiveness of the designed lateral controllers. A *Simulink* model with non-linear actuator and rate gyro elements is used for the simulation. As in the longitudinal channel, prefilters and controllers are implemented in the z-domain while aircraft and actuator dynamics are in the s-domain. Figure 5.21 shows the *Simulink* block diagram used for the simulation of the lateral channel.

Figure 5.21 Lateral Channel Simulink Model

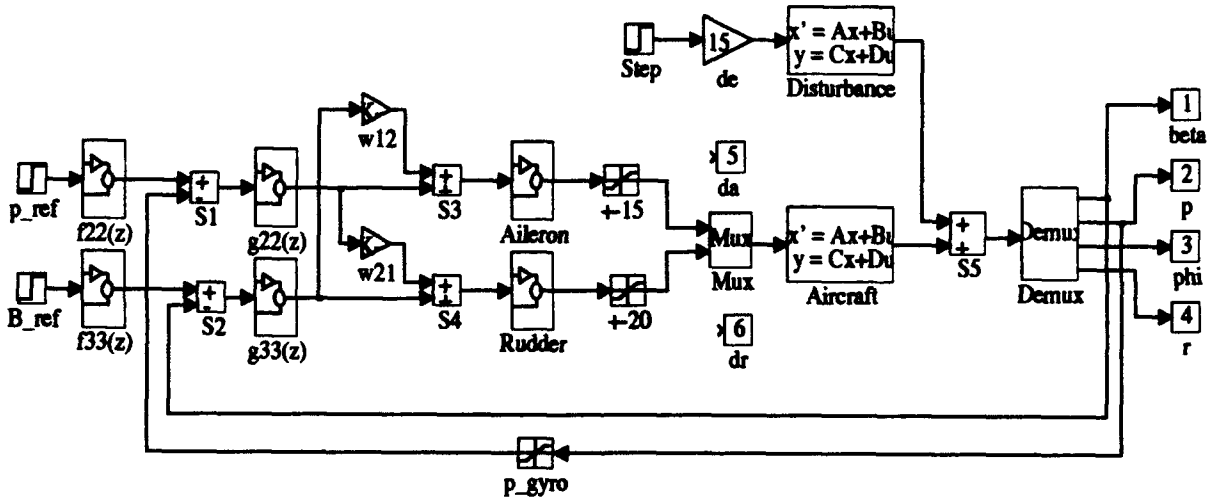

A unit step input is applied to each of the control inputs at different times. Figure 5.22 shows the lateral response to a $1\frac{deg}{sec}$ roll input. It is seen that the roll rate assumes the reference value very quickly. Also, the cross-coupling is limited very effectively. The peak value of β is only 0.075° for this input. Most plants remain even closer to zero. It is seen that elevator and rudder deflections

are minimal. Figure 5.23 shows the response to a β reference command of 1°. Note that the β response is not as "tight" as the p response. This is because of less stringent specifications on the β response since yaw is not the primary control channel. The cross-coupling into the roll channel is seen to be minimized by the controller. The maximum value of the roll angle is only 0.08°. Control surface deflections are well within actuator limits.

Figure 5.22 Roll Channel Tracking Response

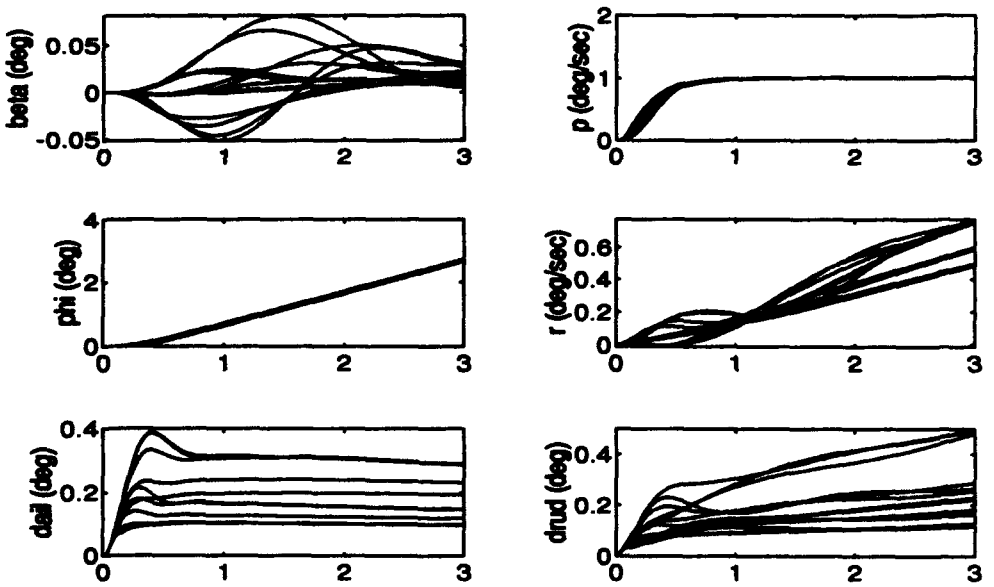

Figure 5.24 shows the lateral response to an elevator deflection. The elevator deflection assumes that one entire elevator is lost. The remaining elevator surface is deflected to its maximum value of 15°. The roll rate is seen to be effectively attenuated by the controller, limiting the roll angle displacement to a maximum value of 0.9°. The aileron is seen to assume a non-zero steady-state value. This deflection is required to counter the roll moment induced by the damaged elevator. The maximum steady-state deflection of $-3°$ still allows room for the aileron deflection to maintain control authority in the roll axis. The maximum value of the sideslip angle is 0.8° in the disturbance

Figure 5.23 Yaw Channel Tracking Response

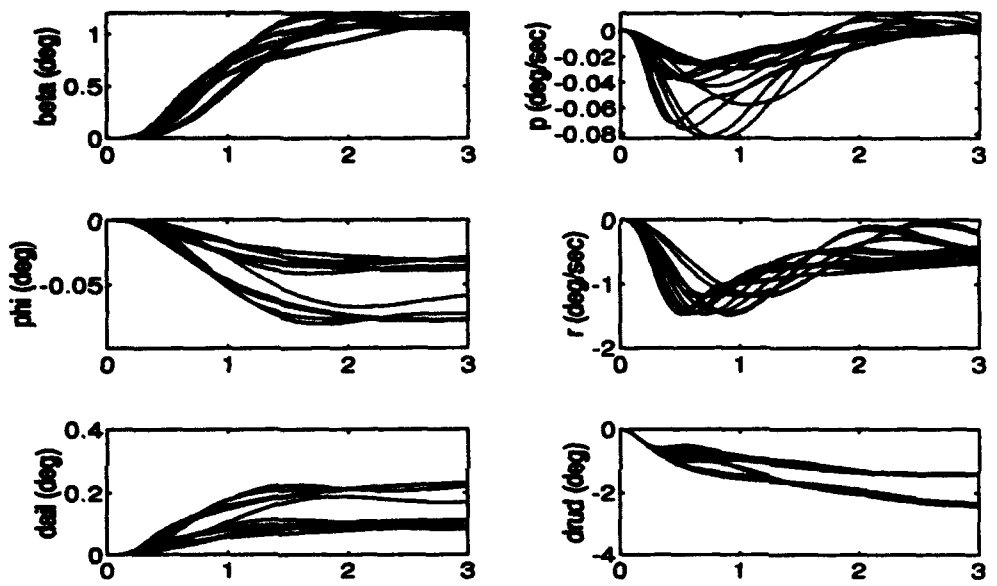

response. This value can be reduced by lowering the magnitude of $w_{2,1}$. However, the negative effects of $w_{2,1}$ on disturbance are far outweighed by the gains in cross-coupling rejection.

Actuator and gyro saturation effects are investigated only for the primary input channel (roll). A reference step input of $40\frac{deg}{sec}$ is applied to the system. It is seen that the roll rate starts to run away. This is due to saturation in the roll gyro. Therefore, for a 50% aileron failure, the gyros will saturate first. See Fig. 5.25.

5.10 Other Concerns

As in the longitudinal channel, pilot oscillations (p.i.o.) and sensor noise are concerns. The frequency response of three transfer functions are analyzed: roll reference to aileron, roll gyro noise to aileron and β sensor noise to aileron. The transfer function $\frac{\delta_r}{\beta_{ref}}$ is not analyzed since yaw control inputs are avoided with this design.

Figure 5.24 Lateral Channel Disturbance Response

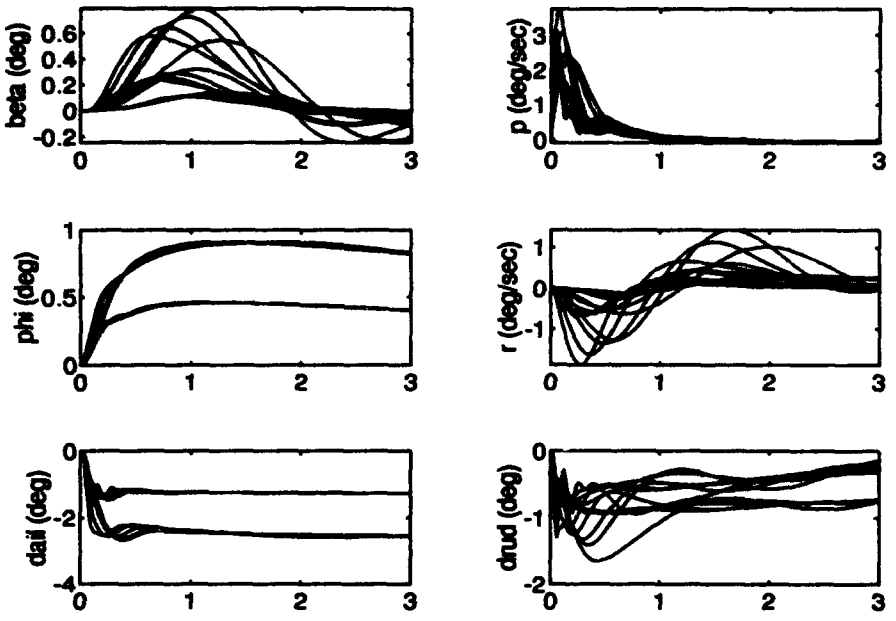

Figure 5.25 Roll Channel Tracking Response $40\frac{deg}{sec}$ Reference

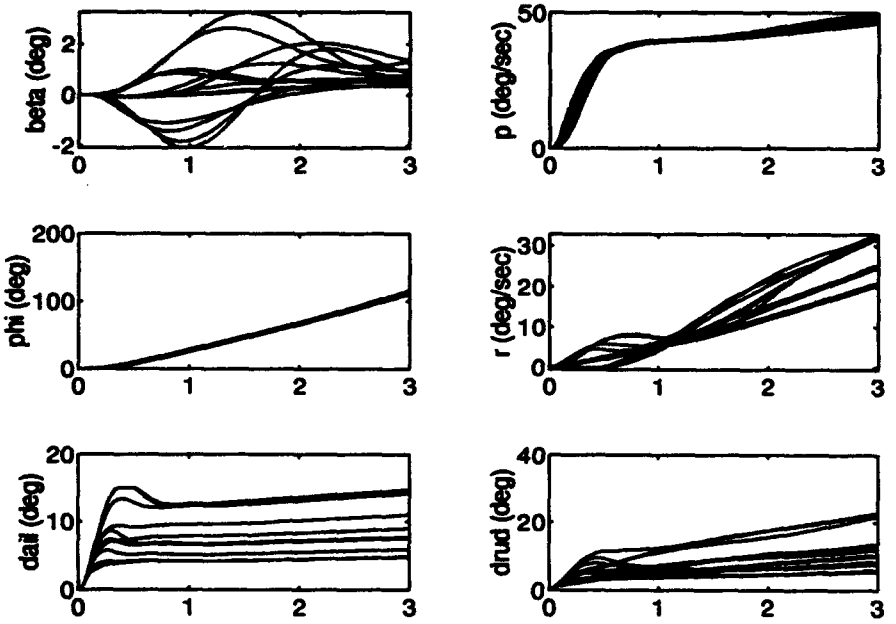

Figures 5.26 through 5.29 show the equivalent block diagrams of the aileron output/reference input signal and the aileron output/sensor noise input signal configurations and the corresponding frequency responses. It is seen that high frequency pilot oscillations and roll gyro noise are well attenuated.

Figure 5.26 Block Diagram of Aileron Output/Reference Input

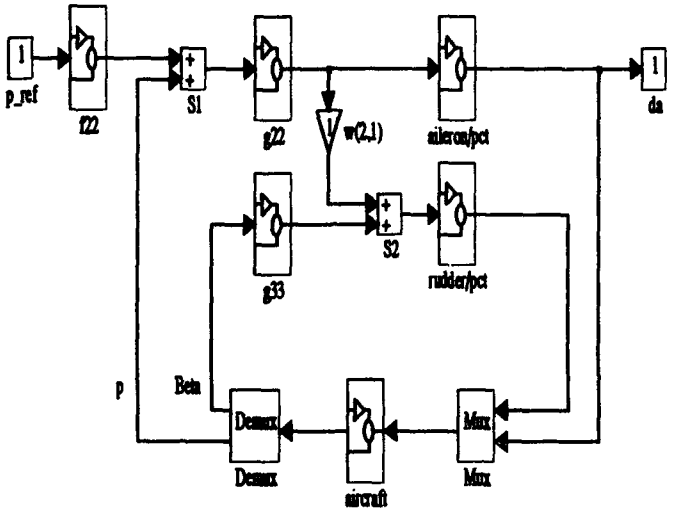

The effect of noise is a concern in the yaw channel especially when β feedback is to be used. The β sensor is a noisy sensor as it measures unsteady airflow dynamics. Excessive amplification of sensor noise can cause "chatter" in the rudders. Figure 5.30 shows the equivalent block diagram of the rudder response to sensor noise input and Fig. 5.31 shows the frequency response of the aileron to sensor noise transfer function. Amplification of the noise appears to be significant. However, the frequency response with the chosen $G_{33}(s)$ is significantly lower than the initial yaw channel design. Amplification of the noise above $5\frac{rad}{sec}$ is due to high gain in the G_{33} controller element (see

Figure 5.27 Frequency Response of Aileron to Reference

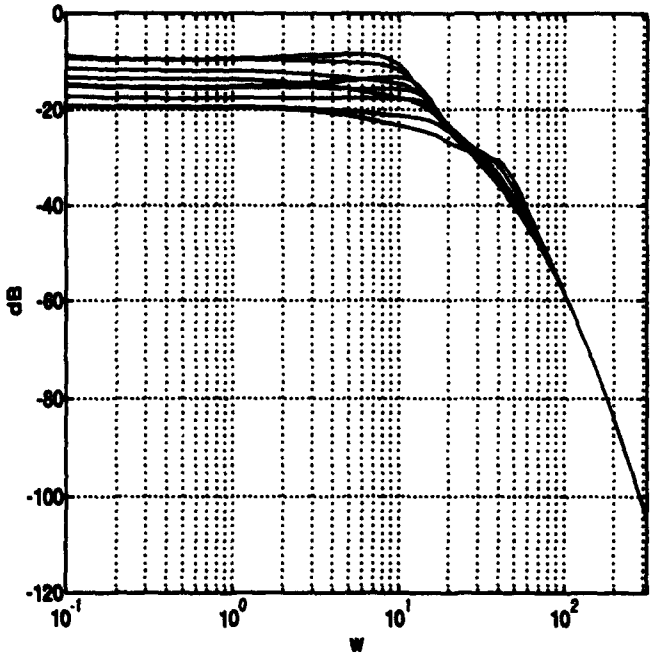

Figure 5.28 Block Diagram of Aileron Output/Roll Sensor Noise Input

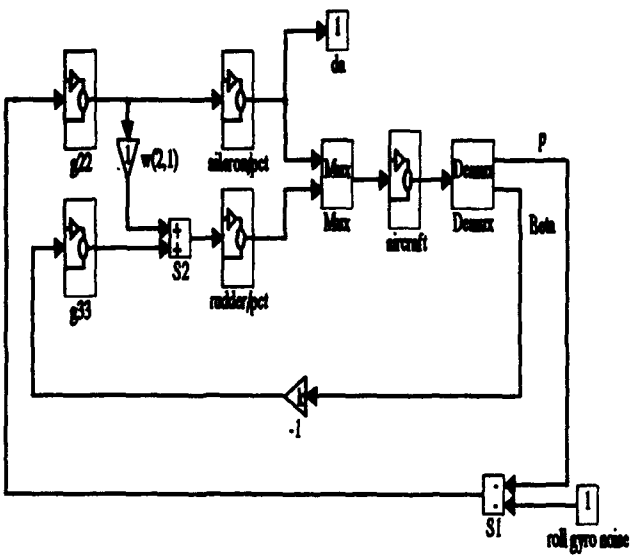

Figure 5.29 Frequency Response of Aileron to Sensor Noise

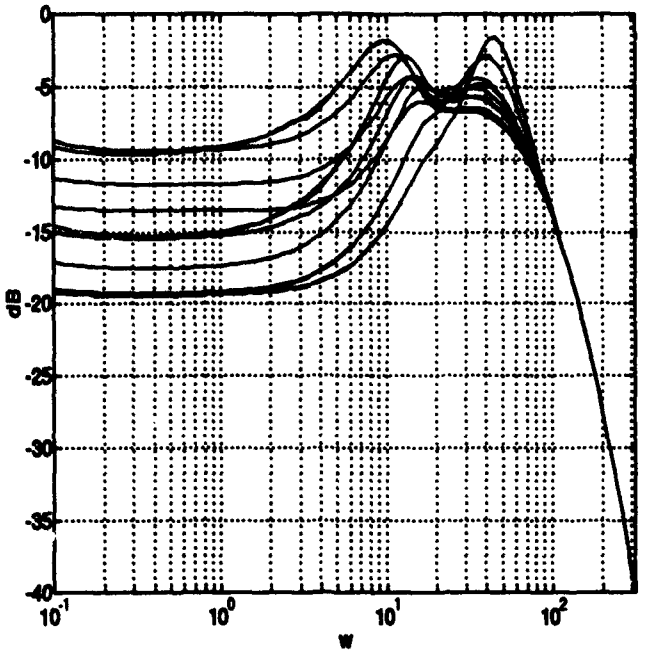

Fig. 5.15). When surface failures occur, the plant transfer functions experience a loss of gain and additional phase lag. To counter these effects, gain and phase lead are returned to the open-loop transmission with the compensator. This additional gain and phase lead, while restoring desired open-loop qualities, also amplifies sensor noise. The redesigned controller, while not perfectly meeting yaw channel specifications, maintains sensor noise amplification at reasonable levels.

Time domain simulations are performed using white Gaussian noise models of the Lambda sensors. Figure 5.32 and Fig. 5.33 show that efforts to reduce noise effects on the control surface outputs have been successful. Figure 5.32 shows the time domain response of the lateral channel to roll rate gyro noise. Roll gyro noise is seen to have a negligible effect on the aircraft states. Both the aileron and rudder experience a $\pm 0.1^{\circ}$ in response to the noise. The rudder chatters due to the aileron-rudder interconnect. Figure 5.33 shows the time domain response of the lateral channel to

Figure 5.30 Block Diagram of Rudder Output/β Sensor Noise Input

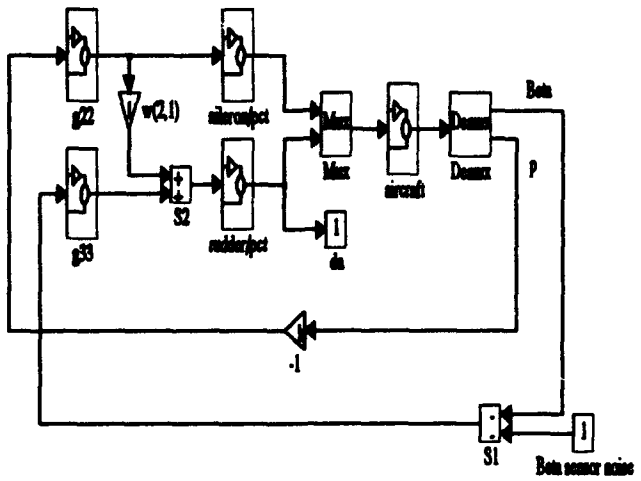

Figure 5.31 Frequency Response of Rudder to β Sensor Noise

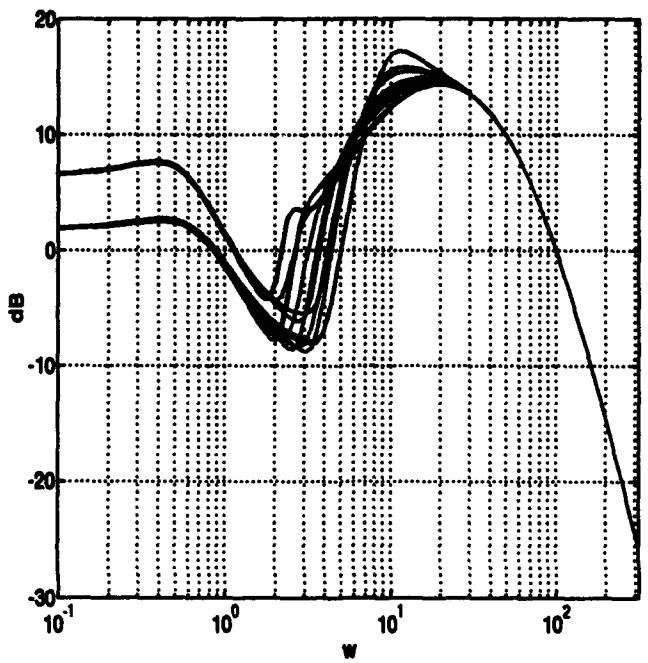

β sensor noise. Again, effects on the lateral states are negligible. The rudder experiences a $\pm 0.2°$ chatter. The aileron chatter is extremely small since there is no rudder-aileron interconnect.

Figure 5.32 Response of the Lambda to Roll Sensor Noise

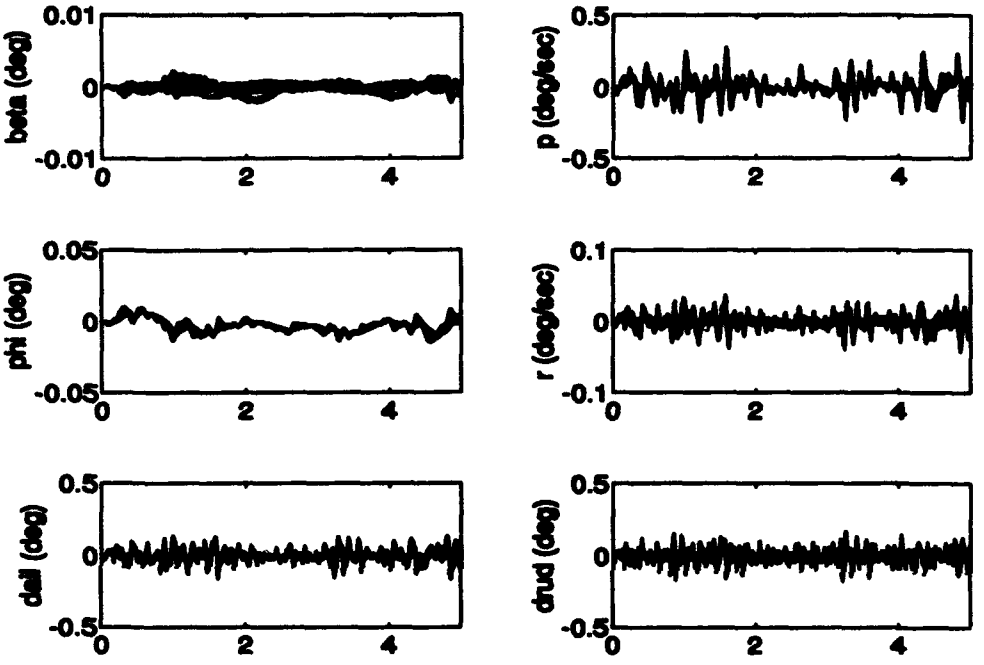

If further reduction of noise effects in either channel is desired, the controller can be redesigned for a smaller degree of damage to the control surfaces. This eases phase and gain requirements on the controllers, thus minimizing noise amplification. Another approach can be to include a sixth-order Butterworth filter in the feedback loops to filter sensor noise [1]. This needs to be included at the start of the QFT design process to ensure robust behavior of the resulting controller. Another option is to design the QFT controller around roll rate p and yaw rate r. The yaw gyro is not expected to be as noisy as the β sensor. However, coordination efforts will not be as direct as designing with β feedback.

Figure 5.33 Response of the Lambda to Beta Sensor Noise

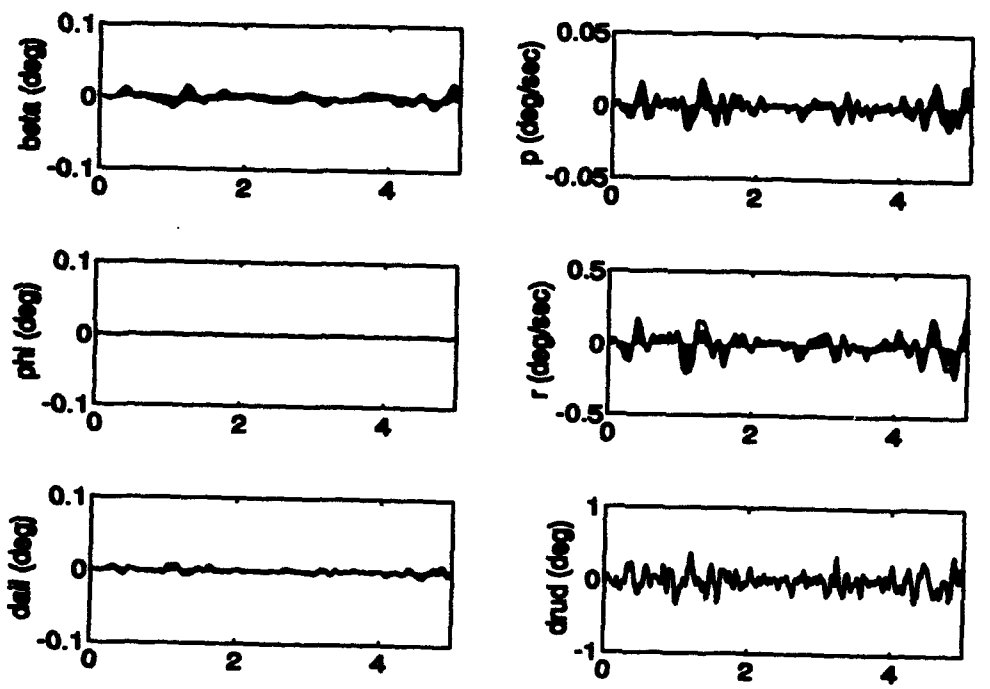

VI. Autopilot Design

This chapter presents an autopilot design for the Lambda. The autopilot is designed around the QFT p, β controller synthesized in the previous chapters. The designed QFT controller performs the functions of minimizing sideslip and stabilizing flight over a wide range of parameters. While roll rate is an excellent state to design a QFT controller around, it is desired to allow the pilot to command a desired bank angle. The commanded bank angle determines how tight a turn the aircraft will make.

The autopilot is a very simple design. It simply integrates the output of the roll gyro to yield the bank angle ϕ. This design is therefore limited by the saturation rates of the roll gyro, $\pm 40 \frac{deg}{sec}$. The bank angle calculated by the integrator is compared to a reference bank angle input by the pilot to determine the reference error. The pilot also commands a pitch rate to initiate the banked turn. The pitch rate and sideslip angle commands are input directly to the QFT controller.

Figure 6.1 shows the *Simulink* model used to simulate the autopilot. Both the longitudinal and lateral channels are simulated simultaneously to see the effect of damaged elevator deflections on the lateral channel. The model includes the discretized controllers and prefilters, continuous actuator and plant models, and all nonlinear elements. The thirteen lateral flight conditions are used since they contain the most drastic elevator damage. These conditions best analyze the rejection of elevator damage coupling into the lateral channel.

The first simulation shows the effect of damaged elevator deflections on the lateral channel. The elevator gradually increases its deflection. It is seen that for all plants the QFT controller and autopilot eliminate motion in the lateral channel in response to damaged elevator deflections while

Figure 6.1 Autopilot Simulink Model

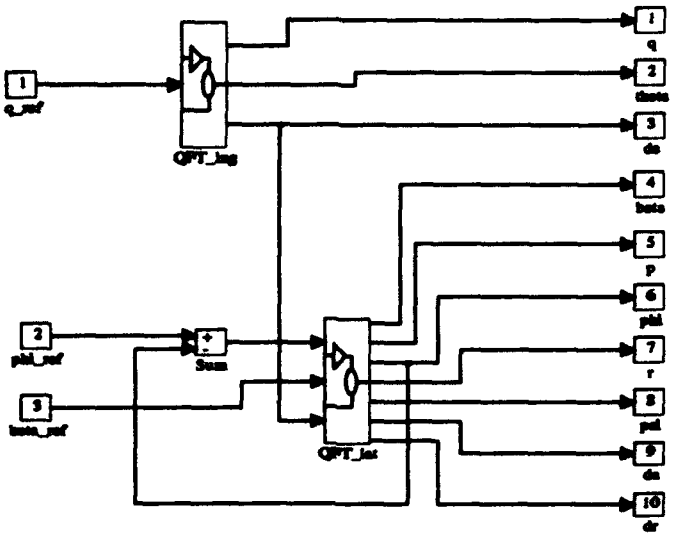

maintaining the commanded pitch rate. Lateral moments generated by the elevator are countered by the aileron and rudder.

The second simulation, Fig. 6.3, shows the aircraft response to a 45° roll command. The aileron-rudder interconnect in the QFT controller maintains adequate turn coordination. The peak value of β is about 3°. However, the turn coordinator quickly returns β to 0°. The maximum β excursions occur for the simulation performed at the slowest speed, maximum altitude and maximum damage conditions, as expected. This is precisely the flight condition with the least control authority . However, the exhibited control is still adequate. The desired roll angle is achieved rapidly and precisely for all flight and damage conditions.

Figure 6.4 shows the aircraft response to a roll doublet maneuver. A 10° doublet of 2 second duration (each pulse) is commanded. The roll channel is seen to respond in a smooth and coordinated manner. Note the rudder response as it maintains coordination.

The next simulation, Fig. 6.5, applies a $10\frac{deg}{sec}$ pitch rate reference to the system. All flight conditions have a lateral channel response since the flight conditions used always assume a 50% elevator damage. Turn coordination is maintained with minimal lateral control surface deflection. As shown in Chapter IV, the commanded pitch rate is not maintained when the elevator saturates. Saturation occurs more quickly than in previous simulations. During actual flight the pilot can minimize the loss of pitch rate by applying throttle commands to maintain airspeed.

A $10\frac{deg}{sec}$ pitch doublet of 2 second duration (each pulse) is now commanded. Figure 6.6 shows the response. Pitch rate tracks the reference adequately until the elevator saturates. The aileron and rudder are seen to maintain lateral coordination.

Although rudder control is not intended to be the primary control method, rudder inputs are simulated. Figure 6.7 shows the aircraft response to a 5° sideslip command. This amounts to placing the aircraft into a flat turn. The desired sideslip angle is maintained. Notice the aileron response as it holds the wings at a level condition.

Finally, a 5° sideslip doublet is commanded as shown in Fig. 6.8. The aircraft is seen to adequately track the commanded reference signal.

Figure 6.2 Autopilot Response to Elevator Deflection

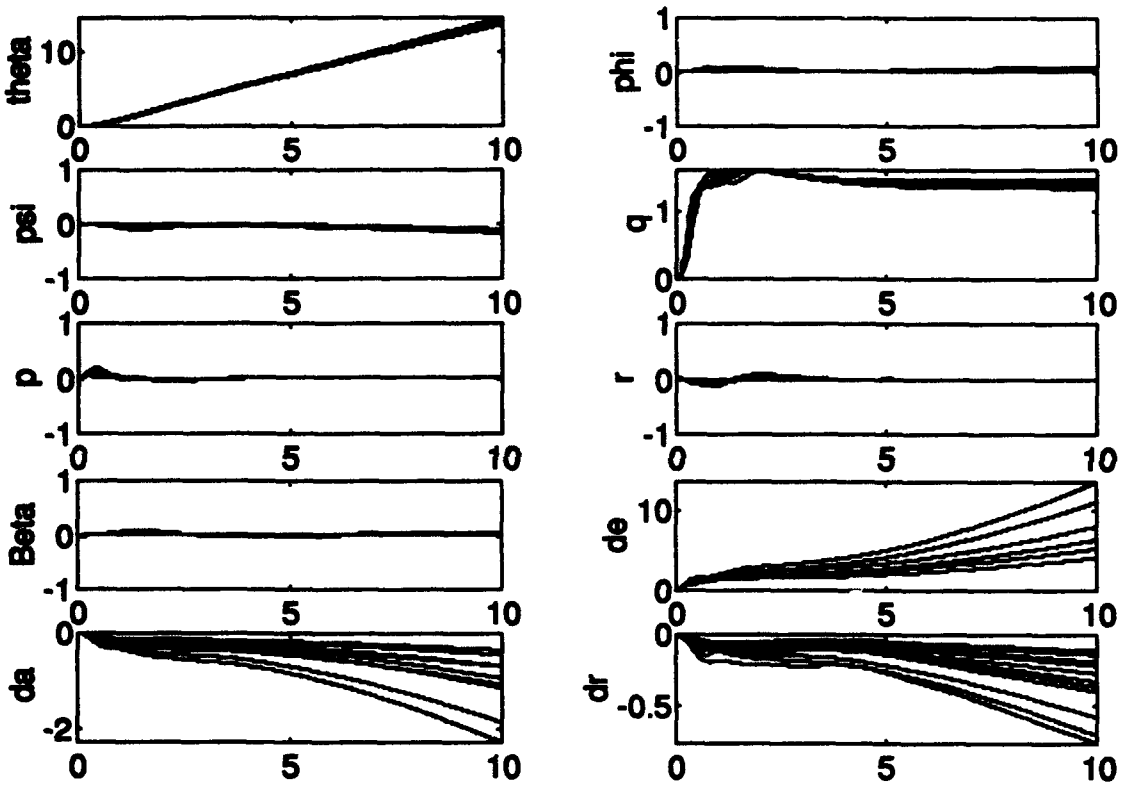

Figure 6.3 Autopilot Response to 45° Roll Command

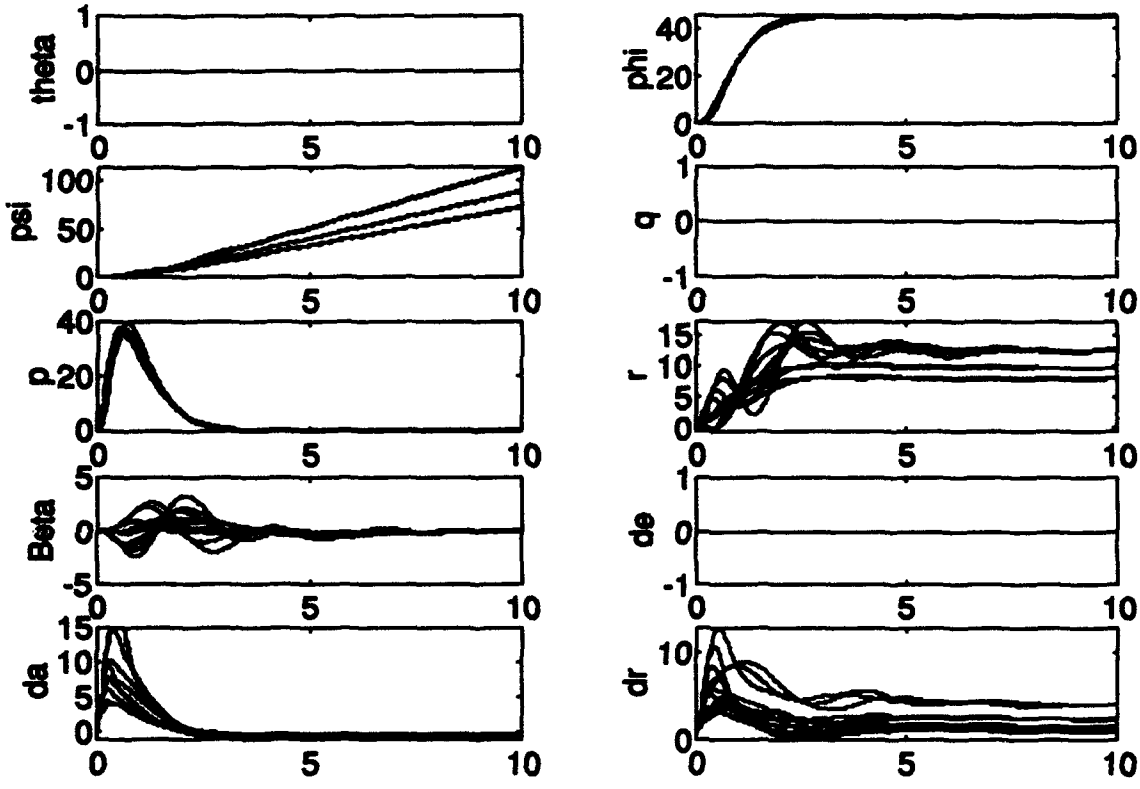

Figure 6.4 Autopilot Response to 10° 2 Second Pulse Roll Doublet

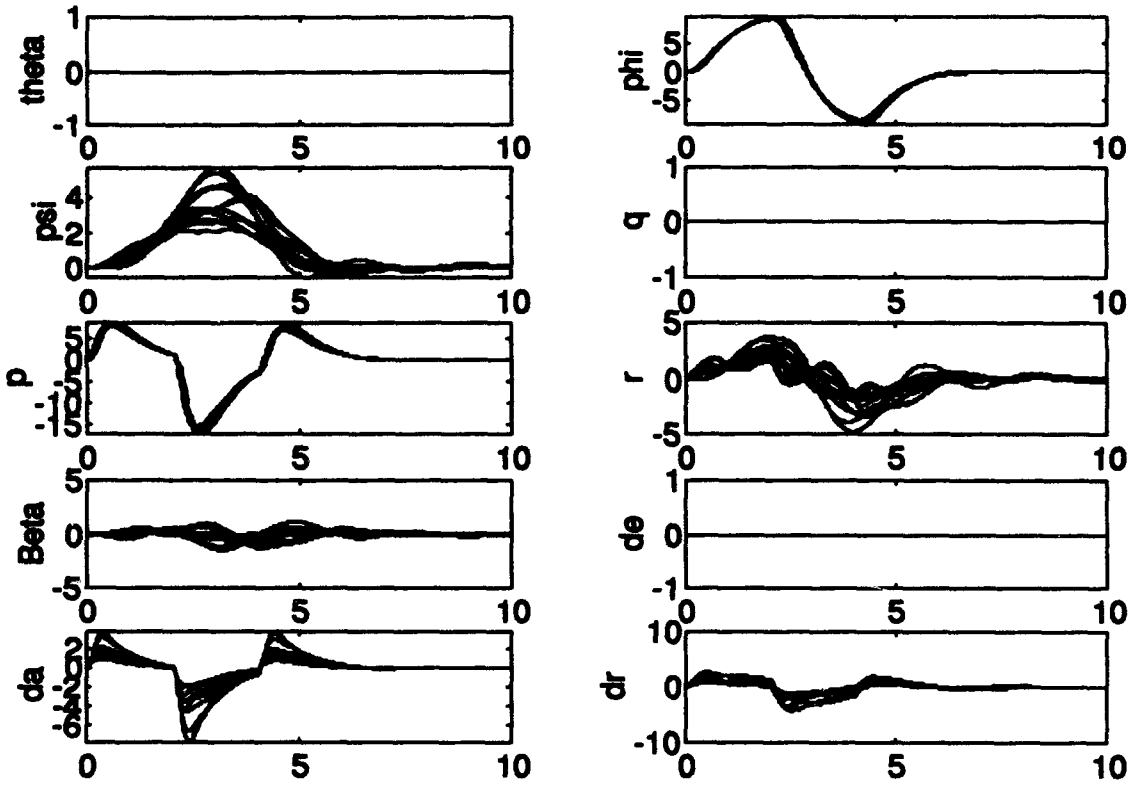

Figure 6.5 Autopilot Response to 10° Pitch Rate Command

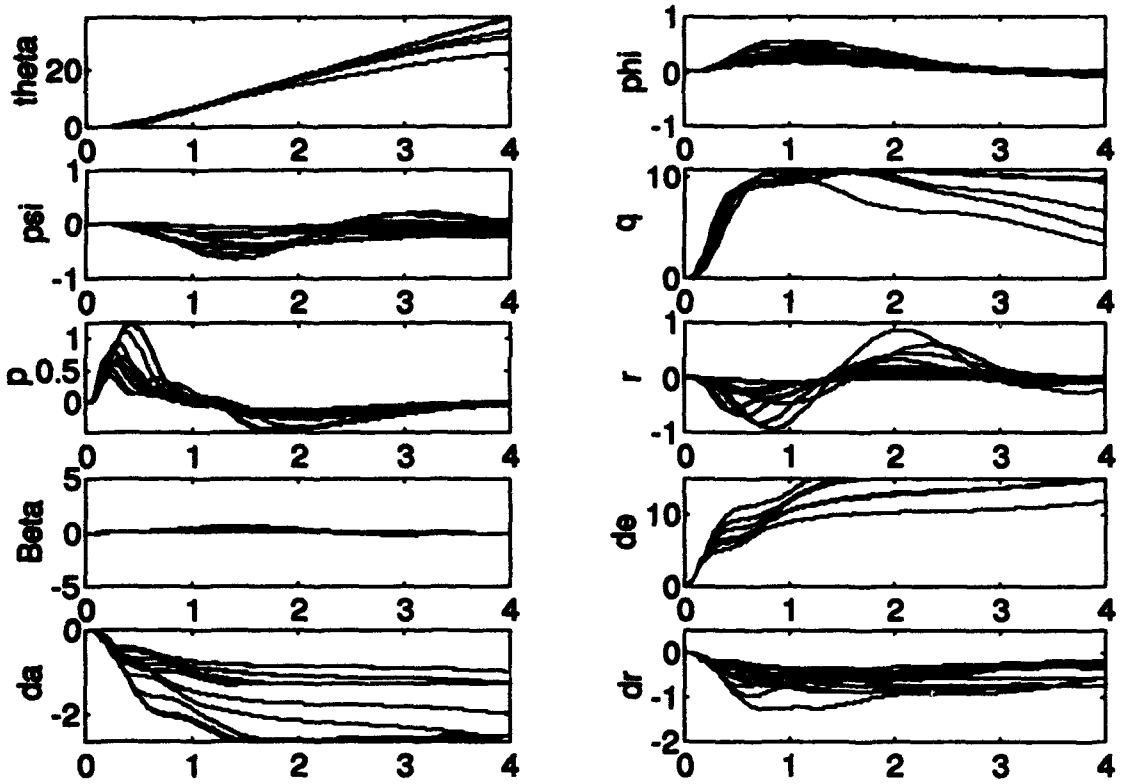

Figure 6.6 Autopilot Response to 10° 2 Second Pulse Pitch Doublet

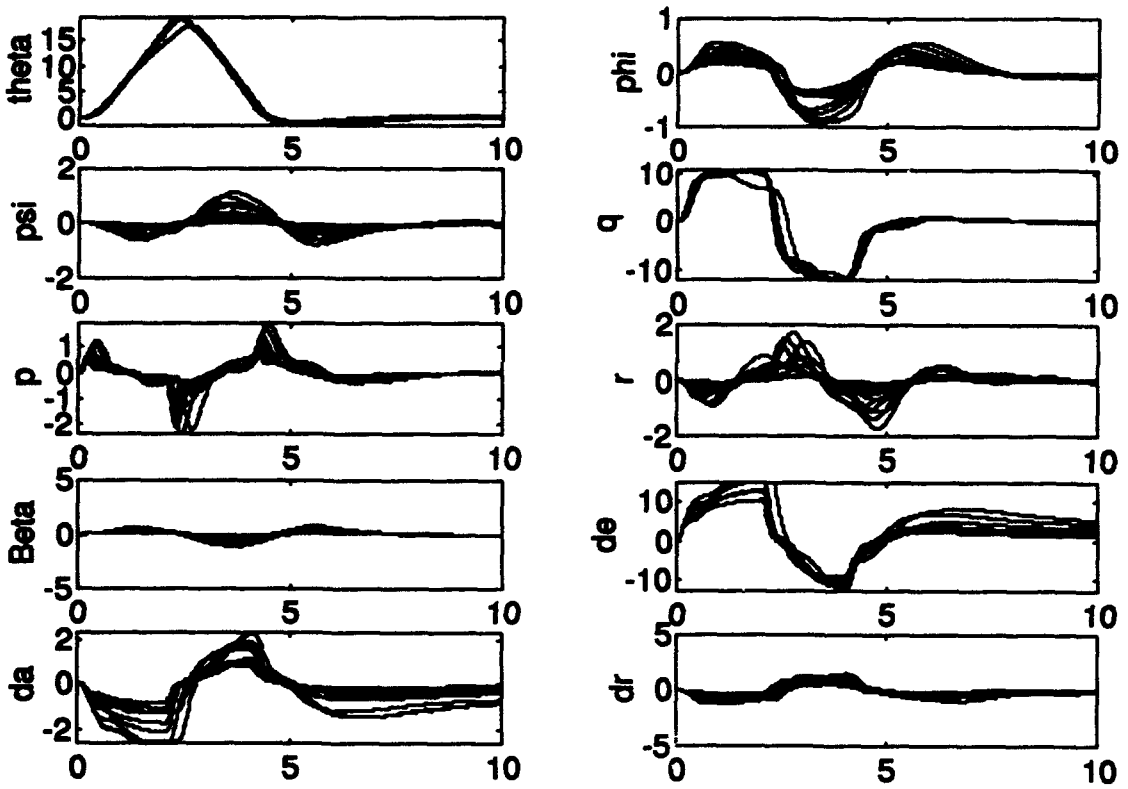

Figure 6.7 Autopilot Response to 5° Sideslip Command

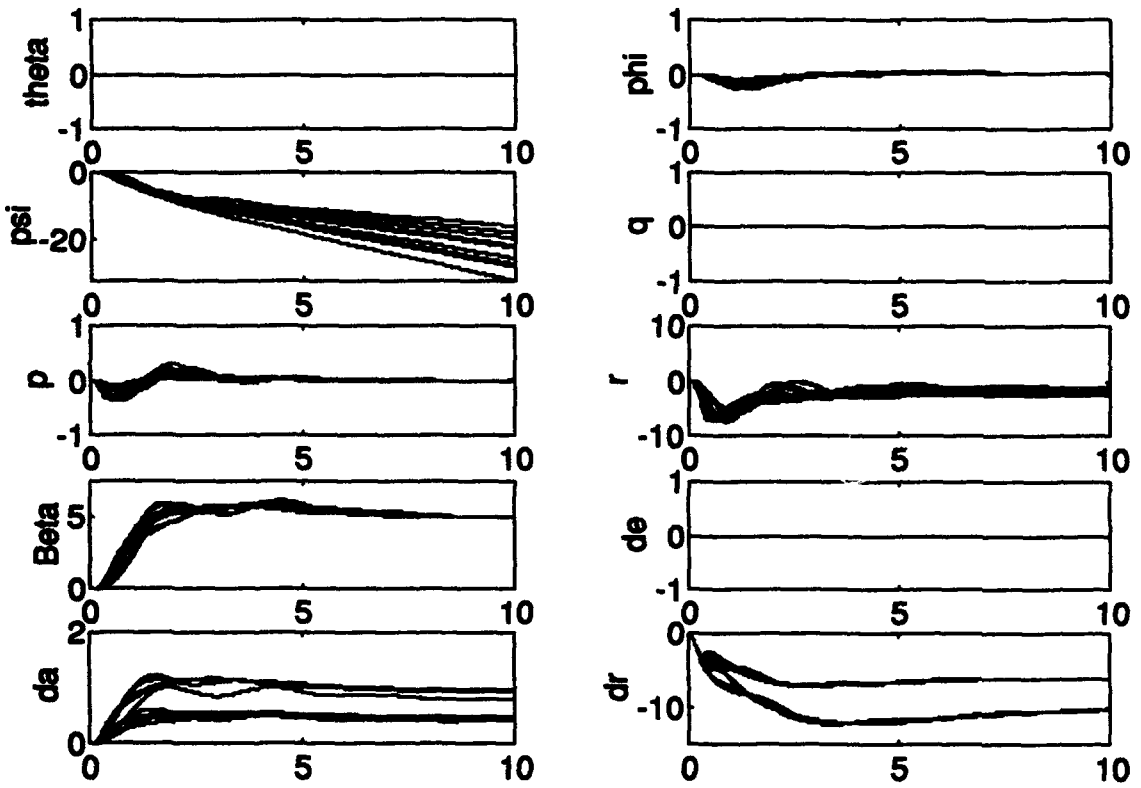

Figure 6.8 Autopilot Response to 10° 2 Second Pulse Sideslip Doublet

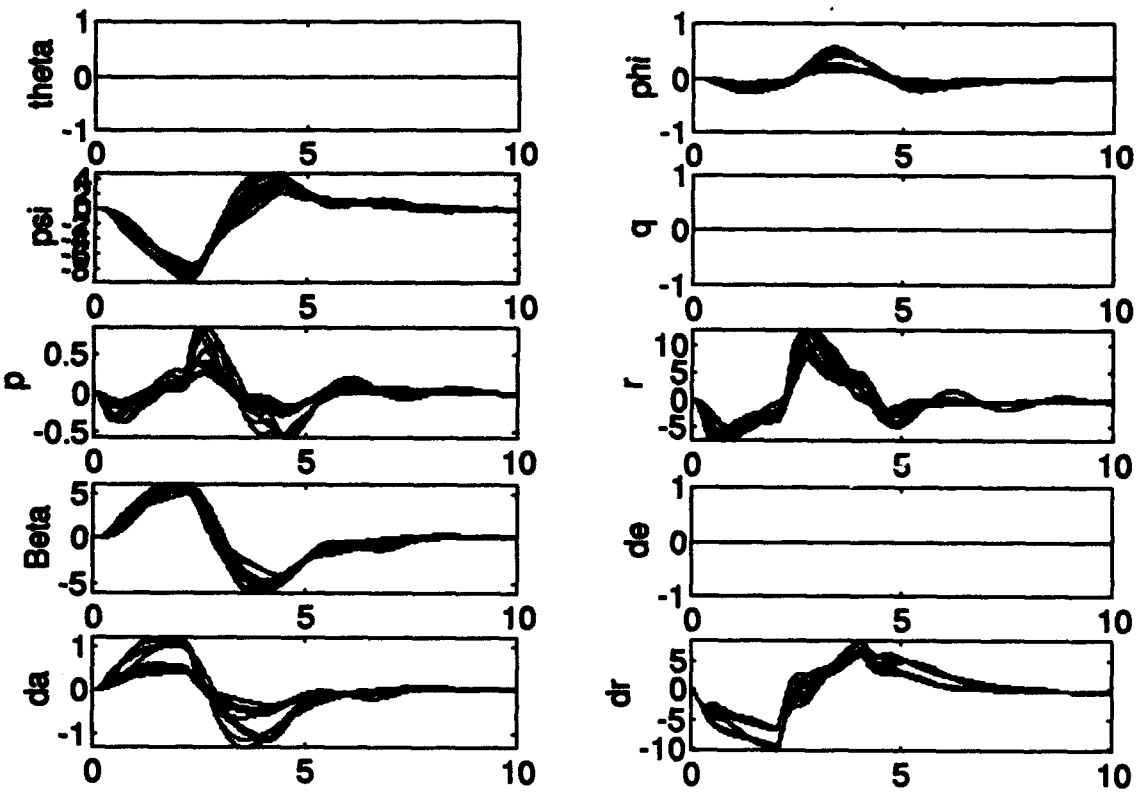

VII. Summary, Conclusions and Recommendations

This chapter presents a summary of the thesis, draws conclusions, and recommends future research.

7.1 Summary

The Quantitative Feedback Theory design technique is applied to the Lambda URV to synthesize a robust flight control system. This design expands on previous Lambda flight control system designs in that it considers actuator failures as a source of structured plant uncertainty. Failures considered are losses of surface area inflicted on the elevators, ailerons and rudders. Mathematical models of the failure's effects on the dynamics are derived and added to an existing macro which generates state-space models of the Lambda for given flight conditions. Failures manifest themselves as changes in stability derivatives and as external disturbances in both the longitudinal and lateral channels. The longitudinal channel design thus requires a MISO controls design with one feedback variable. The lateral channel entails a MIMO design consisting of two feedback states. Finally, an outer-loop autopilot is designed around the QFT controller.

The longitudinal MISO QFT design begins with the selection of flight conditions which adequately represent the Lambda flight envelope. Sixteen flight conditions are chosen. The short-period approximation of longitudinal aircraft dynamics is utilized. The PCT design technique is employed for a digital sampling rate of 50Hz.

In the pitch channel, a fifth-order controller and third order prefilter are synthesized which employ the feedback state (pitch rate) to adequately meet frequency domain stability and tracking specifications in the face of varying flight conditions and elevator failure. The controllers are

transformed to the z-plane via a Tustin transformation. The digital design is simulated with *Simulink*. Analyses of the possibility of P.I.O.s and sensor noise effects are then performed.

The lateral MIMO QFT design proceeds in a similar manner. Thirteen flight conditions are chosen. A PCT design is performed around two feedback states, roll-rate and sideslip angle. Sideslip angle is chosen as a feedback state so the resultant QFT controller, which in a natural way renders a degree of decoupling, coordinates aircraft flight. To aid coordination, an aileron-rudder interconnect is employed via a control weighting matrix. An equivalent $m \times m$ MISO loop transfer function matrix **Q** is developed which results in a fifth-order roll channel controller and a second-order prefilter. Modified yaw channel **Q**'s are formed using QFT's Method Two. In addition, a fifth-order yaw controller and a third-order prefilter which adequately meet frequency domain specifications are synthesized. Digital simulations of roll and yaw channel disturbance responses are performed with *Simulink*. Analyses of lateral channel P.I.O.s and sensor noise effects are performed.

An outer-loop autopilot is formed around the QFT controller. The autopilot integrates roll rate to obtain roll angle. Roll angle is then fed back to the pilot reference command. The remote pilot can then perform a banked turn by simply commanding a reference bank angle and a pitch rate. No rudder control is necessary since the QFT controller induces the turn by eliminating sideslip. The autopilot is simulated with *Simulink*. The *Simulink* model includes cross-coupling of the longitudinal channel into the lateral channel as derived for elevator failures. Seven different commanded inputs are simulated.

7.2 Conclusions

Several conclusions are reached about this specific design and the QFT method in general:

- A robust digital controller and prefilter are designed for the longitudinal channel which meet frequency domain specifications for a loss of elevator surface area up to 25%. Reasonable aircraft control can be maintained for up to 50% elevator loss but response specifications are no longer met. Greater damage levels cannot be adequately accommodated due to the inherently large bandwidth of the longitudinal channel. The controller quickly returns the aircraft to a trimmed flight condition after surface area lo The designed controller minimizes effects of pitch rate sensor noise on the time responses.
- Robust digital controllers and prefilters are designed for the lateral channel. The resulting controllers and prefilters adequately meet specifications for 50% surface area loses in both the aileron and rudder. The controllers reject cross-coupling of the longitudinal channel into the lateral channel in the face of elevator damage. The controllers and aileron-rudder interconnect successfully limit sideslip induced by an aircraft roll. Tracking specifications are slightly violated because of controller gain limitations caused by sensor noise.
- An autopilot is designed which enables coordinated flight for the Lambda URV under serious damage conditions. The QFT controller and the autopilot allow the Lambda to be flown in a "feet-on-the-floor" manner. That is, banked turns require only a roll angle command and a pitch rate command. Autopilot performance is limited by the aerodynamic properties of the aircraft itself and by limits on the gyro feedback rates.
- Aerodynamic surface failures cause significant gain and phase losses in the aircraft response. Therefore, for responses to meet specifications, the controller must contain significant gain

and phase lead. Noise and sampling effects limit the ability of the controllers to have these characteristics. Noise limits the amount of gain which may be placed in the controllers. This is especially a concern when using a state such as β whose sensor is characteristically noisy. Sampling rate limits the bandwidth of the controller which may be used. More drastic failures can be accommodated using a QFT controller if sensor noise is decreased and/or a faster sampling rate is used.

- Control surface failures can be successfully included as structured parameter uncertainties in a QFT flight control design. QFT robustly compensates for limited control surface failures to maintain a desired aircraft response. The robust control is accomplished with a fixed, not a scheduled, controller, thus maintaining controller simplicity. The utility of QFT is evident throughout the design. Its effective use of the frequency domain along with the associated MIMO QFT CAD Package allows quick insight into the flight control problem when design trade-offs need to be made.
- The AFIT MIMO QFT CAD Package is invaluable in the completion of this and any QFT design. Without its ease of use, many aspects of this design problem could not have been investigated as effectively or as efficiently as they were.

7.3 Recommendations

The following recommendations are made based upon the results of this thesis:

- Future study should investigate the improvement of the aileron-rudder interconnect by using dynamic terms in the weighting matrix. Better rejection of sideslip in response to an aileron

input can be achieved with a dynamic matrix. Improved sideslip rejection will in turn improve coordinated flight efforts.

- Greater control in the longitudinal channel can be achieved if flaperons are used for dynamic control. Now that a failure model is generated, a weighting matrix can be employed to share control efforts between the elevator/flaperon and aileron/flaperon surfaces. Differential surface control can also be investigated for damaged flight control.
- Investigate coordinating damage control efforts between a QFT flight control system and a multiple model adaptive estimator.
- Apply QFT to design a flight control system for a high performance Air Force aircraft with control surface failures.
- Modify MIMO QFT CAD Package to allow greater freedom when generating plots. In particular, options allowing the placement of labels and custom text on plots should be included.

Appendix A. Modified Model Generation Macro

The following *Matlab* executable file was created by Lt Gerald Swift and modified by Capt Steve Rasmussen. It was further modified to account for changes in stability derivatives due to control surface damage.

```
%   This macro calculates the longitudinal and lateral-
%   directional state space equations of motion for the
%   Lambda URV given Xcg, U1, q1, W and theta.
%
%   Input:  X=[Xcg,U1,q1,W,theta,ztae,ztar,ztaa]
%
%           where, Xcg = inches
%                  U1 = feet/second
%                  q1 = pounds/sq foot
%                  W  = pounds
%                  theta = degrees
%                  ztae = elevator damage (1 to 0; 1= no damage)
%                  ztar = rudder damage (1 to 0)
%                  ztaa = aileron damage (1 to 0)
%
%   Outputs:
%
%     Clong=[CMu,CMa,CMad,CMq,CLu,CLa,CLad,CLq,CDa,CDu,
%                              CLde,CDde,CMde,CLdf,CDdf,CMdf]'
%
%     Clat=[Clb,Clp,Clr,Clda,Cldr,Cnb,Cnp,Cnr,Cnda,Cndr,
%                                     Cyb,Cyp,Cyr,Cyda,Cydr]'
%
%     Dlong = corresponding vector of dimensional derivatives for Clong
%
%     Dlat = corresponding vector of dimensional derivatives for Clat
%
%     Along = A matrix for longitudinal equations of motion
%
%     Alat = A matrix for lateral-directional equations of motion
%
%     Blong = B matrix for longitudinal equations of motion
%
%     Blat = B matrix for lateral-directional equations of motion
```

```
%
xcg=x(1,1);
u=x(1,2);
q=x(1,3);
m=x(1,4)/32.174;
ztae=x(1,6);                % added, msk
ztar=x(1,7);                % added. msk
ztaa=x(1,8);                % added, msk
St=5.17;                    % added, msk
Sw=21.1;                    % added, msk
nu=.95;                     % added, msk
k=0.42;                     % added, msk
At=2.8645;                  % added, msk
Aw=4.55;                    % added, msk
dxcg=(46.405-xcg)/12;       % added, msk
lt=(101.99-xcg)/12;         % added, msk
s=21.1;
c=1.51;
b=14.07;
Ixx=32.502;
Iyy=26.666;
Izz=40.939;
Ixz=0.5922;
CL1=x(1,4)/(q*s);
CD1=0.027;
CM1=0.0;
A1=Ixz/Ixx;
B1=Ixz/Izz;
ztaar = ((ztaa-1)*1.4 + (ztar-1)*1.0 + 24.6)/24.6;  % added, msk
ztarprm = ((ztar-1)*1.0 + 3.5)/3.5;                 % added, msk
ztaeprm = ((ztae-1)*1.4 + 5.17)/5.17;               % added, msk
nma = (1-ztaeprm)*nu*St*At*lt*(1-k);                % added, msk
dma = Sw*Aw*dxcg + ztaeprm*nu*St*At*lt*(1-k);       % added, msk
dmama = nma/dma;                                    % added, msk
nza = (1-ztaeprm)*nu*St*At*(1-k);                   % added, msk
dza = Sw*Aw + ztaeprm*nu*St*At*(1-k);               % added, msk
dzaza = nza/dza;                                    % added, msk
%
%  The following parameters represent changes to
%  Swifts' model based on 20 nov 92 flight test - sjr
%
CMAV=0.75;
CMADV=0.7;
CMQV=0.6;
CMDEV=-0.5;
```

```
CLDAV=0.75;
CNBV=0.9;
CNRV=0.9;
CNDRV=-0.6;
%
%  end new parameters - sjr
%
CMu=0;
CMa=CMAV*(0.326643*x(1,1)-16.5189);       %  changed, sjr
CMad=CMADV*(0.238235*x(1,1)-7.8977);      %  changed, sjr
CMq=CMQV*(0.628420*x(1,1)-45.0582);       %  changed, sjr
CLu=-0.0001719*x(1,1)+0.01518;
CLa=5.820;
CLad=-0.03838*x(1,1)+3.83508;
CLq=-0.65202*x(1,1)+37.8884;
CDa=0;
CDu=0;
CLde=0.2908;
CDde=0;
CMde=CMDEV*(0.013464*x(1,1)-1.48039); %  changed, sjr
CLdf=1.419;
CDdf=0.08489;
CMdf=0.070932*x(1,1)-3.63838;
Clong1=[CMu,CMa,CMad,CMq,CLu,CLa,CLad,CLq,CDa,CDu];
Clong2=[CLde,CDde,CMde,CLdf,CDdf,CMdf];
Clong=[Clong1 Clong2]';
%
Clb=-0.01451;
Clp=-.5538;
Clr=0.08763;
Clda=CLDAV*0.2608;                        %  changed, msk
Cldr=0.000213*x(1,1)-0.00783;
Cnb=CNBV*(-0.00038*x(1,1)+0.07834);       %  changed, sjr
Cnp=-0.03601;
Cnr=CNRV*(0.003087*x(1,1)-0.31072);       %  changed, sjr
Cnda=-0.01368;
Cndr=CNDRV*(0.001633*x(1,1)-0.15208); %  updated 4/22/91, changed, sjr
Cyb=-0.4372;
Cyp=-0.001600;
Cyr=-0.00424*x(1,1)+0.46047;
Cyda=0;
Cydr=0.2865;
Clat=[Clb,Clp,Clr,Clda,Cldr,Cnb,Cnp,Cnr,Cnda,Cndr,Cyb,Cyp,Cyr,Cyda,Cydr]';
%
%
```

```
%   Calculation of Dimensional Derivatives
%
%     Dlong=[Mu,Ma,Mad,Mq,Zu,Za,Zad,Zq,Xa,Xu,Zde,Xde,Mde,Zdf,Xdf,Mdf]'
%
%     Dlat=[Lb,Lp,Lr,Lda,Ldr,Nb,Np,Nr,Nda,Ndr,Yb,Yp,Yr,Yda,Ydr]'
%
%
Mu=q*s*c*(CMu+2*CM1)/(Iyy*u);
Ma=q*s*c*(CMa-(CMa*dmama))/Iyy;          % changed, msk
Mad=q*s*c*c*CMad/(2*Iyy*u);
Mq=q*s*c*c*ztaeprm*CMq/(2*Iyy*u);        % changed, msk
Zu=-q*s*(CLu+2*CL1)/(m*u);
Za=-q*s*((CLa+CD1)-((CLa+CD1)*dzaza))/m; % changed, msk
Zad=-q*s*c*CLad/(2*m*u);
Zq=-q*s*c*ztaeprm*CLq/(2*m*u);           % changed, msk
Xu=-q*s*(CDu+2*CD1)/(m*u);
Xa=-q*s*(CDa-CL1)/m;
Zde=-q*s*ztae*CLde/m;                    % changed, msk
Xde=-q*s*CDde/m;
Mde=q*s*c*ztae*CMde/Iyy;                 % changed, msk
Zdf=-q*s*CLdf/m;
Xdf=-q*s*CDdf/m;
Mdf=q*s*c*CMdf/Iyy;
Dlong=[Mu,Ma,Mad,Mq,Zu,Za,Zad,Zq,Xa,Xu,Zde,Xde,Mde,Zdf,Xdf,Mdf]';
%
Lb=q*s*b*ztarprm*Clb/Ixx;
Lp=q*s*b*b*ztaar*Clp/(2*Ixx*u);           % changed, msk
Lr=q*s*b*b*ztarprm*Clr/(2*Ixx*u);         % changed, msk
Lda=q*s*b*ztaa*Clda/Ixx;                  % changed, msk
Ldr=q*s*b*ztar*Cldr/Ixx;                  % changed, msk
Nb=q*s*b*ztarprm*Cnb/Izz;                 % changed, msk
Np=q*s*b*b*ztarprm*Cnp/(2*Izz*u);         % changed, msk
Nr=q*s*b*b*ztarprm*Cnr/(2*Izz*u);         % changed, msk
Nda=q*s*b*ztaa*Cnda/Izz;                  % changed, msk
Ndr=q*s*b*ztar*Cndr/Izz;                  % changed, msk
Yb=q*s*ztarprm*Cyb/m;                     % changed, msk
Yp=q*s*b*ztarprm*Cyp/(2*m*u);             % changed, msk
Yr=q*s*b*ztarprm*Cyr/(2*m*u);             % changed, msk
Yda=q*s*ztaa*Cyda/m;                      % changed, msk
Ydr=q*s*ztar*Cydr/m;                      % changed, msk
Dlat=[Lb,Lp,Lr,Lda,Ldr,Nb,Np,Nr,Nda,Ndr,Yb,Yp,Yr,Yda,Ydr]';
%
%   Calculation of the Longitudinal A and B matrices
%
theta=x(1,5)/57.29578;
```

```
Along=[Xu,Xa,0,-32.174*cos(theta);
       Zu/(u-Zad),Za/(u-Zad),(u+Zq)/(u-Zad),-32.174*sin(theta);
       Mu+Mad*Zu/(u-Zad),Ma+Mad*Za/(u-Zad),Mq+Mad*(u+Zq)/(u-Zad),...
      -Mad*32.174*sin(theta);
       0,0,1,0];
Blong=[Xde;                                  % flaps deleted, msk
       Zde/(u-Zad);
       Mde+Mad*Zde/(u-Zad);
       0];
%
%   Calculation of the Lateral Directional A and B matrices
%
BA=1-B1*A1;
Alat=[Yb/u,Yp/u,32.174*cos(theta)/u,Yr/u-1;        % psi state deleted, msk
      (Lb+A1*Nb)/BA,(Lp+A1*Np)/BA,0,(Lr+A1*Nr)/BA;
      0,1,0,0;
      (Nb+B1*Lb)/BA,(Np+B1*Lp)/BA,0,(Nr+B1*Lr)/BA];
Blat=[Yda/u,Ydr/u;                                 % psi state deleted, msk
      (Lda+A1*Nda)/BA,(Ldr+A1*Ndr)/BA;
      0,0;
      (Nda+B1*Lda)/BA,(Ndr+B1*Ldr)/BA];
%
%   Generate B matrices for the lateral and longitudinal disturbances
%
blngdist = ((1-ztae)/ztae)*Blong;
%
Ldauf = q*s*b*Clda/Ixx;
blatdist = [0;((1-ztae)*Ldauf)/(6*BA);0;(B1*(1-ztae)*Ldauf)/(6*BA)];
```

Appendix B. Flight Conditions

This appendix displays the flight conditions prior to template generation for both the longitudinal and lateral channels.

B.1 Longitudinal Conditions

Table B.1 Initial Longitudinal Flight Conditions

#	*cg* (*in*)	*Speed* (*ft/sec*)	Q_∞ (lbs/ft^2)	*Weight* (*lbs*)	ζ_e
1	45.83	118.23	16.13	190	1
2	45.83	118.23	16.13	215	1
3	45.83	118.23	12.27	190	1
4	45.83	118.23	12.27	215	1
5	45.83	185.79	39.83	190	1
6	45.83	185.79	39.83	215	1
7	45.83	185.79	30.31	190	1
8	45.83	185.79	30.31	215	1
9	47.75	118.23	16.13	190	1
10	47.75	118.23	16.13	215	1
11	47.75	118.23	12.27	190	1
12	47.75	118.23	12.27	215	1
13	47.75	185.79	39.83	190	1
14	47.75	185.79	39.83	215	1
15	47.75	185.79	30.31	190	1
16	47.75	185.79	30.31	215	1
17	45.83	118.23	16.13	190	0.75
18	45.83	118.23	16.13	215	0.75
19	45.83	118.23	12.27	190	0.75
20	45.83	118.23	12.27	215	0.75
21	45.83	185.79	39.83	190	0.75
22	45.83	185.79	39.83	215	0.75
23	45.83	185.79	30.31	190	0.75
24	45.83	185.79	30.31	215	0.75
25	47.75	118.23	16.13	190	0.75
26	47.75	118.23	16.13	215	0.75
27	47.75	118.23	12.27	190	0.75
28	47.75	118.23	12.27	215	0.75
29	47.75	185.79	39.83	190	0.75
30	47.75	185.79	39.83	215	0.75
31	47.75	185.79	30.31	190	0.75
32	47.75	185.79	30.31	215	0.75

B.2 Lateral Conditions

Table B.2 Initial Lateral Flight Conditions

#	*cg* (*in*)	*Speed* (ft/sec)	Q_∞ (lbs/ft^2)	*Weight* (*lbs*)	ζ_e	ζ_r	ζ_a
1	46.79	118.23	16.13	202.5	0.5	1	1
2	46.79	118.23	16.13	202.5	0.5	1	0.5
3	46.79	118.23	16.13	202.5	0.5	0.5	1
4	46.79	118.23	16.13	202.5	0.5	0.5	0.5
5	46.79	118.23	12.27	202.5	0.5	1	1
6	46.79	118.23	12.27	202.5	0.5	1	0.5
7	46.79	118.23	12.27	202.5	0.5	0.5	1
8	46.79	118.23	12.27	202.5	0.5	0.5	0.5
9	46.79	185.79	39.83	202.5	0.5	1	1
10	46.79	185.79	39.83	202.5	0.5	1	0.5
11	46.79	185.79	39.83	202.5	0.5	0.5	1
12	46.79	185.79	39.83	202.5	0.5	0.5	0.5
13	46.79	185.79	30.31	202.5	0.5	1	1
14	46.79	185.79	30.31	202.5	0.5	1	0.5
15	46.79	185.79	30.31	202.5	0.5	0.5	1
16	46.79	185.79	30.31	202.5	0.5	0.5	0.5

Appendix C. Longitudinal Plant Transfer Functions

This appendix lists the effective plant transfer functions $\frac{q(s)}{\delta_e(s)}$ and the disturbance transfer functions $\frac{q(s)}{d(s)}$ for the longitudinal channel.

C.1 Longitudinal $P_e(s)$ Short-Period Transfer Functions

Plant 1:

$$\frac{q(s)}{\delta_e(s)} = \frac{85958.1000(s+2.1700)}{(s+1.3139 \pm j4.0857)(s+10.8140 \pm j7.7387)(s+100)}$$

Plant 2:

$$\frac{q(s)}{\delta_e(s)} = \frac{278729.4455(s+4.4800)}{(s+2.7124 \pm j7.3369)(s+10.8140 \pm j7.7387)(s+100)}$$

Plant 3:

$$\frac{q(s)}{\delta_e(s)} = \frac{212263.8319(s+3.4100)}{(s+2.0647 \pm j6.4204)(s+10.8140 \pm j7.7387)(s+100)}$$

Plant 4:

$$\frac{q(s)}{\delta_e(s)} = \frac{109347.4836(s+3.0814)}{(s+1.8263 \pm j3.5743)(s+10.8140 \pm j7.7387)(s+100)}$$

Plant 5:

$$\frac{q(s)}{\delta_e(s)} = \frac{83337.7877(s+2.0725)}{(s+1.2652 \pm j3.1567)(s+10.8140 \pm j7.7387)(s+100)}$$

Plant 6:

$$\frac{q(s)}{\delta_e(s)} = \frac{270021.2398(s+4.8422)}{(s+2.8699 \pm j5.6167)(s+10.8140 \pm j7.7387)(s+100)}$$

Plant 7:

$$\frac{q(s)}{\delta_e(s)} = \frac{270185.4425(s+4.2796)}{(s+2.6118 \pm j5.6715)(s+10.8140 \pm j7.7387)(s+100)}$$

Plant 8:

$$\frac{q(s)}{\delta_e(s)} = \frac{205793.2696(s+3.2568)}{(s+1.9881 \pm j4.9606)(s+10.8140 \pm j7.7387)(s+100)}$$

Plant 9:

$$\frac{q(s)}{\delta_e(s)} = \frac{84612.1689(s+3.1857)}{(s+1.8419 \pm j4.4824)(s+10.8140 \pm j7.7387)(s+100)}$$

Plant 10:

$$\frac{q(s)}{\delta_e(s)} = \frac{64468.5757(s+2.1433)}{(s+1.2778 \pm j3.9504)(s+10.8140 \pm j7.7387)(s+100)}$$

Plant 11:

$$\frac{q(s)}{\delta_e(s)} = \frac{209047.0876(s+4.4250)}{(s+2.6377 \pm j7.0929)(s+10.8140 \pm j7.7387)(s+100)}$$

Plant 12:

$$\frac{q(s)}{\delta_e(s)} = \frac{159197.8739(s+3.3681)}{(s+2.0079 \pm j6.2078)(s+10.8140 \pm j7.7387)(s+100)}$$

Plant 13:

$$\frac{q(s)}{\delta_e(s)} = \frac{82010.6127(s+3.0415)}{(s+1.7809 \pm j3.3700)(s+10.8140 \pm j7.7387)(s+100)}$$

Plant 14:

$$\frac{q(s)}{\delta_e(s)} = \frac{62474.3925(s+2.1700)}{(s+1.3559 \pm j2.9567)(s+10.8140 \pm j7.7387)(s+100)}$$

Plant 15:

$$\frac{q(s)}{\delta_e(s)} = \frac{202515.9298(s+4.7795)}{(s+2.7986 \pm j5.2958)(s+10.8140 \pm j7.7387)(s+100)}$$

Plant 16:

$$\frac{q(s)}{\delta_e(s)} = \frac{137680.4259(s+3.0148)}{(s+1.7875 \pm j4.0287)(s+10.8140 \pm j7.7387)(s+100)}$$

C.2 Longitudinal $P_d(s)$ Short-Period Transfer Functions

Plant 1:

$$\frac{q(s)}{d(s)} = 0$$

Plant 2:

$$\frac{q(s)}{d(s)} = 0$$

Plant 3:

$$\frac{q(s)}{d(s)} = 0$$

Plant 4:

$$\frac{q(s)}{d(s)} = 0$$

Plant 5:

$$\frac{q(s)}{d(s)} = 0$$

Plant 6:

$$\frac{q(s)}{d(s)} = 0$$

Plant 7:

$$\frac{q(s)}{d(s)} = 0$$

Plant 8:

$$\frac{q(s)}{d(s)} = 0$$

Plant 9:

$$\frac{q(s)}{d(s)} = \frac{2.0708(s + 3.1857)}{(s + 1.8419 \pm j4.4824)}$$

Plant 10:

$$\frac{q(s)}{d(s)} = \frac{1.5778(s + 2.1433)}{(s + 1.2778 \pm j3.9504)}$$

Plant 11:

$$\frac{q(s)}{d(s)} = \frac{5.1162(s + 4.4250)}{(s + 2.6377 \pm j7.0929)}$$

Plant 12:

$$\frac{q(s)}{d(s)} = \frac{3.8962(s + 3.3681)}{(s + 2.0079 \pm j6.2078)}$$

Plant 13:

$$\frac{q(s)}{d(s)} = \frac{2.0071(s + 3.0415)}{(s + 1.7809 \pm j3.3700)}$$

Plant 14:

$$\frac{q(s)}{d(s)} = \frac{1.5290(s + 2.1700)}{(s + 1.3559 \pm j2.9567)}$$

Plant 15:

$$\frac{q(s)}{d(s)} = \frac{4.9563(s + 4.7795)}{(s + 2.7986 \pm j5.2958)}$$

Plant 16:

$$\frac{q(s)}{d(s)} = 0$$

Appendix D. Lateral Plant Transfer Functions

This appendix lists the effective plant transfer functions $P_{e_{11}}(s)$ and the disturbance transfer functions $P_{d_{11}}(s)$ for the lateral channel.

D.1 Transfer Function $\mathbf{P}_{e_{11}}(s) = \frac{p(s)}{\delta_a(s)}$

Plant 1:

$$\frac{p(s)}{\delta_a(s)} = \frac{160.79s(s+0.6633 \pm j2.5958)(s+4.4699)(s+1968.5371)}{(s-0.0226)(s+4.4372)(s+4.7342)(s+100)(s+0.6184 \pm j2.5351)(s+11.0737 \pm j10.0893)}$$

Plant 2:

$$\frac{p(s)}{\delta_a(s)} = \frac{80.39s(s+0.5265 \pm j2.3165)(s+4.4466)(s+7793.0854)}{(s-0.0193)(s+4.4372)(s+4.7718)(s+100)(s+0.5299 \pm j2.3482)(s+11.0737 \pm j10.0893)}$$

Plant 3:

$$\frac{p(s)}{\delta_a(s)} = \frac{122.33s(s+0.4805 \pm j2.2153)(s+4.4576)(s+3908.3631)}{(s-0.0219)(s+4.4372)(s+3.7251)(s+100)(s+0.4638 \pm j2.2221)(s+11.0737 \pm j10.0893)}$$

Plant 4:

$$\frac{p(s)}{\delta_a(s)} = \frac{122.33s(s+0.5062 \pm j2.2720)(s+4.4777)(s+1966.3849)}{(s-0.0225)(s+4.4372)(s+3.6224)(s+100)(s+0.4629 \pm j2.2231)(s+11.0737 \pm j10.0893)}$$

Plant 5:

$$\frac{p(s)}{\delta_a(s)} = \frac{61.17s(s+0.4009 \pm j2.0272)(s+4.4485)(s+7791.2275)}{(s-0.0193)(s+4.4372)(s+3.6473)(s+100)(s+0.3970 \pm j2.0586)(s+11.0737 \pm j10.0893)}$$

Plant 6:

$$\frac{p(s)}{\delta_a(s)} = \frac{61.17s(s+0.4121 \pm j2.0544)(s+4.4596)(s+3907.3803)}{(s-0.0198)(s+4.4372)(s+3.5443)(s+100)(s+0.3962 \pm j2.0595)(s+11.0737 \pm j10.0893)}$$

Plant 7:

$$\frac{p(s)}{\delta_a(s)} = \frac{397.05s(s+0.9717 \pm j3.9639)(s+4.4840)(s+3915.6867)}{(s-0.0142)(s+4.4372)(s+7.6264)(s+100)(s+0.9762 \pm j3.9567)(s+11.0737 \pm j10.0893)}$$

Plant 8:

$$\frac{p(s)}{\delta_a(s)} = \frac{397.05s(s+1.0049 \pm j4.0547)(s+4.5286)(s+1973.6692)}{(s-0.0146)(s+4.4372)(s+7.4112)(s+100)(s+0.9755 \pm j3.9582)(s+11.0737 \pm j10.0893)}$$

Plant 9:

$$\frac{p(s)}{\delta_a(s)} = \frac{198.52s(s+0.8191 \pm j3.6352)(s+4.4599)(s+7797.5219)}{(s-0.0125)(s+4.4372)(s+7.4753)(s+100)(s+0.8353 \pm j3.6669)(s+11.0737 \pm j10.0893)}$$

Plant 10:

$$\frac{p(s)}{\delta_a(s)} = \frac{302.09s(s+0.7404 \pm j3.4732)(s+4.4808)(s+3912.2895)}{(s-0.0142)(s+4.4372)(s+5.8217)(s+100)(s+0.7348 \pm j3.4662)(s+11.0737 \pm j10.0893)}$$

Plant 11:

$$\frac{p(s)}{\delta_a(s)} = \frac{151.04s(s+0.6236 \pm j3.1825)(s+4.4585)(s+7794.6027)}{(s-0.0125)(s+4.4372)(s+5.7034)(s+100)(s+0.6291 \pm j3.2110)(s+11.0737 \pm j10.0893)}$$

Plant 12:

$$\frac{p(s)}{\delta_a(s)} = \frac{265.76s(s+0.8352 \pm j3.3289)(s+4.4962)(s+1971.1031)}{(s-0.0177)(s+4.4372)(s+6.0711)(s+100)(s+0.7970 \pm j3.2454)(s+11.0737 \pm j10.0893)}$$

Plant 13:

$$\frac{p(s)}{\delta_a(s)} = \frac{202.20s(s+0.6111 \pm j2.8454)(s+4.4675)(s+3910.3260)}{(s-0.0173)(s+4.4372)(s+4.7717)(s+100)(s+0.5996 \pm j2.8429)(s+11.0737 \pm j10.0893)}$$

D.2 Transfer Function $\mathbf{P}_{e_{12}}(s) = \frac{p(s)}{\delta_r(s)}$

Plant 1:

$$\frac{p(s)}{\delta_r(s)} = \frac{160.79s(s + 5.1399 \pm j2.9560)}{(s - 0.0226)(s + 4.4372)(s + 4.7342)(s + 100)(s + 0.6184 \pm j2.5351)}$$

Plant 2:

$$\frac{p(s)}{\delta_r(s)} = \frac{80.39s(s + 4.4056 \pm j3.2242)}{(s - 0.0193)(s + 4.4372)(s + 4.7718)(s + 100)(s + 0.5299 \pm j2.3482)}$$

Plant 3:

$$\frac{p(s)}{\delta_r(s)} = \frac{122.33s(s + 3.9106 \pm j3.3115)}{(s - 0.0219)(s + 4.4372)(s + 3.7251)(s + 100)(s + 0.4638 \pm j2.2221)}$$

Plant 4:

$$\frac{p(s)}{\delta_r(s)} = \frac{122.33s(s + 3.9106 \pm j3.3115)}{(s - 0.0225)(s + 4.4372)(s + 3.6224)(s + 100)(s + 0.4629 \pm j2.2231)}$$

Plant 5:

$$\frac{p(s)}{\delta_r(s)} = \frac{61.17s(s + 3.3519 \pm j3.3289}{(s - 0.0193)(s + 4.4372)(s + 3.6473)(s + 100)(s + 0.3970 \pm j2.0586)}$$

Plant 6:

$$\frac{p(s)}{\delta_r(s)} = \frac{61.17s(s + 3.3519 \pm j3.3289)}{(s - 0.0198)(s + 4.4372)(s + 3.5443)(s + 100)(s + 0.3962 \pm j2.0595)}$$

Plant 7:

$$\frac{p(s)}{\delta_r(s)} = \frac{397.04s(s + 8.0769 \pm j4.6451)}{(s - 0.0142)(s + 4.4372)(s + 7.6264)(s + 100)(s + 0.9762 \pm j3.9567)}$$

Plant 8:

$$\frac{p(s)}{\delta_r(s)} = \frac{397.05s(s+8.0769 \pm j4.6451)}{(s-0.0146)(s+4.4372)(s+7.4112)(s+100)(s+0.9755 \pm j3.9582)}$$

Plant 9:

$$\frac{p(s)}{\delta_r(s)} = \frac{198.52s(s+6.9231 \pm j5.0666)}{(s-0.0125)(s+4.4372)(s+7.4753)(s+100)(s+0.8353 \pm j3.6669)}$$

Plant 10:

$$\frac{p(s)}{\delta_r(s)} = \frac{302.09s(s+6.1452 \pm j5.2038)}{(s-0.0142)(s+4.4372)(s+5.8217)(s+100)(s+0.7348 \pm j3.4662)}$$

Plant 11:

$$\frac{p(s)}{\delta_r(s)} = \frac{151.05s(s+5.2673 \pm j5.2311)}{(s-0.0125)(s+4.4372)(s+5.7034)(s+100)(s+0.6291 \pm j3.2110)}$$

Plant 12:

$$\frac{p(s)}{\delta_r(s)} = \frac{265.76s(s+6.6080 \pm j3.8003)}{(s-0.0177)(s+4.4372)(s+6.0711)(s+100)(s+0.7970 \pm j3.2454)}$$

Plant 13:

$$\frac{p(s)}{\delta_r(s)} = \frac{202.20s(s+5.0275 \pm j4.2574)}{(s-0.0173)(s+4.4372)(s+4.7717)(s+100)(s+0.5996 \pm j2.8429)}$$

D.3 Transfer Function $\mathbf{P}_{e_{21}}(s) = \frac{\beta(s)}{\delta_r(s)}$

Plant 1:

$$\frac{\beta(s)}{\delta_r(s)} = \frac{49.83(s-0.4498)(s-33.9420)(s+0.7.9419 \pm j7.9450)(s+5.0220)}{(s-0.0226)(s+4.4372)(s+4.7342)(s+100)(s+0.6184 \pm j2.5351)(s+11.0737 \pm j10.0893)}$$

Plant 2:

$$\frac{\beta(s)}{\delta_r(s)} = \frac{24.92(s+0.7190)(s+12.6620)(s+15.5574 \pm j22.4002)(s+4.0981)}{(s-0.0193)(s+4.4372)(s+4.7718)(s+100)(s+0.5299 \pm j2.3482)(s+11.0737 \pm j10.0893)}$$

Plant 3:

$$\frac{\beta(s)}{\delta_r(s)} = \frac{37.91(s-4.3592)(s-25.1150)(s+4.3592)(s+6.4502 \pm j5.1924)}{(s-0.0219)(s+4.4372)(s+3.7251)(s+100)(s+0.4638 \pm j2.2221)(s+11.0737 \pm j10.0893)}$$

Plant 4:

$$\frac{\beta(s)}{\delta_r(s)} = \frac{37.91(s-0.4711)(s-34.5206)(s+3.0440)(s+8.5081 \pm j8.7367)}{(s-0.0225)(s+4.4372)(s+3.6224)(s+100)(s+0.4629 \pm j2.2231)(s+11.0737 \pm j10.0893)}$$

Plant 5:

$$\frac{\beta(s)}{\delta_r(s)} = \frac{18.96(s+0.5629)(s+6.0674)(s+8.9243)(s-15.3000 \pm j21.4138)}{(s-0.0193)(s+4.4372)(s+3.6473)(s+100)(s+0.3970 \pm j2.0586)(s+11.0737 \pm j10.0893)}$$

Plant 6:

$$\frac{\beta(s)}{\delta_r(s)} = \frac{18.96(s-3.6589)(s-25.7908)(s+1.5782)(s+6.3605 \pm j5.9201)}{(s-0.0198)(s+4.4372)(s+3.5443)(s+100)(s+0.3962 \pm j2.0595)(s+11.0737 \pm j10.0893)}$$

Plant 7:

$$\frac{\beta(s)}{\delta_r(s)} = \frac{78.31(s-1.5107)(s-48.1421)(s+15.3632)(s+0.3294 \pm j4.9133)}{(s-0.0142)(s+4.4372)(s+7.6264)(s+100)(s+0.9762 \pm j3.9567)(s+11.0737 \pm j10.0893)}$$

Plant 8:

$$\frac{\beta(s)}{\delta_r(s)} = \frac{78.31(s-0.2450)(s-56.7801)(s+11.8098)(s+5.6836 \pm j7.7627)}{(s-0.0146)(s+4.4372)(s+7.4112)(s+100)(s+0.9755 \pm j3.9582)(s+11.0737 \pm j10.0893)}$$

Plant 9:

$$\frac{\beta(s)}{\delta_r(s)} = \frac{39.15(s=0.9761)(s+2.2689)(s+17.0154)(s-27.1719 \pm j20.4655)}{(s-0.0125)(s+4.4372)(s+7.4753)(s+100)(s+0.8353 \pm j3.6669)(s+11.0737 \pm j10.0893)}$$

Plant 10:

$$\frac{\beta(s)}{\delta_r(s)} = \frac{59.58(s-1.5089)(s-49.4974)(s+11.2967)(s+1.8778 \pm j4.5724)}{(s-0.0142)(s+4.4372)(s+5.8217)(s+100)(s+0.7348 \pm j3.4662)(s+11.0737 \pm j10.0893)}$$

Plant 11:

$$\frac{\beta(s)}{\delta_r(s)} = \frac{29.79(s+0.7439)(s+3.1626)(s+13.4091)(s-26.8070 \pm j18.2492)}{(s-0.0125)(s+4.4372)(s+5.7034)(s+100)(s+0.6291 \pm j3.2110)(s+11.0737 \pm j10.0893)}$$

Plant 12:

$$\frac{\beta(s)}{\delta_r(s)} = \frac{64.07(s-0.3155)(s-45.3608)(s+8.4734)(s+6.7694 \pm j7.5346)}{(s-0.0177)(s+4.4372)(s+6.0711)(s+100)(s+0.7970 \pm j3.2454)(s+11.0737 \pm j10.0893)}$$

Plant 13:

$$\frac{\beta(s)}{\delta_r(s)} = \frac{48.74(s-2.4083)(s-37.6040)(s+7.5162)(s+3.5545 \pm j3.4846)}{(s-0.0173)(s+4.4372)(s+4.7717)(s+100)(s+0.5996 \pm j2.8429)(s+11.0737 \pm j10.0893)}$$

D.4 Transfer Function $\mathbf{P}_{e_{22}}(s) = \frac{\beta(s)}{\delta_r(s)}$

Plant 1:

$$\frac{\beta(s)}{\delta_r(s)} = \frac{49.83(s-0.0494)(s-40.3037)(s+4.7197)}{(s-0.0226)(s+4.4372)(s+4.7342)(s+100)(s+0.6184 \pm j2.5351)}$$

Plant 2:

$$\frac{\beta(s)}{\delta_r(s)} = \frac{24.92(s-0.0419)(s-40.4971)(s+4.7557)}{(s-0.0193)(s+4.4372)(s+4.7718)(s+100)(s+0.5299 \pm j2.3482)}$$

Plant 3:

$$\frac{\beta(s)}{\delta_r(s)} = \frac{37.91(s-0.0476)(s-40.6275)(s+3.7015)}{(s-0.0219)(s+4.4372)(s+3.7251)(s+100)(s+0.4638 \pm j2.2221)}$$

Plant 4:

$$\frac{\beta(s)}{\delta_r(s)} = \frac{37.9143(s-0.0490)(s-40.6275)(s+3.5978)}{(s-0.0225)(s+4.4372)(s+3.6224)(s+100)(s+0.4629 \pm j2.2231)}$$

Plant 5:

$$\frac{\beta(s)}{\delta_r(s)} = \frac{18.96(s-0.0415)(s-40.7744)(s+3.6233)}{(s-0.0193)(s+4.4372)(s+3.6473)(s+100)(s+0.3970 \pm j2.0586)}$$

Plant 6:

$$\frac{\beta(s)}{\delta_r(s)} = \frac{18.96(s-0.0427)(s-40.7745)(s+3.5194)}{(s-0.0198)(s+4.4372)(s+3.5443)(s+100)(s+0.3962 \pm j2.0595)}$$

Plant 7:

$$\frac{\beta(s)}{\delta_r(s)} = \frac{78.31(s-0.0307)(s-63.3574)(s+7.6099)}{(s-0.0142)(s+4.4372)(s+7.6264)(s+100)(s+0.9762 \pm j3.9567)}$$

Plant 8:

$$\frac{\beta(s)}{\delta_r(s)} = \frac{78.31(s-0.0316)(s-63.3575)(s+7.3937)}{(s-0.0146)(s+4.4372)(s+7.4112)(s+100)(s+0.9755 \pm j3.9582)}$$

Plant 9:

$$\frac{\beta(s)}{\delta_r(s)} = \frac{39.15(s-63.6605)(s-0.0267)(s+7.4565)}{(s-0.0125)(s+4.4372)(s+7.4753)(s+100)(s+0.8353 \pm j3.6669)}$$

Plant 10:

$$\frac{\beta(s)}{\delta_r(s)} = \frac{59.58(s-0.0304)(s-63.8655)(s+5.7945)}{(s-0.0142)(s+4.4372)(s+5.8217)(s+100)(s+0.7348 \pm j3.4662)}$$

Plant 11:

$$\frac{\beta(s)}{\delta_r(s)} = \frac{29.79(s-0.0265)(s-64.0958)(s+5.6767)}{(s-0.0125)(s+4.4372)(s+5.7034)(s+100)(s+0.6291 \pm j3.2110)}$$

Plant 12:

$$\frac{\beta(s)}{\delta_r(s)} = \frac{64.07(s-0.0385)(s-51.8282)(s+6.0553)}{(s-0.0177)(s+4.4372)(s+6.0711)(s+100)(s+0.7970 \pm j3.2454)}$$

Plant 13:

$$\frac{\beta(s)}{\delta_r(s)} = \frac{48.74(s-0.0371)(s+52.2440)(s+4.7468)}{(s-0.0173)(s+4.4372)(s+4.7717)(s+100)(s+0.5996 \pm j2.8429)}$$

D.5 Transfer Function $\mathbf{P}_{d_{11}}(s) = \frac{p(s)}{d(s)}$

Plant 1:

$$\frac{p(s)}{d(s)} = \frac{2.40s(s + 0.6182 \pm j2.4803)}{(s - 0.0226)(s + 4.7342)(s + 0.6184 \pm j2.5351)}$$

Plant 2:

$$\frac{p(s)}{d(s)} = \frac{2.40s(s + 0.5299 \pm j2.3023)}{(s - 0.0193)(s + 4.7718)(s + 0.5299 \pm j2.3482)}$$

Plant 3:

$$\frac{p(s)}{d(s)} = \frac{1.83s(s + 0.4703 \pm j2.1729)}{(s - 0.0219)(s + 3.7251)(s + 0.4638 \pm j2.2221)}$$

Plant 4:

$$\frac{p(s)}{d(s)} = \frac{1.83s(s + 0.4703 \pm j2.1729}{(s - 0.0225)(s + 3.6224)(s + 0.4629 \pm j2.2231)}$$

Plant 5:

$$\frac{p(s)}{d(s)} = \frac{1.83s(s + 0.4031 \pm j2.0156)}{(s - 0.0193)(s + 3.6473)(s + 0.3970 \pm j2.0586)}$$

Plant 6:

$$\frac{p(s)}{d(s)} = \frac{1.83s(s + 0.4031 \pm j2.0156)}{(s - 0.0198)(s + 3.5443)(s + 0.3962 \pm j2.0595)}$$

Plant 7:

$$\frac{p(s)}{d(s)} = \frac{5.93s(s + 0.9714 \pm j3.8977)}{(s - 0.0142)(s + 7.6264)(s + 0.9762 \pm j3.9567)}$$

Plant 8:

$$\frac{p(s)}{d(s)} = \frac{5.93s(s + 0.9714 \pm j3.8977)}{(s - 0.0146)(s + 7.4112)(s + 0.9755 \pm j3.9582)}$$

Plant 9:

$$\frac{p(s)}{d(s)} = \frac{5.93s(s + 0.8326 \pm j2.6179)}{(s - 0.0125)(s + 7.4753)(s + 0.8353 \pm j3.6669)}$$

Plant 10:

$$\frac{p(s)}{d(s)} = \frac{4.51s(s + 0.7391 \pm j3.4145)}{(s - 0.0142)(s + 5.8217)(s + 0.7348 \pm j3.4662)}$$

Plant 11:

$$\frac{p(s)}{d(s)} = \frac{4.51s(s + 0.6335 \pm j3.1674)}{(s - 0.0125)(s + 5.7034)(s + 0.6291 \pm j3.2110)}$$

Plant 12:

$$\frac{p(s)}{d(s)} = \frac{3.97s(s + 0.7947 \pm j3.1888)}{(s - 0.0177)(s + 6.0711)(s + 0.7970 \pm j3.2454)}$$

Plant 13:

$$\frac{p(s)}{d(s)} = \frac{3.02s(s + 0.6047 \pm j2.7935)}{(s - 0.0173)(s + 4.7717)(s + 0.5996 \pm j2.8429)}$$

D.6 Transfer Function $\mathbf{P}_{d_{21}}(s) = \frac{\beta(s)}{d(s)}$

Plant 1:

$$\frac{\beta(s)}{d(s)} = \frac{0.0346(s+0.5361)(s-36.6976)}{(s-0.0226)(s+4.7342)(s+0.6184 \pm j2.5351)}$$

Plant 2:

$$\frac{\beta(s)}{d(s)} = \frac{0.0346(s-1.9495)(s-34.1827)}{(s-0.0193)(s+4.7718)(s+0.5299 \pm j2.3482)}$$

Plant 3:

$$\frac{\beta(s)}{d(s)} = \frac{0.0264(s+0.4604)(s-32.4824)}{(s-0.0219)(s+3.7251)(s+0.4638 \pm j2.2221)}$$

Plant 4:

$$\frac{\beta(s)}{d(s)} = \frac{0.0264(s+0.4604)(s-32.4824)}{(s-0.0225)(s+3.6224)(s+0.4629 \pm j2.2231)}$$

Plant 5:

$$\frac{\beta(s)}{d(s)} = \frac{0.0264(s+0.4193)(s-30.5580)}{(s-0.0193)(s+3.6473)(s+0.3970 \pm j2.0586)}$$

Plant 6:

$$\frac{\beta(s)}{d(s)} = \frac{0.0264(s+0.4193)(s-30.5578)}{(s-0.0198)(s+3.5443)(s+0.3962 \pm j2.0595)}$$

Plant 7:

$$\frac{\beta(s)}{d(s)} = \frac{0.0855(s+0.4961)(s-39.6594)}{(s-0.0142)(s+7.6264)(s+0.9762 \pm j3.9567)}$$

Plant 8:

$$\frac{\beta(s)}{d(s)} = \frac{0.0855(s+0.4961)(s-39.6595)}{(s-0.0146)(s+7.4112)(s+0.9755 \pm j3.9582)}$$

Plant 9:

$$\frac{\beta(s)}{d(s)} = \frac{0.0855(s+0.4713)(s-35.7606)}{(s-0.0125)(s+7.4753)(s+0.8353 \pm j3.6669)}$$

Plant 10:

$$\frac{\beta(s)}{d(s)} = \frac{0.0855(s+0.4514)(s-33.1269)}{(s-0.0142)(s+5.8217)(s+0.7348 \pm j3.4662)}$$

Plant 11:

$$\frac{\beta(s)}{d(s)} = \frac{0.0651(s+0.4250)(s-30.1487)}{(s-0.0125)(s+5.7034)(s+0.6291 \pm j3.2110)}$$

Plant 12:

$$\frac{\beta(s)}{d(s)} = \frac{0.0572(s+0.5257)(s-37.4245)}{(s-0.0177)(s+6.0711)(s+0.7970 \pm j3.2454)}$$

Plant 13:

$$\frac{\beta(s)}{d(s)} = \frac{0.0436(s+0.4666)(s-32.0527)}{(s-0.0173)(s+4.7717)(s+0.5996 \pm j2.8429)}$$

Appendix E. MISO Equivalent Transfer Functions

This appendix lists the MISO equivalent transfer functions used for roll and yaw channel loop-shaping.

E.1 Roll Channel $q_{22}(s)$

Plant 1:

$$q_{22}(s) = \frac{312234.51s(s-40.5188)}{(s-0.0494)(s-40.3037)(s+4.7197)(s+100)(s+11.07365 \pm j10.0893)}$$

Plant 2:

$$q_{22}(s) = \frac{624469.02s(s-40.7030)}{(s-0.0494)(s-40.4971)(s+4.7557)(s+100)(s+11.07365 \pm j10.0893)}$$

Plant 3:

$$q_{22}(s) = \frac{475115.98s(s-40.8274)}{(s-0.0476)(s-40.6275)(s+3.7015)(s+100)(s+11.07365 \pm j10.0893)}$$

Plant 4:

$$q_{22}(s) = \frac{237557.98s(s-40.8274)}{(s-0.0494)(s-40.6275)(s+3.5978)(s+100)(s+11.07365 \pm j10.0893)}$$

Plant 5:

$$q_{22}(s) = \frac{475115.98s(s-40.9676)}{(s-0.0415)(s-40.7744)(s+3.6233)(s+100)(s+11.07365 \pm j10.0893)}$$

Plant 6:

$$q_{22}(s) = \frac{237557.98s(s-40.9676)}{(s-0.0427)(s-40.7745)(s+3.5194)(s+100)(s+11.07365 \pm j10.0893)}$$

Plant 7:

$$q_{22}(s) = \frac{1542055.60s(s - 63.6723)}{(s - 0.0307)(s - 63.3574)(s + 7.6099)(s + 100)(s + 11.07365 \pm j10.0893)}$$

Plant 8:

$$q_{22}(s) = \frac{771027.79s(s - 63.6723)}{(s - 0.0316)(s - 63.3575)(s + 7.3937)(s + 100)(s + 11.07365 \pm j10.0893)}$$

Plant 9:

$$q_{22}(s) = \frac{1542055.60s(s - 63.9620)}{(s - 0.0267)(s - 63.6605)(s + 7.4565)(s + 100)(s + 11.07365 \pm j10.0893)}$$

Plant 10:

$$q_{22}(s) = \frac{1173245.30s(s - 64.1573)}{(s - 0.0304)(s - 63.8655)(s + 5.7945)(s + 100)(s + 11.07365 \pm j10.0893)}$$

Plant 11:

$$q_{22}(s) = \frac{1173245.30s(s - 64.3777)}{(s - 0.0265)(s - 64.0958)(s + 5.6767)(s + 100)(s + 11.07365 \pm j10.0893)}$$

Plant 12:

$$q_{22}(s) = \frac{517074.41s(s - 52.0921)}{(s - 0.0385)(s - 51.8282)(s + 6.0553)(s + 100)(s + 11.07365 \pm j10.0893)}$$

Plant 13:

$$q_{22}(s) = \frac{785291.76s(s - 52.4889)}{(s - 0.0371)(s - 52.2440)(s + 4.7468)(s + 100)(s + 11.07365 \pm j10.0893)}$$

E.2 Yaw Channel $q_{33_e}(s)$

Plant 1:

$$q_{33_e}(s) = \frac{63417.73(s-40.3100)(s-40.5188)}{(s-40.2054)(s+4.4706)(s+1293.9194)(s+100)(s+0.6847 \pm j2.5895)}$$

Plant 2:

$$q_{33_e}(s) = \frac{132266.67(s-40.5086)(s-40.7031)}{(s-40.4193)(s+4.4466)(s+5342.83)(s+100)(s+0.5219 \pm j2.3163)}$$

Plant 3:

$$q_{33_e}(s) = \frac{97956.56(s-40.6363)(s-40.8274)}{(s-40.5431)(s+4.4553)(s+2613.6590)(s+100)(s+0.4794 \pm j2.2127)}$$

Plant 4:

$$q_{33_e}(s) = \frac{48912.58(s-40.6321)(s-40.8274)}{(s-40.5393)(s+4.4629)(s+1318.9502)(s+100)(s+0.5237 \pm j2.2633)}$$

Plant 5:

$$q_{33_e}(s) = \frac{97943.79(s-40.7829)(s-40.9676)}{(s-40.6915)(s+4.4470)(s+5201.9369)(s+100)(s+0.3964 \pm j2.0268)}$$

Plant 6:

$$q_{33_e}(s) = \frac{48799(s-40.7788)(s-40.9676)}{(s-40.6867)(s+4.4501)(s+2612.6786)(s+100)(s+0.4117 \pm j2.0498)}$$

Plant 7:

$$q_{33_e}(s) = \frac{203390.43(s-63.3736)(s-63.6723)}{(s-63.2294)(s+4.4885)(s+2620.9281)(s+100)(s+0.9724 \pm j3.9645)}$$

Plant 8:

$$q_{33_e}(s) = \frac{102593.59(s-63.3658)(s-63.6723)}{(s-63.2232)(s+4.5416)(s+1326.1636)(s+100)(s+1.0261 \pm j4.0568)}$$

Plant 9:

$$q_{33_e}(s) = \frac{202804.46(s-63.6758)(s-63.9620)}{(s-63.5351)(s+4.4620)(s+5208.1863)(s+100)(s+0.8152 \pm j3.6363)}$$

Plant 10:

$$q_{33_e}(s) = \frac{154544.77(s-63.8771)(s-64.1573)}{(s-63.7418)(s+4.4832)(s+2617.5386)(s+100)(s+0.7413 \pm j3.4726)}$$

Plant 11:

$$q_{33_e}(s) = \frac{154212.1633(s-64.1069)(s-64.3777)}{(s-63.9738)(s+4.4597)(s+5205.2705)(s+100)(s+0.6204 \pm j3.1827)}$$

Plant 12:

$$q_{33_e}(s) = \frac{83727.5912(s-51.8356)(s-52.0921)}{(s-51.7151)(s+4.5037)(s+1323.6283)(s+100)(s+0.8576 \pm j3.3283)}$$

Plant 13:

$$q_{33_e}(s) = \frac{126250.73(s-52.2544)(s-52.4889)}{(s-52.1406)(s+4.4682)(s+2615.5985)(s+100)(s+0.6115 \pm j2.8439)}$$

Appendix F. Difference Equations

This appendix presents the difference equations needed for digital implementation of the designed flight controllers and prefilters. The equations assume a sampling rate of $50Hz$.

Equations (4.15) and (4.13) are the z-plane representations of the designed longitudinal prefilter and controller, respectively. Equations (5.19) and (5.20) are z-plane representations of the lateral prefilters. Equations (5.15) and (5.16) are z-plane representations of the lateral controllers. The prefilters and controllers are converted to difference equations for implementation on Lambda's digital flight controller.

The z-plane transfer functions are of the form:

$$G(z) = \frac{Y(z)}{U(z)} = \frac{c_m z^m + c_{m-1} z^{m-1} + ... + c_1 z + c_o}{d_n z^n + d_{n-1} z^{n-1} + ... + d_1 z + d_o} \tag{F.1}$$

where: $n \geq m$ and $d_n = 1$. The difference equation is formed by dividing the equation by z^n, cross multiplying, and replacing the negative powers of z with the appropriate delay to obtain:

$$\begin{aligned} y(kT) \;=\; & -d_{n-1}y[(k-1)T] - ... - d_1 y[(k+1-n)T] - d_0 y[(k-n)T] \\ & + c_m u[(k+m-n)T] + c_{m-1} u[(k+m-n-1)T] + ... \\ & + c_1 u[(k+1-n)T] + c_0 u[(k-n)T] \end{aligned} \tag{F.2}$$

The difference equations are listed below:

$$\begin{aligned} f_{11}(kT) \;=\; & 2.57754514 f_{11}[(k-1)T] \\ & -2.20234613 f_{11}[(k-2)T] \\ & -0.62346973 f_{11}[(k-3)T] \\ & +0.03569841 q_{ref}[kT] \\ & -0.03436716 q_{ref}[(k-1)T] \end{aligned} \tag{F.3}$$

$$\begin{aligned} g_{11}(kT) \;=\; & 1.46358316 g_{11}[(k-1)T] \\ & -0.02849538 g_{11}[(k-2)T] \end{aligned}$$

$$
\begin{aligned}
&-0.34868264 g_{11}[(k-3)T] \\
&-0.08121895 g_{11}[(k-4)T] \\
&-0.00518618 g_{11}[(k-5)T] \\
&+12.25155696 \delta_{e_{cmd}}[kT] \\
&-29.69703900 \delta_{e_{cmd}}[(k-1)T] \\
&+11.84532698 \delta_{e_{cmd}}[(k-2)T] \\
&+23.14265795 \delta_{e_{cmd}}[(k-3)T] \\
&-24.09492395 \delta_{e_{cmd}}[(k-4)T] \\
&+6.55634105 \delta_{e_{cmd}}[(k-5)T]
\end{aligned} \tag{F.4}
$$

$$
\begin{aligned}
f_{22}(kT) = \quad & 1.70497427 f_{22}[(k-1)T] \\
& -0.72555746 f_{22}[(k-2)T] \\
& 0.02058319 p_{ref}[kT]
\end{aligned} \tag{F.5}
$$

$$
\begin{aligned}
g_{22}(kT) = \quad & 1.55845411 g_{22}[(k-1)T] \\
& -0.17971014 g_{22}[(k-2)T] \\
& -0.31884058 g_{22}[(k-3)T] \\
& +0.05700483 g_{22}[(k-4)T] \\
& +0.00289855 g_{22}[(k-5)T] \\
& +5.99046148 \delta_{a_{cmd}}[kT] \\
& -15.19126028 \delta_{a_{cmd}}[(k-1)T] \\
& +7.20757487 \delta_{a_{cmd}}[(k-2)T] \\
& 11.23289141 \delta_{a_{cmd}}[(k-3)T] \\
& -13.19796181 \delta_{a_{cmd}}[(k-4)T] \\
& +3.95844341 \delta_{a_{cmd}}[(k-5)T]
\end{aligned} \tag{F.6}
$$

$$
\begin{aligned}
f_{33}(kT) = \quad & 2.90477497 f_{33}[(k-1)T] \\
& -2.81330221 f_{33}[(k-2)T] \\
& -0.90846623 f_{33}[(k-3)T] \\
& +0.00308112 \beta_{ref}[kT] \\
& -0.00302011 \beta_{ref}[(k-1)T]
\end{aligned} \tag{F.7}
$$

$$
\begin{aligned}
g_{33}(kT) \;=\;& 3.44977611 g_{33}[(k-1)T] \\
& -4.55182299 g_{33}[(k-2)T] \\
& +2.84736852 g_{33}[(k-3)T] \\
& -0.83858820 g_{33}[(k-4)T] \\
& +0.09326655 g_{33}[(k-5)T] \\
& -22.12114283 \delta_{r_{cmd}}[kT] \\
& +63.99586422 \delta_{r_{cmd}}[(k-1)T] \\
& -39.63341388 \delta_{r_{cmd}}[(k-2)T] \\
& -44.11914690 \delta_{r_{cmd}}[(k-3)T] \\
& +61.75453156 \delta_{r_{cmd}}[(k-4)T] \\
& -19.87674225 \delta_{r_{cmd}}[(k-5)T]
\end{aligned} \tag{F.8}
$$

Bibliography

1. Pachter, Meir, "Personal Conversation and Unpublished Notes", Visiting Professor of Electrical Engineering, Air Force Institute of Technology, Wright-Patterson AFB, OH, April-Sept 1993.
2. Wheaton, Captain Donald G., *Automatic Flight Control System Design for an Unmanned Research Vehicle Using Discrete QFT*, MS thesis, Air Force Institute of Technology, Wright Patterson AFB, OH, December 1990.
3. Swift, First Lieutenant Gerald A., *Model Identification and Control System Design for the Lambda Unmanned Research Vehicle*, MS thesis, Air Force Institute of Technology, Wright Patterson AFB, OH, September 1991.
4. Lacey, Captain Donald J., *A Robust Digital Flight Control System for an Unmanned Research Vehicle Using Discrete Quantitative Feedback Theory*, MS thesis, Air Force Institute of Technology, Wright Patterson AFB, OH, December 1991.
5. Horowitz, Isaac M., "Quantitative Synthesis of Uncertain Multiple-Input, Multiple-Output Feedback Systems", *International Journal of Control*, 1979, vol.30, No.1, 81-106.
6. Blakelock, John H., *Automatic Control of Aircraft and Missiles* (2nd ed.), John Wiley & Sons, 1991.
7. Horowitz, Isaac M., "Improved Design Technique for Uncertain Multiple-Input, Multiple-Output Feedback Systems", *International Journal of Control*, 1982, vol.36, No.6, 977-988.
8. D'Azzo, J.J. and Houpis, C.H., *Linear Control System Analysis and Design, Conventional and Modern* (3rd ed.), McGraw-Hill, 1988.
9. Houpis, C.H. and Lamont, G.B., *Digital Control Systems, Theory, Hardware, Software* (2nd ed.), McGraw-Hill, 1992.
10. Lane, D.W., *Multiple Model Adaptive Estimation Applied to Actuator and Sensor Failure Detection on the Lambda Unmanned Reearch Vehicle*, MS thesis, Air Force Institute of Technology, Wright Patterson AFB, OH, December 1993.
11. Houpis, C.H., *Quantitative Feedback Theory, Technique for Designing Multivariable Control Systems*, AFWAL-TR-86-3107, Wright Aeronautical Laboratories, Wright-Patterson AFB, OH, January 1987.

Vita

Captain Mark S. Keating was born May 17, 1967 in Petersburg, Virginia. He graduated from Northern Highlands Regional High School in Allendale, New Jersey in 1985. He attended The Citadel, The Military College of South Carolina, graduating Magna Cum Laude with a BS in Electrical Engineering in May 1989. He received his commission through the Reserve Officer Training Corps and reported for active duty in August 1989. His first assignment was as a Satellite Engineering Officer with the 2nd Satellite Control Squadron at Falcon AFB, Colorado. He came to the Air Force Institute of Technology in May 1992. He and his wife, Margaret, were married in December 1991.

Permanent address: 527 Fort Johnson Road
Charleston, South Carolina 29412

REPORT DOCUMENTATION PAGE

Form Approved
OMB No. 0704-0188

Public reporting burden for this collection of information is estimated to average 1 hour per response, including the time for reviewing instructions, searching existing data sources, gathering and maintaining the data needed, and completing and reviewing the collection of information. Send comments regarding this burden estimate or any other aspect of this collection of information, including suggestions for reducing this burden, to Washington Headquarters Services, Directorate for information Operations and Reports, 1215 Jefferson Davis Highway, Suite 1204, Arlington, VA 22202-4302, and to the Office of Management and Budget, Paperwork Reduction Project (0704-0188), Washington, DC 20503.

1. AGENCY USE ONLY (Leave blank)	2. REPORT DATE	3. REPORT TYPE AND DATES COVERED
	December 1993	Master's Thesis

4. TITLE AND SUBTITLE

DESIGN OF A FLIGHT CONTROLLER FOR AN UNMANNED RESEARCH VEHICLE WITH CONTROL SURFACE FAILURES USING QUANTITATIVE FEEDBACK THEORY

5. FUNDING NUMBERS

6. AUTHOR(S)

Mark S. Keating, Captain, USAF

7. PERFORMING ORGANIZATION NAME(S) AND ADDRESS(ES)

Air Force Institute of Technology, WPAFB OH 45433-6583

8. PERFORMING ORGANIZATION REPORT NUMBER

AFIT/GE/ENG/93D-18

9. SPONSORING/MONITORING AGENCY NAME(S) AND ADDRESS(ES)

Capt. Stuart Sheldon
Air Force Wright Laboratories, Flight Dynamics Directorate
WL/FIGS
Wright-Paterson AFB, OH 45433

10. SPONSORING/MONITORING AGENCY REPORT NUMBER

11. SUPPLEMENTARY NOTES

12a. DISTRIBUTION/AVAILABILITY STATEMENT

Approved for public release; distribution unlimited

12b. DISTRIBUTION CODE

13. ABSTRACT *(Maximum 200 words)*

This thesis describes the application of the multiple-input multiple-ouput (MIMO) Quantitative Feedback Theory (QFT) design technique to the design of a digital flight control system for the Lambda Unmanned Research Vehicle (URV). The QFT technique allows the synthesis of a control system which is robust in the presence of structured plant uncertainties. Uncertainties considered in this design are the aircraft's plant variation within the flight envelope and the effects of damage to aircraft control surfaces. Mathematical models of control surface failure effects on aircraft dynamics are derived and used to modify an existing small perturbation model of the Lambda. The QFT technique is applied to design a control system utilizing aircraft pitch rate, roll rate and sideslip angle as feedback variables. The inherent cross-coupling rejection qualities of QFT and an aileron-rudder interconnect are utilized to design a control system which results in a coordinated flight. An outer-loop autopilot is then designed around the QFT controller to further assist turn coordination. Sensor noise effects on aircraft states are also analyzed.

14. SUBJECT TERMS	15. NUMBER OF PAGES
Quantitative Feedback Theory, Flight Control System, Aircraft Damage	161
	16. PRICE CODE

17. SECURITY CLASSIFICATION OF REPORT	18. SECURITY CLASSIFICATION OF THIS PAGE	19. SECURITY CLASSIFICATION OF ABSTRACT	20. LIMITATION OF ABSTRACT
Unclassified	Unclassified	Unclassified	UL